**Title:**

Pressure Sensitivity Kernels Applied to Time-reversal Acoustics

**Author:**

Raghukumar, Kaustubha

**Publication Date:**

06-19-2009

**Series:**

Scripps Institution of Oceanography Technical Report

**Publication Info:**

UC San Diego, Scripps Institution of Oceanography Technical Report, Scripps Institution of Oceanography

**Permalink:**

http://www.escholarship.org/uc/item/86g5s4w8

**Citation:**

Raghukumar, Kaustubha. (2009). Pressure Sensitivity Kernels Applied to Time-reversal Acoustics. UC San Diego: Scripps Institution of Oceanography. Retrieved from: http://www.escholarship.org/uc/item/86g5s4w8

**Additional Info:**

Originally published as: Raghukumar, Kaustubha. Pressure sensitivity kernels applied to time-reversal acoustics, Ph.D. Dissertation, University of California, San Diego, 2009

**Abstract:**

<p>Time-reversal is a method of focusing sound in the ocean that has found a variety of applications in recent years, ranging from underwater communications to biological stone destruction. In order to produce a focal spot, the time-reversal process first needs to acquire the Green's function between source and receiver. This Green's function is time-reversed and retransmitted in order to produce a spatio-temporal focal spot at the original source location. If the medium properties in between the source and receiver change between the acquisition of the Green's function and the subsequent retransmission, the quality of the focal spot can degrade or even disappear. However, the time-reversal focal spot has been found to be surprisingly robust to changes in medium properties, which are chiefly sound speed fluctuations in underwater acoustics. At 445 Hz, the focal spot was seen to persist for a week, while at 3.5 kHz, the focal spot persists for about an hour.</p> <p>Sensitivity kernels have the ability to linearly map sound speed perturbations to a perturbation of an acoustic parameter such as travel-time or pressure. Sensitivity kernels have a Fresnel-like interference pattern with regions of positive and negative sensitivities in the medium. Time-reversal, which causes different arrival paths to arrive at the same time, results in overlapping sensitivity kernels that leads to a net reduction in pressure sensitivity at

| 1. REPORT DATE<br>**2009** | 2. REPORT TYPE | 3. DATES COVERED<br>**00-00-2009 to 00-00-2009** |
| :--- | :--- | :--- |

| 4. TITLE AND SUBTITLE<br>**Pressure Sensitivity Kernels Applied to Time-reversal Acoustics** | 5a. CONTRACT NUMBER |
| :--- | :--- |
| | 5b. GRANT NUMBER |
| | 5c. PROGRAM ELEMENT NUMBER |
| 6. AUTHOR(S) | 5d. PROJECT NUMBER |
| | 5e. TASK NUMBER |
| | 5f. WORK UNIT NUMBER |
| 7. PERFORMING ORGANIZATION NAME(S) AND ADDRESS(ES)<br>**University of California, San Diego,9500 Gilman Dr,La Jolla,CA,92093** | 8. PERFORMING ORGANIZATION REPORT NUMBER |
| 9. SPONSORING/MONITORING AGENCY NAME(S) AND ADDRESS(ES) | 10. SPONSOR/MONITOR'S ACRONYM(S) |
| | 11. SPONSOR/MONITOR'S REPORT NUMBER(S) |

| 12. DISTRIBUTION/AVAILABILITY STATEMENT |
| :--- |
| **Approved for public release; distribution unlimited** |

| 13. SUPPLEMENTARY NOTES |
| :--- |

| 14. ABSTRACT |
| :--- |
| **see report** |

| 15. SUBJECT TERMS |
| :--- |

| 16. SECURITY CLASSIFICATION OF: | | | 17. LIMITATION OF ABSTRACT | 18. NUMBER OF PAGES | 19a. NAME OF RESPONSIBLE PERSON |
| :---: | :---: | :---: | :---: | :---: | :---: |
| a. REPORT<br>**unclassified** | b. ABSTRACT<br>**unclassified** | c. THIS PAGE<br>**unclassified** | **Same as Report (SAR)** | **147** | |

the focal spot. Upon expressing the pressure at the focal spot in terms of sensitivity kernels, source transmissions are derived that are even more robust than time-reversal. </p> <p>The theory developed using pressure sensitivity kernels is tested on experimental data, along with an internal wave model, using various metrics. The linear limitations of the kernels are explored in the context of time-evolving Green's functions. The optimized source functions are then tested using experimental Green's functions and their behavior is seen to be in the right sense.</p> <p>Finally, thermistor chain data gathered during a similar experiment allowed for the testing of a 'synthetic aperture thermistor chain'. Temperature observations, presumably caused by displacements of a reference temperature profile, are inverted to provide an estimate of the background temperature profile.</p>

UNIVERSITY OF CALIFORNIA, SAN DIEGO

**Pressure Sensitivity Kernels Applied to Time-reversal Acoustics**

A dissertation submitted in partial satisfaction of the
requirements for the degree
Doctor of Philosophy

in

Oceanography

by

Kaustubha Raghukumar

Committee in charge:

    William S. Hodgkiss, Chair
    Bruce D. Cornuelle
    Kenneth Kreutz-Delgado
    William A. Kuperman
    Robert Pinkel

2009

The dissertation of Kaustubha Raghukumar is approved, and it is acceptable in quality and form for publication on microfilm and electronically:

_____

_____

_____

_____

_____
Chair

University of California, San Diego

2009

# DEDICATION

To family...

TABLE OF CONTENTS

# LIST OF FIGURES

LIST OF TABLES

# ACKNOWLEDGEMENTS

I am deeply grateful to my advisors Professor William Hodgkiss and Dr. Bruce Cornuelle for taking me on as a graduate student and guiding me through my doctorate. Their advice, constant encouragement and occasional criticism has allowed me to realize my strengths and work on my weaknesses. They are both incredible scientists in their own special way and I have learned a great deal from each. Bruce has greatly inspired me with his vast reservoir of oceanographic knowledge, all of which seems to be readily accessible at a moments notice. He was always available when I needed help and for that I am thankful. Bill never fails to impress me with his ability to drive straight to the heart of matters, no matter how complex they might seem.

I am also thankful to Professor William Kuperman, a great physicist and director of MPL, whose presence at our meetings allowed us to arrive at much more elegant conclusions.

My committee members, Professor Robert Pinkel and Professor Ken Kreutz-Delgado deserve my thanks for providing their valuable time and advice.

My parents deserve my gratitude for allowing me to find my own way, but always being present for help, encouragement and words of advice. My sister deserves special mention for being a good friend, travel companion and for opening my eyes to new worlds and ways of thinking.

Special thanks go out to all my friends at SIO who are now almost like family. I will always fondly remember the good times, discussions, trips and pranks.

Thanks to the staff at MPL, especially Evelyn Doudera and Norissa Gastelum, for all the help that made everything so much easier.

This dissertation is a collection of papers that were published, submitted for publication, or in preparation for submission.

The text of Chapter Two is in full a reprint of the material as it appears in Kaustubha Raghukumar, Bruce Cornuelle, William Hodgkiss, William Kuperman,

"Pressure sensitivity kernels applied to time-reversal acoustics", J. Acoustic Soc. Am., Vol. 124, Issue 1, pp. 98-112, 2008.

The text of Chapter Three is in full a reprint of the material as it appears in Kaustubha Raghukumar, Bruce Cornuelle, William Hodgkiss, William Kuperman, "Experimental demonstration of pressure sensitivity kernels", to be submitted to J. Acoustic Soc. Am., 2009.

The text of Chapter Four is in full a reprint of the material as it appears in Kaustubha Raghukumar, Bruce Cornuelle, William Hodgkiss, William Kuperman, "Temperature profile estimation using thermistor chain data", in preparation, 2009.

The dissertation author was the primary researcher and author, and the co-authors listed in these publications directed and supervised the research which forms the basis for this dissertation.

VITA

| | |
|---|---|
| 2000 | B.E. in Electrical Engineering,<br>Goa University, Goa, India |
| 2003 | M.S. in Telecommunications,<br>New Jersey Institute of Technology, Newark, New Jersey |
| 2009 | Ph.D. in Oceanography,<br>Scripps Institution of Oceanography, University of California,<br>San Diego, CA |
| 2000-2001 | Software Engineer, Infosys Technologies, Bangalore, India |
| 2002-2003 | Research Assistant, Center for Communications and Signal<br>Processing Research, New Jersey Institute of Technology, Newark,<br>New Jersey |
| 2003-2009 | Graduate Student Research Associate<br>Marine Physical Laboratory, Scripps Institution of Oceanography, University of California, San Diego, CA |

PUBLICATIONS

Journals

1. K. Raghukumar, B. D. Cornuelle, W. S. Hodgkiss, and W. A. Kuperman, "Sensitivity analysis applied to time-reversal acoustics," Journal of the Acoustical Society of America, July 2008, Vol. 124, Issue 1, pp. 98-112.

2. K. Raghukumar, B. D. Cornuelle, W. S. Hodgkiss, and W. A. Kuperman, "Optimized source functions based on pressure sensitivity kernels," to be submitted to Journal of the Acoustical Society of America.

3. K. Raghukumar, B. D. Cornuelle, W. S. Hodgkiss, and W. A. Kuperman, "A method of estimating a reference temperature profile given thermistor chain observations," to be submitted to Journal of Atmospheric and Ocean Technology.

4. H. C. Song, W. S. Hodgkiss, W. A. Kuperman, W. J. Higley, K. Raghukumar, T. Akal, and M. Stevenson, "Spatial diversity in passive time reversal communications," Journal of the Acoustical Society of America, October 2006, Vol. 120, Issue 4, pp. 2067-2076.

5. Chakraborty B., Kaustubha, R.,Hegde, A., Pereira, A., "Acoustic seafloor sediment classification using self-organizing feature maps," IEEE Transactions on Geoscience and Remote Sensing, Vol. 39 pp. 2722 - 2725 doi: 10.1109/36.975006, 2001.

Conferences

1. K. Raghukumar, B. D. Cornuelle, W. S. Hodgkiss, and W. A. Kuperman, "Optimized source functions based on pressure sensitivity kernels," ASA-ESA Acoustics '08, Paris, 2008.

2. K. Raghukumar, B. D. Cornuelle, W. S. Hodgkiss, and W. A. Kuperman, "Sensitivity analysis applied to time-reversal acoustics," Acoustical Society of America, New Orleans, 2007.

3. K. Raghukumar, Philippe Roux, W. S. Hodgkiss, and W. A. Kuperman, "Towards multichannel underwater communications using time reversal," Acoustical Society of America, Austin, 2003.

4. Michael B. Porter, Paul Hursky, Martin Siderius, Mohsen Badiey, Jerald Caruthers, William S. Hodgkiss, Kaustubha Raghukumar, Dan Rouseff, Warren Fox, Christian de Moustier, Brian Calder, Barbara J. Kraft, Keyko McDonald, Peter Stein, James K. Lewis, and Subramaniam Ra jan. "Kauaiex: Environ- mental effects on hf acoustic propagation with application to communications," Acoustical Society of America, New York, 2004.

5. S. Wang, K. Raghukumar, A. Abdi, J. Wallace, M. Jensen, "Indoor MIMO channels: a parametric correlation model and experimental results," IEEE/ Sarnoff Symposium on Advances in Wired and Wireless Communication, pp. 1-5, doi: 10.1109/SARNOF.2004.1302827, 2004.

Technical Reports

1. K. Raghukumar, W. S. Hodgkiss, "Pressure sensitivity kernels applied to time-reversal acoustics," ONR Graduate studentship final report, 2008.

ABSTRACT OF THE DISSERTATION

## Pressure Sensitivity Kernels Applied to Time-reversal Acoustics

by

Kaustubha Raghukumar

Doctor of Philosophy in Oceanography

University of California San Diego, 2009

William S. Hodgkiss, Chair

Time-reversal is a method of focusing sound in the ocean that has found a variety of applications in recent years, ranging from underwater communications to biological stone destruction. In order to produce a focal spot, the time-reversal process first needs to acquire the Green's function between source and receiver. This Green's function is time-reversed and retransmitted in order to produce a spatio-temporal focal spot at the original source location. If the medium properties in between the source and receiver change between the acquisition of the Green's function and the subsequent retransmission, the quality of the focal spot can degrade or even disappear. However, the time-reversal focal spot has been found to be surprisingly robust to changes in medium properties, which are chiefly sound speed fluctuations in underwater acoustics. At 445 Hz, the focal spot was seen to persist for a week, while at 3.5 kHz, the focal spot persists for about an hour.

Sensitivity kernels have the ability to linearly map sound speed perturbations to a perturbation of an acoustic parameter such as travel-time or pressure. Sensitivity kernels have a Fresnel-like interference pattern with regions of positive and negative sensitivities in the medium. Time-reversal, which causes different arrival paths to arrive at the same time, results in overlapping sensitivity kernels that leads to a net reduction in pressure sensitivity at the focal spot. Upon expressing the pressure at the focal spot in terms of sensitivity kernels, source transmissions

are derived that are even more robust than time-reversal.

The theory developed using pressure sensitivity kernels is tested on experimental data, along with an internal wave model, using various metrics. The linear limitations of the kernels are explored in the context of time-evolving Green's functions. The optimized source functions are then tested using experimental Green's functions and their behavior is seen to be in the right sense.

Finally, thermistor chain data gathered during a similar experiment allowed for the testing of a 'synthetic aperture thermistor chain'. Temperature observations, presumably caused by displacements of a reference temperature profile, are inverted to provide an estimate of the background temperature profile.

# Chapter 1

# Introduction

## 1.1 Background

The scientific focus on shallow water acoustics since the end of the cold war has lead to a renewed interest in environmentally-induced acoustic fluctuations, together with ways and means to understand and mitigate their effect. A wide variety of applications ranging from underwater communications and mine detection to the acoustic tagging of marine mammals require an understanding of the oceanographic fluctuations that can influence an acoustic signal as it makes its way from a source to the receiver. Shallow water acoustic propagation, in particular, has to deal with a higher degree of environmental complexity compared to acoustic propagation in deeper water. This is due to a variety of reasons such as increased bottom and surface interaction, a higher frequency of operation, and a higher noise floor due to the proximity to shipping lanes. [1] Another major cause of fluctuations are internal waves whose presence results in the heaving of the thermocline in the water column, resulting in sound speed perturbations that in turn perturb the acoustic signal.

Understanding the effects of a fluctuating sound speed profile on the various paths of the received multipath signal is important in order to separate out environmental effects from the desired signal. In order to be able to better perform physics-based signal processing, a variety of experiments have been conducted in recent years to study acoustic fluctuations. As an example, one such cruise that

took wide-ranging environmental measurements was the Kaui-Ex experiment that took place off the coast of Kauai in July 2003. [2] In addition to near-continuous probing of the acoustic channel using a variety of vertical and bottom mounted arrays, oceanographic measurements were made of quantities such as the surface wave spectrum, 2D temperature structure, salinity, currents and bottom properties.

Complementary to the work done during Kauai-Ex, which can primarily be seen as dealing with understanding the forward problem, is the effort to invert an acoustic signal for the environment that gave it its unique signature. This work ranges from the contributions to geoacoustic inversion made by Gerstoft [3] to the shallow water acoustic tomography work by Cornuelle et. al.[4] and Hursky et. al. [5]

Time-reversal is a method of focusing sound in the ocean in range, depth and time that has proven remarkably robust to sound speed fluctuations. While time-reversal has been widely used in applications ranging from underwater communications to target detection, efforts to understand the reasons for its stability have been lacking. Fundamentally, this thesis can be seen as providing an explanation for the stability of time-reversal using some of the tools developed in seismic and acoustic tomography. Further, the same tools are utilized in an optimization framework together with a knowledge of fluctuation statistics to develop new sets of signals that can be made even more stable than time-reversal. This can be seen as an example of physics-based signal processing that was alluded to earlier.

## 1.2 Time-reversal

The first time-reversal experiment in the ocean was conducted by Parvulescu and Clay in 1965.[6, 7] The authors viewed the ocean as a black box that has a particular impulse response. Given an input signal $s(t)$ and an impulse response $h(t)$, the received signal $r(t)$ can be expressed as the convolution of the input signal

with the impulse response.

$$r(t) = s(t) \circledast h(t) \tag{1.1}$$

$$= \int_{-\infty}^{\infty} s(\tau)h(t-\tau)d\tau \tag{1.2}$$

Recognizing that a convolution operation with one of the signals reversed in time is the same as correlating the two signals, they were able to use the ocean as a 'correlator' by time-reversing and retransmitting an approximation to the impulse response, i.e. by recording and transmitting $h(-t)$, they were able to obtain a received signal that is the autocorrelation of $h(t)$. Of course, there is the possibility that the impulse response may have changed between the time of recording and retransmitting, in which case the received signal will be the cross-correlation of two impulse responses. The correlation peak is akin to a focal spot at the location of the source, whose quality (peak power, peak-to-sidelobe ratio) will depend on the degree of similarity between the two impulse responses. Fig. 1.1, taken from Parvulescu[7], is a simple schematic of how time-reversal works. Time-reversal of the impulse response and subsequent retransmission will cause each pulse to elicit a response. One of the paths for each response will arrive at exactly the same time, and due to the linearity of the hydrophone response, the pressure at this time will be exactly three times those of the sidelobes. One can thus see that the larger the number of multipaths, the higher will be the peak relative to the sidelobes.

Time-reversal is a time-domain concept whose equivalent in the frequency domain is phase conjugation. Phase conjugation was originally employed in non-linear optics where medium nonlinearities are used to scatter incident light in a way that the resulting scattered signal is a phase-conjugated version of the incident radiation. [8]The scattering medium is called a phase conjugating mirror, and just like in acoustics, takes advantage of the time-reversal invariance of the wave equation. In addition to the invariance property, time-reversal also takes advantage of reciprocity in the medium, i.e. the response of the medium is the same whether going from source to receiver or receiver to source.

Following a number of years of attention in the optics community, phase conjugation regained prominence in acoustics after a series of ultrasonics experiments by Fink et. al. [9, 10] who demonstrated focusing of sound using time
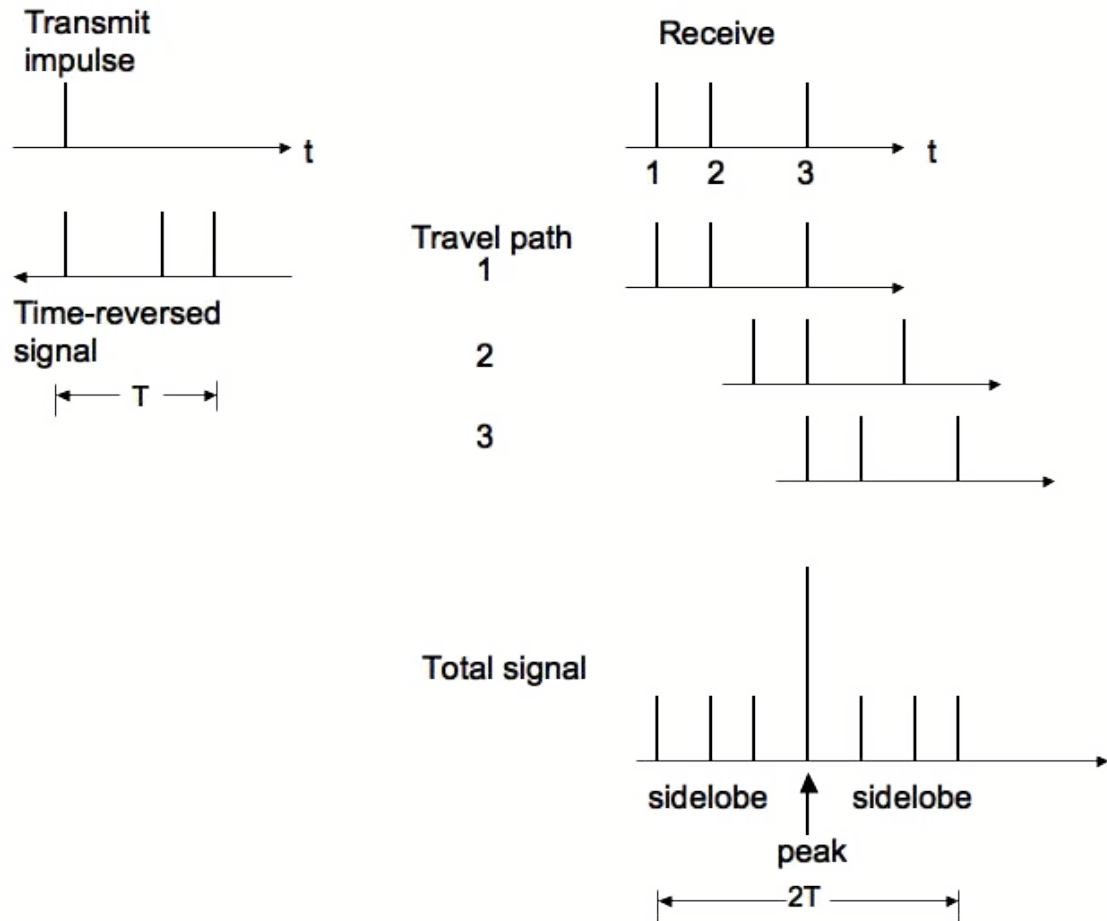
Figure 1.1: A schematic for how time-reversal works, based on Parvulescu and Clay.[6]

reversal mirrors. In one of the first experiments, a closed cavity containing a source is surrounded by transducers. Sound emitted by the source is scattered by heterogeneities in the cavity and recorded by the surrounding transducers. Upon emitting the time-reversed version of the recording, it was seen to focus back on the source location. This experiment showed promise in the ability of sound focused by time-reversal in biological stone destruction. Another experiment showed that if the medium is weakly homogeneous (dominated by single scattering), then a time-reversal mirror can produce a focal spot comparable to that of a closed-cavity, whose realization can be difficult in practice.

Around the same time that Fink et. al. were conducting the ultrasonic time-reversal experiments, Jackson and Dowling [11] proposed the viability of phase conjugation as a means of solving many longstanding problems in underwater acoustics. The behavior of phase conjugate arrays in underwater acoustics was studied through several examples and the effects of aperture size and inhomogeneities in medium propagation were treated for both near-field and far-field regions.

The first time-reversal array experiment in the ocean was conducted by Kuperman et. al. [12] in the Mediterranean Sea in 1996. This experiment successfully demonstrated focusing in the ocean waveguide at a distance of 6.3 km using a 50 ms pulse centered at 445 Hz. In addition to showing that the ocean acoustic experiments were consistent with theory, the stability of the focal spot was studied, and found to be robust for a time period of over an hour. The success of this proof-of-concept experiment in 1996 paved the way for a series of time-reversal experiments in the region conducted by the same group, and were termed the Focused Acoustic Fields (FAF) experiments. These experiments [13, 14, 15, 16] studied the utility of time-reversal in a variety of applications, ranging from underwater communications to buried target detection. Some of these applications will be described in the following section. In addition, the experiments also examined the stability of the focal spot for a number of ranges, frequencies and depths, providing valuable insight into the physics of time-reversal in the ocean. The data gathered during one of these experiments, FAF 2005, is used in this thesis while studying the stability aspects of the time-reversal focus.

## 1.2.1 Applications of Time-reversal

The ability of time-reversal to focus sound in space and time lends its itself to a wide variety of applications. Time-reversal, when proposed by Parvulescu and Clay[6], was seen as a way of allowing the ocean to perform the correlation process, thus saving on the limited computational resources available at the time. When phase conjugation was later proposed in optics, it was seen as having potential applications in adaptive optics, lenseless imaging, phase-conjugate resonators and

image processing[17].

Time-reversal in ultrasonics[10] was originally proposed as a way of performing lithotripsy (destruction of biological stones), by virtue of being able to focus sound inside a cavity. In addition, it was found that iterative time-reversal in the presence of multiple scatterers tends to converge to a focus on the strongest scatterer. This aspect of time-reversal, while also having biomedical applications, has been used in non-destructive testing to detect small surface anomalies.

In underwater acoustics, the most popular use of time-reversal has been in the area of underwater communications. The idea was first proposed by Roux [18], who recognized that time-reversal has the ability to mitigate the effects of multipath, which have long plagued underwater communications. In communications, where several symbols are transmitted one after the other, multipath causes the 'echos' associated with any one symbol to overlap with the other symbols, causing what is termed inter-symbol interference (ISI). Typically, communication receivers are built to remove ISI using signal processing tools known as equalizers[19]. Time-reversal, on the other hand exploits multipath, by effectively delaying each multipath such that all the different paths arrive at the same time, causing a focal spot. Edelmann[14] showed that it is possible to encode phase information in the time-reversed Green's function that can then be recovered at the receiver end. The use of the time-reversed Green's function as a communication symbol has the advantage of significantly reduced ISI due to the creation of a focal spot for each symbol. The ISI suppression achieved by time-reversal is often insufficient for higher data rate communications, or multiple-input multiple-output (MIMO) communications [20], in which case time-reversal is typically followed by receiver side equalization.

Other uses of time-reversal in underwater acoustics include its use as an acoustic barrier [21] and to detect buried objects[22]. In the acoustic barrier experiment, a disturbance in the focal plane is used to alert the presence of a foreign object between the source and receiver. When used for target detection, the ability of time-reversal to focus on a target results in less energy interacting with rough ocean boundaries above and below the focal spot. This give rise to an enhanced echo-to-reverberation ratio which can be exploited to localize the target.

### 1.2.2   Stability of Time-reversal

A highly attractive aspect of time-reversal, besides its focusing ability, is the fact that the focus produced by a particular Green's function can persist for a while. This happens despite the fact that the Green's function between the acquisition and subsequent retransmissions has changed. At lower frequencies (445 Hz), it was found that the focal spot persists for several hours upto a week [13]. At higher frequencies (3.5 kHz), the focal spot persisted for about an hour [15]. The authors examined fluctuations of the time-reversal focal spot using the waveguide invariant. They found that, in the presence of internal wave induced fluctuations, the focal spot merely shifted in range, but was still present at a different location. While the explanation is valid for a single frequency, or the narrowband case, the translation to a broadband scenario is not entirely obvious. Recent experiments (FAF 2005) were carried out using a 1 kHz bandwidth centered around 3.5 kHz. Various other explanations have also been put forth to explain the stability of the focus, which are examined in more detail in Chapter 2.

## 1.3   Motivation and purpose

This thesis can be seen as an attempt to explain the stability of the time-reversal focal spot that can be applied regardless of the specific characteristics of the time-reversal experiment such as geometry, frequency, bandwidth, etc. One constraint that is invoked is that the sound speed perturbations that cause a degradation of the focal spot be small enough to satisfy the single scattering assumption (first Born approximation). It is also assumed that changes to the focal spot are caused solely by sound speed fluctuations, and the effects of features such as surface waves and non-linear internal waves are negligible. This is because non-linear internal waves have been observed[23] to cause horizontal refraction of acoustic energy. While the analysis in this thesis can easily be extended to three dimensions, only two-dimensional effects are considered at this time.

A change in the pressure of the focal spot due to a change in the sound speed profile can be thought of as a pressure sensitivity to sound speed perturbations.

Time-reversal has been observed to have a lower pressure sensitivity than a simple pulse transmission. Given this line of reasoning, it becomes apparent that the use of a formal sensitivity analysis framework can yield potentially useful results.

The FAF experiment that was conducted in July 2005 in the Mediterranean sea focused on several aspects of time-reversal and time-reversal communications using vertical line arrays and billboard arrays. The focal spot was seen to persist for about an hour at 3.5 kHz with a 1 kHz pulse bandwidth. In addition to the time-reversal segment, the experiment also contained a portion where Green's functions were acquired every 20 seconds over 8 hours. Given the availability of Green's functions, the time-reversal focus can be passively constructed on the computer, and a variety of focusing scenarios can be studied.

In addition to the rich acoustic dataset available, the experiment also gathered CTD (conductivity-temperature-depth) profiles and temperature time-series over 12 days using two moored thermistor chains. The availability of acoustic and environmental data allows for a detailed study of fluctuations and their effect on time-reversal.

The main questions that this thesis addresses can thus be summarized as follows:

- Does time-reversal have a lower pressure sensitivity to sound speed fluctuations than a one-way transmission?

- Can sensitivity analysis be used to provide an answer why?

- Can knowledge of the pressure sensitivity be exploited to develop signals that are even less sensitive than time-reversal?

- Can knowledge of the pressure sensitivity be used to predict the behavior of the time-reversal focal spot?

The availability of the thermistor chain record also allowed for an additional investigation that could be useful in sensitivity studies and internal wave modeling. The hypothesis is that the temperature fluctuations observed are caused by repeated displacements of a background, or reference temperature profile. Thus,

given the thermistor chain record, it should be possible to invert for the reference profile using iterative methods. The last question question addressed in this thesis is therefore,

- Given a thermistor chain record, is it possible to invert for a background reference temperature profile?

## 1.4    Outline

This thesis is organized as follows[1]. Chapter 2 discusses the theory for sensitivity analysis applied to time-reversal acoustics by introducing pressure sensitivity kernels.[24] Two simple cases are considered: free-space and a Pekeris waveguide. Sensitivity kernels are illustrated for each case, and an argument is made for the reduction of sensitivity when time-reversal is used. The theory for pressure sensitivity kernels is then taken a step further, where the knowledge of pressure sensitivity is used to derive optimized source functions that are closely related to the inverse filter.[25] These functions contain adjustable parameters that allow for a tradeoff between focal spot quality and sensitivity to sound speed fluctuations. Various features of these functions are then illustrated for three simple perturbation scenarios: first, when medium perturbations are uncorrelated, second when there is a channel of zero perturbation variance in depth, and the third when perturbations have a long decorrelation scale.

Chapter 3 takes the theory developed in Chapter 2 and applies it to the FAF05 dataset. [26] An internal wave model is developed whose characteristics are matched to the environmental data available. It was found that the internal wave model, together with a parabolic equation acoustic code, was able to capture the of evolution of the peak of the time-reversal focal spot. This can be seen as a acoustic test of the internal wave model. Sensitivity kernels are then computed using experimentally gathered sound speed profiles and an attempt is made to track Green's functions as the evolve using these kernels. However, it was found that the

---

[1]Each chapter is essentially a full or partial reprint of papers that have been published, accepted, submitted or in preparation for submission to a professional journal. Therefore, each has been written in a paper format and is self-contained.

linear nature of the kernels limits the tracking ability to only about 10 minutes of fluctuations for the perturbation scenario encountered. Optimized source functions are then computed using the sensitivity kernels and the experimentally gathered Green's functions. Their performance is compared to time-reversal and the inverse filter for the given dataset and found to be in the right sense.

Chapter 4 deals with the problem of temperature profile estimation using the thermistor chain record. Thermistor chain data used belonged to the FAF06 experiment. A different set of thermistor chain data is used compared to Chapter 3 due to the closer depth and time-spacing available in the FAF06 thermistor chain data. This allowed for a better demonstration of the estimation method. The iterative Gauss-Newton method that is used is introduced and its application to the problem is discussed. The profile estimation algorithm is then applied to three different cases. The first two use synthetically generated data that have a known reference temperature while the third uses the FAF06 temperature data to estimate an unknown reference. The first synthetic data case study uses randomly generated temperature samples, while the second uses the internal wave model to generate temperature time-series.

# Bibliography

[1] W. A. Kuperman and J. F. Lynch. Shallow-water acoustics. *Physics Today*, 57:55–61, 2004.

[2] M. B. Porter, P. Hursky, M. Siderius, M. Badiey, J. Caruthers, W. S. Hodgkiss, K. Raghukumar, D. Rouseff, W. Fox, C. Moustier, B. Calder, B. J. Kraft, K. McDonald, P. Stein, J. K. Lewis, and S. Rajan. Kauaiex: Environmental effects on hf acoustic propagation with application to communications. *J. Acoustic Soc. Am.*, 115:2468–2468, 2004.

[3] P. Gerstoft. Inversion of seismo-acoustic data using genetic algorithms and a posteriori probability distributions,. *J. Acoustic Soc. Am.*, 95:770–782, 1994.

[4] B. Cornuelle, M. Dzieciuch, and E. Skarsoulis. Wave-theoretic kernels for long-range ocean travel-time measurement. *J. Acoustic Soc. Am.*, 119:3248, 2006.

[5] P. Hursky, M. B. Porter, B. D. Cornuelle, W. S. Hodgkiss, and W. A. Kuperman. Adjoint modelling for acoustic inversion. *J. Acoustic Soc. Am.*, 115:607–619, 2004.

[6] A. Parvulescu and C. S. Clay. Reproducibility of signal transmissions in the ocean. *Radio Electron Eng.*, 29:223–228, 1965.

[7] A. Parvulescu. Matched-signal ("MESS") processing by the ocean. *J. Acoustic Soc. Am.*, 98(2):943–960, 1995.

[8] B. Y. Zel'Dovich, N. F. Pilipetsky, and V. V. Shkunov. *Principles of phase conjugation*. Springer-Verlag, Berlin, 1985.

[9] M Fink, C. Prada, F. Wu, and D. Cassereau. Self-focusing with time reversal mirror in inhomogeneous media. *Proc. IEEE Ultrason. Symp. 1989 Montreal*, 2:681–686, 1989.

[10] M. Fink. Time-reversal mirrors. *Journal of Physics D: Applied Physics*, 26(9):1333–1350, 1993.

[11] D. R. Jackson and D. R. Dowling. Phase conjugation in underwater acoustics. *J. Acoustic Soc. Am.*, 89:171–181, 1991.

[12] W. A. Kuperman, W. S. Hodgkiss, H. C. Song, T. Akal, C. Ferla, and D. R. Jackson. Phase conjugation in the ocean: Experimental demonstration of an acoustic time-reversal mirror. *J. Acoustic Soc. Am.*, 103:25–40, 1998.

[13] W. S. Hodgkiss, H. C. Song, W. A. Kuperman, T. Akal, C. Ferla, and D. R. Jackson. A long-range and variable focus phase-conjugation experiment in shallow water. *J. Acoustic Soc. Am.*, 105:1597–1604, 1999.

[14] G. F. Edelmann, T. Akal, W. S. Hodgkiss, S. Kim, W. A. Kuperman, and H. C. Song. An initial demonstration of underwater acoustic communication using time-reversal. *IEEE J. Oceanic Engineering*, 27:602–608, 2002.

[15] S. Kim, W. A. Kuperman, W. S. Hodgkiss, H. C. Song, and G. F. Edelmann. Robust time-reversal focusing in the ocean. *J. Acoustic Soc. Am.*, 114:145–157, 2001.

[16] H. C. Song, W. A. Kuperman, W. S. Hodgkiss, T. Akal, and C. Ferla. Iterative time reversal in the ocean. *J. Acoustic Soc. Am.*, 105:3176–3184, 1999.

[17] D. M. Pepper. Applications of optical phase conjugation. *Scientific American*, 254:74–83, 1986.

[18] P. Roux. Time-reversal mirrors: Application to waveguide propagation and characterization of fluid flows (French). *Phd thesis, University of Paris*, 1997.

[19] M. Stojanovic. Recent advances in high-speed underwater acoustic communications. *IEEE J. Oceanic Engineering*, 21:125–136, 1996.

[20] H. C. Song, W. S. Hodgkiss, W. A. Kuperman, T. Akal, and M. Stevenson. Multiuser communications using passive time reversal. *IEEE J. Oceanic Engineering*, 32:915–926, 2007.

[21] H. C. Song, W. A. Kuperman, W. S. Hodgkiss, T. Akal, and P. Guerrini. Demonstration of a high-frequency acoustic barrier with a time-reversal mirror. *IEEE J. Oceanic Engineering*, 28:246–249, 2003.

[22] S. Kim, W. A. Kuperman, W. S. Hodgkiss, H. C. Song, G. F. Edelmann, and T. Akal. Echo-to-reverberation enhancement using a time-reversal mirror. *J. Acoustic Soc. Am.*, 115(4):1525–1531, 2004.

[23] S. D. Frank, M. Badiey, J. F. Lynch, and W. L. Siegmann. Experimental evidence of three-dimensional acoustic propagation caused by nonlinear internal waves. *JASA*, 118:723–734, 2005.

[24] K. Raghukumar, Bruce D. Cornuelle, William S. Hodgkiss, and William A. Kuperman. Pressure sensitivity kernels applied to time-reversal acoustics. *J. Acoustic Soc. Am.*, 124:98–112, 2008.

[25] M. Tanter, J. L. Thomas, and M. Fink. Time-reversal and the inverse filter. *J. Acoustic Soc. Am.*, 108:223–234, 2000.

[26] K. Raghukumar, Bruce D. Cornuelle, William S. Hodgkiss, and William A. Kuperman. Experimental demonstration of pressure sensitivity kernels. *J. Acoustic Soc. Am.*, 2009, to be submitted.

# Chapter 2

# Pressure Sensitivity Kernels Applied to Time-reversal Acoustics

Sensitivity kernels for receptions of broadband sound transmissions are used to study the effect of the transmitted signal on the sensitivity of the reception to environmental perturbations. A first-order Born approximation is used to obtain the pressure sensitivity of the received signal to small changes in medium sound speed. The pressure perturbation to the received signal caused by medium sound speed changes is expressed as a linear combination of single-frequency sensitivity kernels weighted by the signal in the frequency domain. This formulation can be used to predict the response of a source transmission to sound speed perturbations. The stability of time-reversal is studied and compared to that of a one-way transmission using sensitivity kernels. In the absence of multipath, a reduction in pressure sensitivity using time-reversal is only obtained with multiple sources. This can be attributed both to the presence of independent paths and to cancellations that occur due to the overlap of sensitivity kernels for different source-receiver paths. The sensitivity kernel is then optimized to give a new source transmission

14

scheme that takes into account knowledge of the medium statistics and is related to the regularized inverse filter.

## 2.1 Introduction

Time-reversed acoustics, due to its ability to focus energy in space and time, has found numerous applications ranging from underwater and wireless communications to medical ultrasound therapy. [1, 2, 3] Time-reversal works by transmitting a signal which is a time-reversed version of the observed Green's function between a source and receiver. This scheme assumes that the Green's function has not significantly changed between its acquisition and time-reversed retransmission. Despite this assumption, the ability of time-reversal to produce a focal spot has been found to be remarkably robust to environmental changes. In the ocean, the focal spot has been shown to persist for a week at 445 Hz (50 ms pulse)[4], and close to an hour at 3.5 kHz (10 ms pulse). [5]

Various explanations have been offered to understand the reason for the robustness of time-reversal to environmental perturbations. Kim et al.[5], using the theory of waveguide invariants for an oceanic waveguide, showed that while there is little degradation in the intensity of the focal spot, it is seen to shift back and forth in range as a result of internal wave induced sound speed fluctuations. While any one realization of the focal spot may or may not be stable, an ensemble average of focal spots tends to have high stability.[6] The presence of spatial diversity (large arrays) has the same effect as an ensemble average and results in stability of the focal spot. In random media[7], the probability of a realization of the focal spot differing significantly from its expected value is small. This feature was referred to as the self-averaging property of the focal spot which leads to the statistical stability of time-reversal for broadband signals. The self-averaging property is based on specific asymptotic limits more suited to optical and infrared time-reversal than sonar or ultrasound.

The above contributions suggest the use of a formal sensitivity analysis to analyze the stability of the time-reversal focal spot with respect to sound speed

perturbations. Sensitivity, when defined as the derivative of the received pressure signal with respect to medium sound speed fluctuations, provides a way to compare time-reversal transmissions to one-way transmissions. Sensitivity kernels can be a useful tool for analyzing various transmission schemes that have been proposed that seek to provide an even more stable focal spot[5], or a focal spot with reduced spatio-temporal sidelobes.[8, 9] The present work develops a pressure sensitivity kernel that can be used with a variety of source transmissions. The sensitivity kernels obtained for different source transmissions can be used as a performance measure to study the effect of medium sound speed fluctuations on the received signal. As an example, time-reversal is compared to a one-way transmission, and an explanation is provided for the lower sensitivity of time-reversal. The ability to express the received pressure perturbation as a function of the sensitivity kernel allows for the development of a regularized version of the inverse filter [10], with a physically relevant regularization. In this paper, source transmissions may sometimes be referred to as source functions, or source shading functions (for an array of sources) in order to explicitly denote the time, frequency or spatial dependence of the source transmission. This paper can be seen as primarily providing a theoretical framework, which is then visualized using a simple acoustic propagation scenario. Free space acoustic propagation, followed by a Pekeris waveguide, is used to visualize various sensitivity kernels.

Wave-theoretic sensitivity kernels were first proposed in seismology as a finite-frequency tomography alternative to the more commonly used time-of-arrival tomography. [11, 12, 13] A key contribution was in revealing that it is possible to have zero sensitivity to sound speed perturbations along a ray path, while having non-zero sensitivities in the region surrounding a ray path. More recently, travel-time sensitivity kernels for ocean-acoustic tomography were developed and were shown to exhibit similar properties to those developed in seismology. [14] These kernels are currently being employed to invert for sound speed perturbations in a shallow water waveguide using broadband acoustic signals. [15] All of these kernels make use of a first-order Born approximation, which results in a linear relation between the sound speed perturbation and either the induced pressure perturbation

in the Green's function or a travel-time perturbation. The first Born approximation restricts the use of these sensitivity kernels to linear regimes where the sound speed perturbation is small compared to the background sound speed profile. For larger perturbations, non-linearities result, which can, to an extent, be handled by iterative adjoint methods. [16] As a result of the first-order Born approximation, it is assumed that the Green's function used as a source transmission in time-reversal represents an unperturbed medium, and that medium perturbations are restricted to a linear regime.

The contents of this work are organized as follows. In Sec. II, pressure sensitivity kernels are developed for the general case of an array of hydrophones transmitting to a single receiver (broadside transmission). The theory can be easily extended to a multiple-input multiple-output scenario. Sections III and IV show examples of sensitivity kernels in free space and for a Pekeris waveguide, respectively. The goal is to examine the sensitivity of time-reversal versus that of a one-way transmission. In a dispersionless propagation environment, and in the absence of a transmit array, there is no difference in sensitivity between time-reversal and a one-way transmission. As suggested in Roux et al.,[17] a reduction in sensitivity through time-reversal is only made in the presence of multiple sources, or multipath propagation. Sensitivity kernels for a source-receiver path have a Fresnel zone-like interference pattern, and a reduction in sensitivity for a finite-frequency, finite-bandwidth case is caused by an averaging of several kernels that correspond to multiple sources or multiple paths. Time-reversal results in each of the multiple paths arriving at the same time, as a consequence of which the sensitivity kernels for each of the paths add coherently to give an overall reduction in sensitivity. This holds true not just for time-reversal, but also for inverse-filters, or any transmission that results in the simultaneous arrival of different paths. In addition to the coherent cancellation of sensitivities, there is also an incoherent reduction in sensitivity that comes from independent paths having uncorrelated sound speed perturbations. The incoherent reduction, however, is not addressed in this paper.

In Sec. V, the sensitivity kernels are examined from an optimization point

of view, the goal being to design source functions that offer the flexibility of trading mainlobe width for increased robustness. Semi-analytic expressions for the optimized signals are offered, which result from a minimization of pressure perturbations together with a constraint on the focusing capabilities of the source function. This approach leads to an expression for the optimized source function which is an enhancement to the inverse filter.[18] Sec. VI presents the results of simulations in a Pekeris waveguide, where the optimized source function is compared to time-reversal and the inverse filter. Sensitivity kernels for the optimized source functions are presented, which explicitly use knowledge of fluctuation statistics to lower sensitivity to medium perturbations. Finally, Sec. VII contains a discussion of the results and draws conclusions from this work.

## 2.2    Pressure sensitivity kernels

The pressure perturbation to the Green's function $G(\boldsymbol{r}|\boldsymbol{r}_s)$ at a location $\boldsymbol{r}$ due to a harmonic point source of unit strength at location $\boldsymbol{r}_s$ can be expressed as

$$\Delta G(\boldsymbol{r}|\boldsymbol{r}_{\mathrm{s}}) = -2\omega^2 \int_V G(\boldsymbol{r}|\boldsymbol{r}')G(\boldsymbol{r}'|\boldsymbol{r}_{\mathrm{s}})\frac{\Delta c(\boldsymbol{r}')}{c^3(\boldsymbol{r}')}d\boldsymbol{r}' \qquad (2.1)$$

This is called the first Born approximation.[19] It is also called the single- or weak-scattering approximation, or wave-field linearization, and is widely used in connection with scattering problems.[20] It is a linear relation between the perturbation in the sound-speed distribution and the induced perturbation in the Green's function. The integration volume in eq. 2.1 is all space or the region encompassing the source and receiver over which sound speed perturbations result in perturbations to the Green's function.

A key assumption upon which the validity of the first order Born approximation rests is that $\Delta c/c$, integrated over the volume, be small. A consequence of the volume integration in eq. 2.1 is that the validity of the first Born approximation in a waveguide will depend on the path length. Longer path lengths will result in the linear approximation breaking down at smaller sound speed perturbations than for shorter path lengths. The effect of non-linearities was seen to start to

creep in for a $\Delta c$ of 4 $ms^{-1}$ with a background sound speed of around 1500 $ms^{-1}$. [21]

The Green's function above is defined in the frequency-domain - the circular frequency $\omega$ enters the Helmholtz equation as a parameter. Further, the Green's function depends on the sound-speed distribution which also enters the Helmholtz equation. In order to explicitly note these dependencies, $G$ is written in the following as $G(\boldsymbol{r}|\boldsymbol{r}_\mathrm{s};\omega;c)$.

For a single point source the resultant pressure field can be written as

$$P(\boldsymbol{r}_r;\omega;c) = G(\boldsymbol{r}_r|\boldsymbol{r}_s;\omega;c)S(\boldsymbol{r}_s;\omega) \tag{2.2}$$

where $P(\boldsymbol{r}_r;\omega;c)$ is the frequency-domain pressure at receiver location $\boldsymbol{r}_r$, from a source located at $\boldsymbol{r}_s$. $G(\boldsymbol{r}_r|\boldsymbol{r}_s;\omega;c)$ is the frequency-domain Green's function that turns pressure at the source at frequency $\omega$ to pressure at the receiver. $S(\boldsymbol{r}_s;\omega)$ is the signal at source $\boldsymbol{r}_s$ at frequency $\omega$. For an array transmitting to a single receiver, the received signal is given by adding up all source contributions:

$$P(\boldsymbol{r}_r;\omega;c) = \sum_{i=1}^{N_s} G(\boldsymbol{r}_r|\boldsymbol{r}_{si};\omega;c)S(\boldsymbol{r}_{si};\omega) \tag{2.3}$$

where $\boldsymbol{r}_{si}$ is the location of the $i^{th}$ source element, and $N_s$ is the number of source elements.

In the time-domain, the received signal is then given by

$$P(\boldsymbol{r}_r;t;c) = \sum_{i=1}^{N_s} \int_{-\infty}^{\infty} G(\boldsymbol{r}_r|\boldsymbol{r}_{si};t-t';c)S(\boldsymbol{r}_{si};t')dt' \tag{2.4}$$

It is seen from eq. 2.4 that, in the case of an array-to-a-point transmission, the time-domain Green's function has been accumulated over source and time, weighted by $S$, as opposed to a point-to-point transmission where the Green's function is only accumulated over time. For now, a heuristic argument can be made that this additional spatial averaging could make the received signal more stable. This will be shown more rigorously in Sec. VI.

In a perturbed propagation environment, the frequency domain perturbation to the received pressure can be approximated by substituting the perturbed

Green's function into eq. 2.3

$$\Delta P(\boldsymbol{r}_r; \omega; c) = \sum_{i=1}^{N_s} \Delta G(\boldsymbol{r}_r|\boldsymbol{r}_{si}; \omega; c) S(\boldsymbol{r}_{si}; \omega) \tag{2.5}$$

Using eq. 2.1 for the perturbed Green's function

$$\Delta P(\boldsymbol{r}_r; \omega) = \sum_{i=1}^{N_s} \left( -2\omega^2 \int_V G(\boldsymbol{r}_r|\boldsymbol{r}; \omega; c) G(\boldsymbol{r}|\boldsymbol{r}_{si}; \omega; c) \frac{\Delta c(\boldsymbol{r})}{c^3(\boldsymbol{r})} )d\boldsymbol{r} \right) S(\boldsymbol{r}_{si}; \omega) \tag{2.6}$$

Exchanging the order of integration and summation will yield the effective pressure sensitivity kernel.

$$
\begin{aligned}
\Delta P(\boldsymbol{r}_r; \omega) &= -2\omega^2 \int_V \left( \sum_{i=1}^{N_s} G(\boldsymbol{r}_r|\boldsymbol{r}; \omega; c) G(\boldsymbol{r}|\boldsymbol{r}_{si}; \omega; c) \frac{\Delta c(\boldsymbol{r})}{c^3(\boldsymbol{r})} S(\boldsymbol{r}_{si}; \omega) \right) d\boldsymbol{r} \\
&= \int_V \left( \sum_{i=1}^{N_s} K_{pp}^i(\boldsymbol{r}; \omega; c) \right) \Delta c(\boldsymbol{r}) d\boldsymbol{r} \\
&= \int_V K_{ap}(\boldsymbol{r}; \omega; c) \Delta c(\boldsymbol{r}) d\boldsymbol{r} \tag{2.7}
\end{aligned}
$$

where $K_{pp}^i(\boldsymbol{r}; \omega; c)$ is the sensitivity of the received pressure for a receiver located at $\boldsymbol{r}_r$ to a sound speed perturbation at location $\boldsymbol{r}$, for the single source with index $i$ located at $\boldsymbol{r}_{si}$.

$$
\begin{aligned}
K_{pp}^i(\boldsymbol{r}; \omega; c) &= -2\omega^2 G(\boldsymbol{r}_r|\boldsymbol{r}; \omega; c) G(\boldsymbol{r}|\boldsymbol{r}_{si}; \omega; c) \frac{1}{c^3(\boldsymbol{r})} S(\boldsymbol{r}_{si}; \omega) \\
&\equiv M_{pp}^i(\boldsymbol{r}; \omega; c) S(\boldsymbol{r}_{si}; \omega) \tag{2.8}
\end{aligned}
$$

and $K_{ap}(\boldsymbol{r}; \omega; c)$ is the sensitivity of the received pressure to a sound speed perturbation at location $\boldsymbol{r}$, for an array of sources transmitting to a single receiver. $M_{pp}^i$ can be recognized as part of the integrand in eq. 2.1, i.e. integrating $M_{pp}^i$ times the sound speed perturbation over the region between source and receiver will give the Born approximation to the perturbed Green's function.

Eq. 2.7 is a linear relation between the pressure perturbation at the receiver and sound speed perturbations in the medium, valid when $\Delta c/c$ is sufficiently small.

Eqs. 2.7-2.8 provide the framework for studying the effect of source transmission schemes on the received pressure perturbation. Replacing $S(\boldsymbol{r}_S; \omega)$ by

$G^*(\boldsymbol{r}_r|\boldsymbol{r}_s; \omega; c)$, will result in an expression for the pressure perturbation for a time-reversal scheme. Replacing $S(\boldsymbol{r}_s; \omega)$ by $1/G(\boldsymbol{r}_r|\boldsymbol{r}_s; \omega; c)$ will result in an expression for the pressure perturbation for a scheme involving inverse filters.[18]

Finally, an additional way of looking at eq. 2.7 is in terms of an optimization problem where the goal is to obtain a set of source transmissions that will minimize the pressure perturbations at the receiver. This is more fully explored in Sec. V.

## 2.3 Free space sensitivity kernels

As a first step towards visualizing pressure sensitivity kernels, the analytical framework developed in Sec. II is applied to acoustic propagation in free space. The analytical framework for free space closely follows that of Skarsoulis.[14]

### 2.3.1 Analytical results

The complex amplitude of the 3-D Green's function between a point source located at $\mathbf{r}_s$ and receiver at $\mathbf{r}_r$ in a medium with uniform background sound speed $c$ has the form,

$$G_s(\omega) = \frac{e^{ikR}}{4\pi R} \qquad (2.9)$$

where $R = |\mathbf{r}_S - \mathbf{r}_r|$ is the source-receiver distance, $k = \omega/c$.

Scatterers in the medium between source and receiver, each of which contribute a sound speed perturbation $\Delta c(x, y, z)$ will cause a perturbation to the Green's function (eq. 2.1). Denoting the distance from the source to a scatterer (sound speed anomaly) by $R_1$ and from the scatterer to the receiver by $R_2$, the perturbation to the received pressure will be

$$\Delta P(\omega) = \frac{-2\omega^2}{(4\pi)^2 c^3} \int \int \int \frac{e^{ik[R_1(x,y,z)+R_2(x,y,z)]}}{R_1(x, y, z) R_2(x, y, z)} S(\omega) \Delta c(x, y, z) dx dy dz \qquad (2.10)$$

From eq. 2.10 and eq. 2.8, the free space sensitivity kernel for a single source-receiver pair is

$$K_{pp}(x, y, z; \omega) = \frac{-2\omega^2}{(4\pi)^2 c^3} \frac{e^{ik[R_1(x,y,z)+R_2(x,y,z)]}}{R_1(x, y, z) R_2(x, y, z)} S(\omega) \qquad (2.11)$$

The three-dimensional pressure sensitivity kernel can be reduced to two-dimensions by integrating eq. 2.11 over the horizontal cross-range dimension. This assumes that the sound speed anomalies between source and receiver do not vary in the horizontal cross-range direction. Next, the continuous-valued kernel in eq. 2.11 can be discretized by integrating eq. 2.11 without the source term over grid cells (Fig. 2.1), with the sound speed anomaly assumed to be constant over each cell. These two operations yield the integrated pressure sensitivity for each grid cell (eq. 2.8),

$$M_{pp}^i(x_n, z_m; \omega) = \frac{-2\omega^2}{(4\pi)^2 c^3} \int_{-y_0}^{y_0} \int_{x_n-dx/2}^{x_n+dx/2} \int_{z_m-dz/2}^{z_m+dz/2} \frac{e^{ik[R_1(x_n,y,z_m)+R_2(x_n,y,z_m)]}}{R_1(x_n,y,z_m)R_2(x_n,y,z_m)} dz dx dy$$
(2.12)

Eq. 2.12 is numerically evaluated in Section V.

Eq. 2.12, multiplied by a source function will yield the point-to-point sensitivity kernel (eq. 2.11), following which the pressure perturbation can be calculated using eq. 2.10.

It is helpful to look at the time domain pressure sensitivity equations for the simple case of free space propagation using both a unity frequency domain source function and the phase conjugated Green's function as source functions.

For a one-way transmission, $S(\omega) = 1$ (delta function in time, centered at $t = 0$). This will result in a single arrival at time $t = R/c = T$. Hence, the time-domain sensitivity kernel for pressure at the time of the peak arrival is evaluated at time $t = R/c$. For time-reversal, the shape of the spectrum stays the same, but the signal is phased and shaded in such a way that the source function $S(\omega) \sim \frac{e^{-ikR}}{R}$. This phasing will result in the single arrival occurring at time $t = 0$, as opposed to the one-way transmission where the arrival occurs at $t = R/c = T$. Hence, for time reversal, the sensitivity kernel for pressure at the time of the peak arrival is evaluated at time $t = 0$. The sensitivity kernel at the time of an arrival provides quantitative information about the sensitivity of the pressure amplitude of the peak of the arrival to sound speed perturbations at any point in the medium. Henceforth, the term time-domain sensitivity kernel is used to denote time-domain pressure sensitivity for a particular time, usually the peak of an arrival, to sound speed perturbations.

Using the appropriate source function $S(\omega)$, and applying the inverse Fourier transform to eq. 2.11 will give the time-domain sensitivity kernels for point-to-point and time-reversal transmissions,

$$
\begin{aligned}
K_{pp}(t) &= \frac{2}{(4\pi)^2 c^3 R_1 R_2} \int_\infty^\infty -\omega^2 e^{i\omega(T_1+T_2-t)} d\omega = \frac{1}{(4\pi)^2 c^3 R_1 R_2} \delta''(T_1 + T_2 - t) \\
K_{tr}(t) &= \frac{2}{(4\pi)^2 c^3 R_1 R_2} \int_\infty^\infty -\omega^2 e^{i\omega(T_1+T_2-T-t)} d\omega = \frac{1}{(4\pi)^2 c^3 R_1 R_2} \delta''(T_1 + T_2 - T - t)
\end{aligned}
$$

$$(2.13)$$

where $\delta(.)$ is the Dirac delta function and $'$ denotes its time derivative, $T_1 = R_1/c$ and $T_2 = R_2/c$. The notation has been simplified to drop the explicit dependence of $R_1, R_2, T_1$ and $T_2$ on $x, y, z$. Eq. 2.13 for the time-domain pressure sensitivity kernels is similar to what was derived with respect to travel-time sensitivity kernels. [14]

Evaluating the sensitivity kernels at the respective arrival times will result in,

$$
\begin{aligned}
K_{pp}(t = T) &= \frac{2}{(4\pi)^2 c^3 R_1 R_2} \delta''(T_1 + T_2 - T) \\
K_{tr}(t = 0) &= \frac{2}{(4\pi)^2 c^3 R_1 R_2} \delta''(T_1 + T_2 - T)
\end{aligned}
$$

$$(2.14)$$

Thus, in the trivial case of a point-to-point transmission in free space, both time-reversal and a one-way transmission have identical pressure sensitivities.

In a finite frequency, finite bandwidth case, the infinite bandwidth Dirac delta function is replaced by a $\frac{sin(x)}{x}$ (sinc) form where the argument of the sinc function is given by $T_1 + T_2 - T$. As a result, the sensitivity kernel in eq. 2.14 can be approximated by the second derivative of the sinc function. This gives rise to a pattern in the range-depth space marked by lines over which $T_1 + T_2$ is constant, which is the broadband equivalent of the lines of constant phase in a single frequency Fresnel interference pattern.

## 2.3.2 Numerical results

A simple way to test the sensitivity kernels (eq. 2.8) from previous sections is to conduct numerical simulations involving acoustic propagation in free space

where there are sound speed anomalies $\delta c(x, z)$ in the medium between source and receiver.[14]
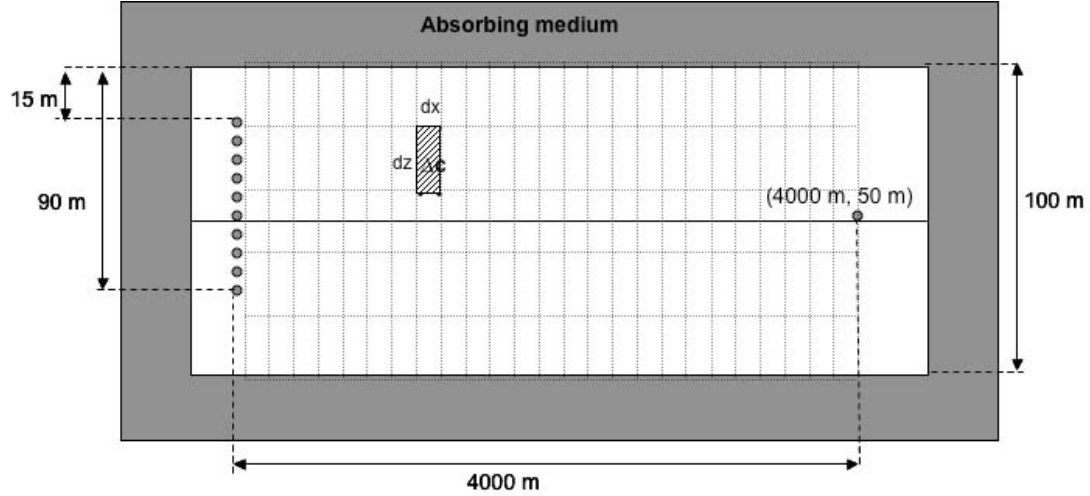


Figure 2.1: Computational geometry for free space sensitivity kernels

The scenario studied involves a two-dimensional area, $4000\ m$ in length and $100\ m$ in depth. While the theory developed here applies to three-dimensional geometries, the results are more easily visualized by integrating the three-dimensional pressure sensitivity kernel along the horizontal cross-range dimension (eq. 2.12). It was shown[22] that three-dimensional scattering effects become important only when the Fresnel width approaches and exceeds the cross-range coherence length of the sound speed perturbations. This is because, under such a scenario, out-of-plane scattering becomes important, which cannot be accounted for by 2-D models. As shown in the next section, the Fresnel width for pressure sensitivity kernels in the free space scenario considered is approximately $20\ m$. The cross-range scale for sound speed perturbations was assumed to be larger than $30\ m$, thus satisfying the criterion under which a two-dimensional example is sufficient to yield realistic results. As a result, it is possible to work in two dimensions by using sensitivity kernels that are integrated in the horizontal cross-range dimension. There are 10 transmit transducers spanning depths $15\ m$ to $90\ m$. The receive transducer

is at a range of $4000$ $m$ and at a depth of $50$ $m$. The background sound speed is assumed to be $1500$ $ms^{-1}$. The transducers operate at a central frequency of $3.5$ $kHz$ ($\lambda_C = 0.4$ $m$) with a bandwidth of $128$ $Hz$. These values are chosen to roughly reflect those used in recent ocean acoustics experiments. Fig. 2.1 shows the computational geometry employed to illustrate sensitivity kernels in free space. The size of each grid cell is $dx = 30$ $m$ by $dz = 2$ $m$. Sensitivity kernels are numerically integrated over three-dimensions for each grid cell. The size of the grid cell is representative of spatial coherence scales of sound speed perturbations in the ocean.[23]

Broadband Green's functions were calculated from each source to the domain and from the receiver to the domain (a finely sampled three-dimensional grid cell), over the $128$ $Hz$ bandwidth centered around $3.5$ $kHz$, using a frequency step of $1$ $Hz$. The product of the two Green's functions is then numerically integrated over each grid cell. This allows for the calculation of the frequency-domain sensitivity kernel according to eq. 2.12. An FFT is then applied to the frequency-domain sensitivity kernels at each grid point, which results in a time-series of sensitivity for each cell. For each cell, the value of the sensitivity time-series at the time of an unperturbed arrival is the time-domain pressure sensitivity for the arrival. This may be expressed as

$$K(t) = \int_{-\infty}^{\infty} M(\omega)S(\omega)e^{-i\omega t}d\omega \qquad (2.15)$$

For a one-way point-to-point transmission, $M(\omega) = M_{pp}^i(\omega)$, $S(\omega) = 1$ and $t = R/c$. For a broadside transmission, $M(\omega) = \sum_{i=1}^{N} M_{pp}^i(\omega)$, $S(\omega) = 1$ and $t = R/c$. For a time-reversal mirror, $M(\omega) = \sum_{i=1}^{N} M_{pp}^i(\omega)$, $S(\omega) = G_{si}^*(\omega)$ and $t = 0$. The top left panel in Fig. 2.2 shows the time-domain pressure sensitivity kernels for the main (only) arrival, for one-way point-to-point transmissions between a source at $50$ $m$ and a receive element at $50$ $m$ depth, at a range of $4$ $km$. The structure of the sensitivity map shows an approximate Fresnel-zone behavior with an oscillatory structure. [14] The significance of the Fresnel zones is that within each zone, the phase difference between the interfering Green's functions is less than $\pi$. While the Fresnel zone is a single-frequency concept, the time-domain analogue, called the 'zone of influence' [24] is a weighted average of many single-frequency Fresnel

interference patterns. As the central frequency increases, the width of the zone of influence becomes smaller as the propagation becomes more ray-like. As the bandwidth increases, the higher order Fresnel zones of different frequencies begin to destructively interfere, and only the first zone of influence is discernible. The width of the central lobe of the kernel is approximately the same as that of the first Fresnel zone at the central frequency, given by [25]

$$R_F(r) = \sqrt{\frac{r(R-r)c}{fR}} \tag{2.16}$$

where $R$ is the source-receiver distance, $f$ is the central frequency of the signal, and $c$ is the sound speed. Taking $R = 4000\ m$, $r = 2000\ m$, $c = 1500\ m/s$ and $f = 3500\ Hz$, gives $R_F = 20.7\ m$, which is consistent with the observed value of approximately 20 m in Fig. 2.2. As $\omega \to \infty$, $R_F(r) \to 0$, and the wave-theoretic sensitivity kernel becomes the ray-theoretic kernel. The sensitivity on the source-receiver path is non-zero, which is different from 3-D travel-time sensitivity kernels which have zero sensitivity along the ray path. In seismic literature,[11] 3-D travel-time sensitivity kernels are often referred to as 'banana-doughnut' kernels with the 'banana' shape arising from the shape of the kernel as a result of refraction of the ray path, and the 'doughnut' referring to the region of zero sensitivity along the ray path. The non-zero sensitivity along the ray path has also been observed for 2-D travel-time kernels.[26] Because the 2-D kernel is obtained from the cross-range averaging of the 3-D kernel, the 2-D kernel has non-zero sensitivity along the ray path.

With an understanding of the pressure sensitivity kernels in place, it is now possible to study the effect of time-reversal on the sensitivity kernel. Any reduction in sensitivity obtained through time-reversal [27] may be thought of as a two-part process. First, there is the reduction in sensitivity, if any, obtained through the use of a time-reversed Green's function as a source function. Second, there is the effect of using an array of sources, which involves a phased sum of several one-way point-to-point kernels such as shown in Fig. 2.2. Thus, when studying the effect of time-reversal on sensitivity, it is helpful to break up the problem into a time-reversal part followed by an array gain part, or vice versa.
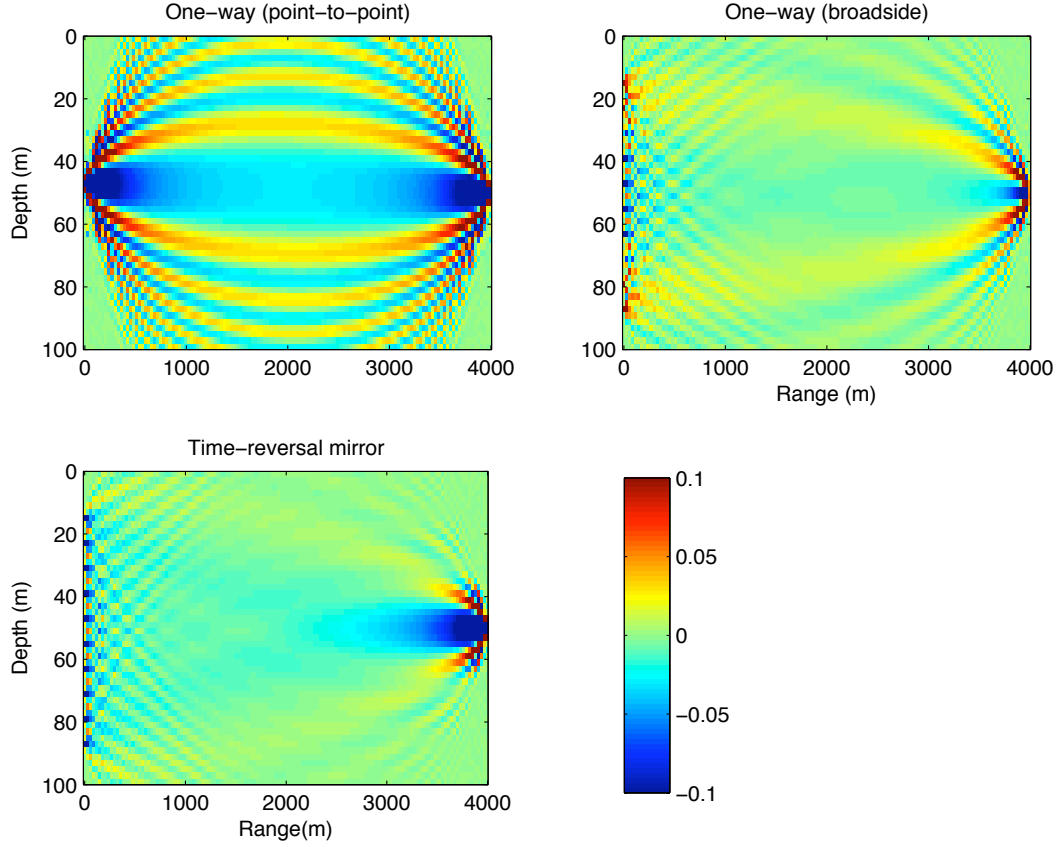
Figure 2.2: Time domain sensitivity kernels ($10^{-5}\mu Pa\ s\ m^{-4}$) evaluated at the peak of the arrival for: **Top Left** Point-point one-way, **Top Right** Array-to-point one-way (broadside) , **Bottom Left** Array-to-point time-reversal (time-reversal mirror). Receiver is on the right hand side of each plot, at a depth of 50 m.

The top right, and bottom panels in Fig. 2.2 show sensitivity, in the time-domain, for one-way and time-reversal transmissions involving an array transmitting to a single receiver. In the case of time-reversal, the power of the time-reversed Green's function has been normalized to have the same total power as the uniform source function used in a one-way transmission. Since the sensitivity kernels for the array-to-point kernels are a sum of individual point-to-point kernels, the array-to-point kernels have been divided by the number of sources. The broadside sensitivity kernel is computed by first summing the individual frequency-domain sensitivity kernels for each source, followed by evaluating the broadside time-domain sensitivity kernel at the time of arrival of a pulse from a source at 50 $m$ depth. This

is because the received signal for a broadside transmission consists of just a single arrival corresponding to a source at 50 $m$ depth since the difference in range between the various sources and the receiver is insufficient to produce several distinct direct arrivals. If there were indeed distinct arrivals, the broadside time domain sensitivity kernel would have to be evaluated at each of the arrival times.

The r.m.s values of sensitivities for the various schemes are listed in Table 2.1, divided by the r.m.s value for a one-way transmission. The r.m.s values are divided by the peak amplitude of the arrival for the one-way transmissions, or the peak amplitude of the focal spot for time-reversal. The statistical significance of using the r.m.s of the sensitivity kernel follows from eq. 2.7. For uncorrelated perturbations, the r.m.s of the sensitivity map is shorthand for the r.m.s of the expected pressure perturbation.

Point-to-point time-reversal is identical to a one-way transmission in terms of sensitivity (eq. 2.14). The use of time-reversal shows a reduction in sensitivity in free space only when used along with an array. For an array in free space, time-reversal results in a phasing of transmissions from different sources such that the peak of all arrivals occurs at the same time. The phased addition of several point-to-point sensitivity kernels results in a net cancellation of the oscillating Fresnel-like zones of influence. A given sound speed perturbation will be in the zone of influence of sensitivity kernels for multiple paths. When these paths are phased such that they all arrive at the same time, then evaluating the sensitivity at that time corresponds to an average of all the sensitivity kernels. Due to overlapping positive and negative regions of sensitivity, there is an overall reduction in sensitivity. As frequencies get larger, there are two effects that need to be considered. First, increasing the bandwidth results in the addition of kernels for each frequency, and this smears out the higher order zones of influence which reduces the overall r.m.s sensitivity. At the same time, there is less overlap of sensitivity kernels for the multiple paths. Second, increasing the central frequency results in a larger pressure sensitivity due to larger phase shifts. The combined effect is that time-reversal involving higher frequencies has a greater sensitivity to sound speed perturbations, as has been experimentally observed.[5]

In the example shown, the time-reversal mirror reduces the sensitivity of the peak magnitude to about two-thirds that of a broadside transmission. While the broadside transmission in this example also results in a single arrival, the alignment of the different peaks is not perfect, and the sensitivity of the peak of the arrival is larger than that for time-reversal.

Table 2.1: The r.m.s values for one-way and time-reversal free space sensitivity kernels, normalized to the sensitivity for a one-way transmission

| One-way (point-to-point) | Time-reversal (point-to-point) | Broadside (array-to-point) | Time-reversal mirror (array-to-point) |
| --- | --- | --- | --- |
| 1 | 1 | 0.48 | 0.33 |

## 2.4   Pekeris waveguide sensitivity kernels

The complex amplitude Green's function in a two-dimensional Pekeris waveguide for a source located at $(r_s, z_s)$ and a receiver at $(r, z)$ is given by [28]

$$G(r, z) = \frac{i}{4\rho(z_s)} \sum_{m=1}^{M} \psi_m(z_s)\psi_m(z)H_0^{(1)}(k_{rm}r) \qquad (2.17)$$

For mode $m$, $k_{rm}$ is the horizontal wavenumber, $\psi_m$ is the vertical mode shape and $H_0^{(1)}(k_{rm}r)$ is the Hankel function of the first kind. Eq. 2.17, along with eq. 2.8, will give the frequency-domain pressure sensitivity kernel for a Pekeris waveguide. The waveguide geometry for which the Pekeris sensitivity kernels are computed has dimensions identical to Fig.2.1, with the surrounding absorbing medium replaced by a pressure release surface and an absorbing bottom. The density and sound speed in the bottom are 1800 $kg/m^3$ and 1800 $m/s$ respectively. While it was relatively straightforward to compute closed form sensitivity kernels for free space propagation, the same is not true for the Pekeris waveguide. However, it can now be expected that multipath propagation will result in differences between time-reversal and one-way transmissions, as opposed to free space propagation where the two are identical for a point-to-point application.

Frequency-domain pressure sensitivity kernels are computed every 1 $Hz$ over a bandwidth of 1 $kHz$ with a central frequency of 3.5 $kHz$. The two-dimensional grid over which the sensitivity kernels are computed is sampled well

above the spatial Nyquist frequency in order to avoid spatial aliasing, with a depth step of $dz = 0.1\ m$ and a range step of $dr = 10\ m$. Unlike the 3-D free space sensitivity kernels, which were averaged over the cross-range dimension, no averaging is needed for the 2-D Pekeris waveguide example, since the Green's function in eq. 2.17 is specifically defined for a 2-D geometry. Green's functions for this example are on the order of $10^{-5}$, as a result of which sensitivity kernels will be on the order of $10^{-10}$. In order to avoid plotting these extremely small values, Green's functions are scaled up by $10^5$.

An inverse FFT of the frequency-domain sensitivity kernels in eq. 2.8 will result in a time series for each grid point. This time series is then sampled at times corresponding to the time of arrival of the various multipaths for a pulse propagating in the unperturbed medium. This will result in a number of sensitivity kernels, each of which corresponds to a particular multipath arrival. The resulting sensitivity kernels are broadband, and centered around the carrier frequency.

Fig. 2.3 shows the time-domain sensitivity kernels for a source located at a depth of $50\ m$ and a receiver located at the same depth, but $1000\ m$ away in range. The same Fresnel-like interference pattern as free space propagation is seen, centered around each ray path. The sensitivity kernel for the bottom bounce is seen to have the opposite polarity compared to the sensitivity kernel for the surface bounce. This is a result of a negative reflection coefficient associated with the surface bounce. Another feature of the sensitivity kernels in Fig. 2.3 is the reduction in sensitivity as the launch angle gets steeper. This is a direct consequence of Snell's law ($\frac{cos\ \theta}{c} = const,\ cos\ \theta = \frac{k_r}{k}, \frac{d\theta}{dc} \to 0$ as $\theta \to \pi/2$), where $\theta$ is the angle of incidence with respect to the horizontal. As $\frac{d\theta}{dc}$ gets smaller with an increasing angle of incidence ($\theta$), a reduction in sensitivity ($\frac{dP}{dc}$) follows.
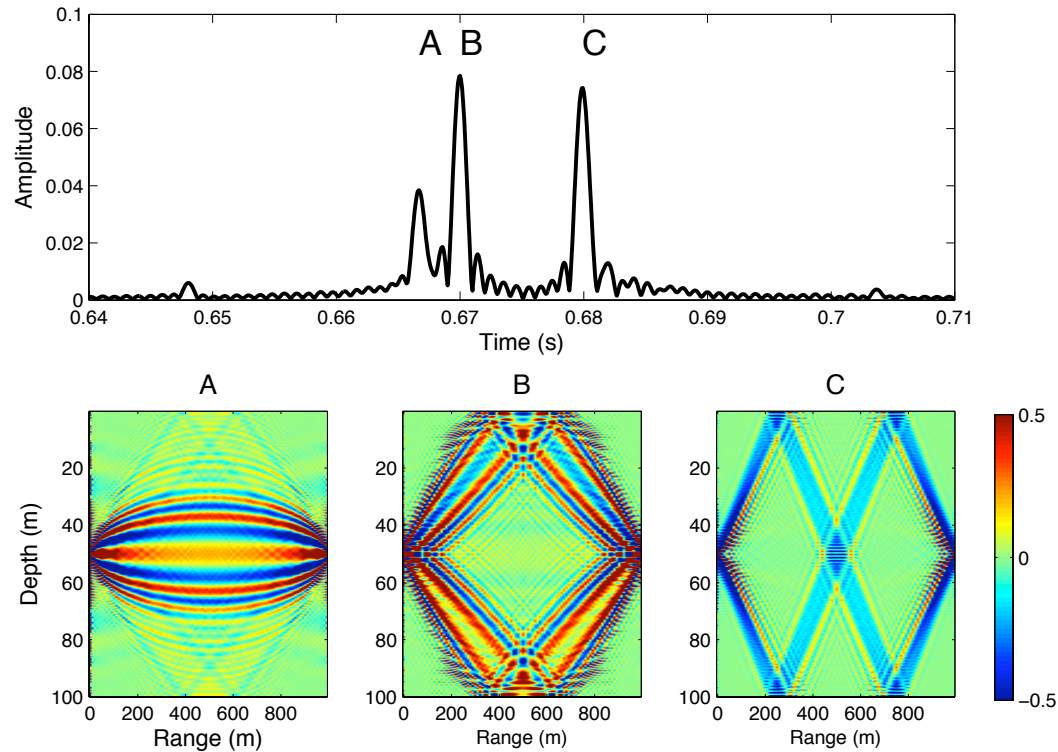
Figure 2.3: Time domain sensitivity kernels ($10^{-10}$ $\mu Pa$ $s$ $m^{-4}$) for one-way transmission, for a source at 50 m and receiver 1000 m away at a depth of 50 m. **Top:** Envelope of Green's function. A,B,C are the individual multipaths corresponding to direct path, single surface/bottom bounce, double bounce off the surface and bottom, **Bottom:** Time-domain sensitivity kernel for each arrival .
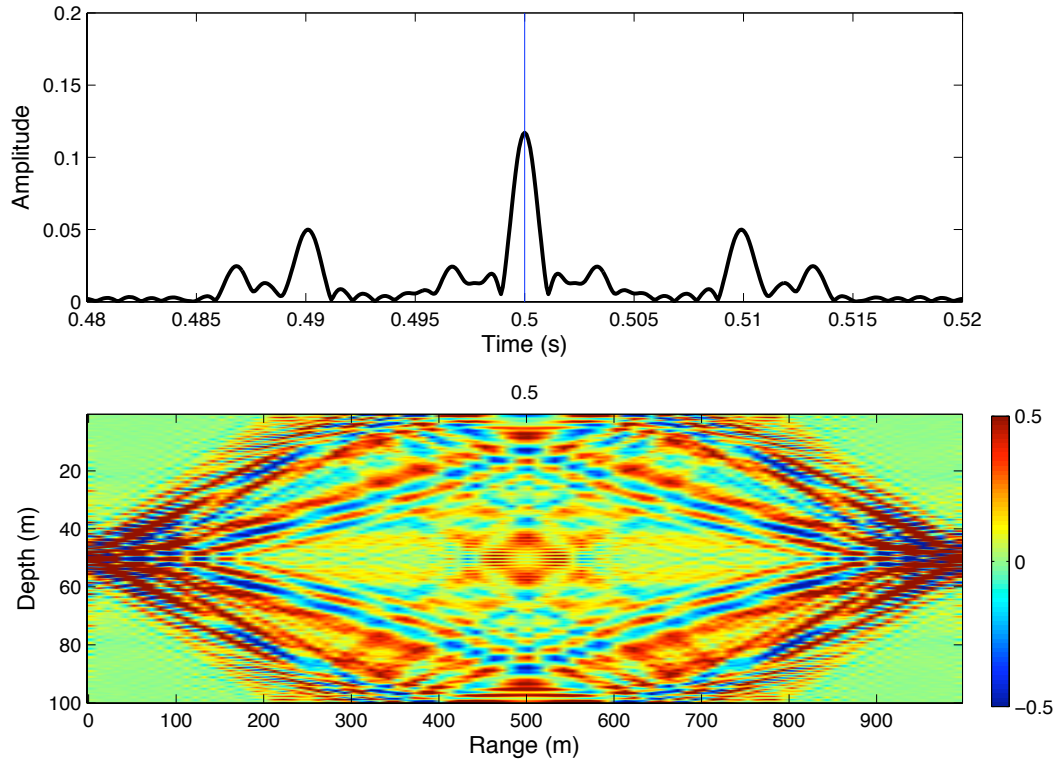
Figure 2.4: Time domain sensitivity kernels ($10^{-10}$ $\mu Pa$ $s$ $m^{-4}$) for the peak of a point-to-point time-reversal focal spot, for a source at 50 m and receiver 1000 m away at a depth of 50 m. **Top:** Pressure envelope of the focal spot, **Bottom** Time-domain sensitivity kernel for the focal spot, with the time of arrival in seconds.

Fig. 2.4 shows the time-domain sensitivity kernel for the time-reversal focal spot, obtained using the time-reversed Green's function in Fig. 2.3 as a source transmission. The time-reversed Green's function is normalized to have unit power. Time-reversal leads to the different multipath arrivals being phased in a way such that they all arrive at the same time, resulting in a focal spot. Similarly, time-reversal results in the sensitivity kernel for the focal spot being a phased sum of the sensitivity kernels for the peak of each arrival. Table 2.2 lists r.m.s sensitivities normalized by the r.m.s sensitivity of the direct path. The peak amplitude of the focal spot is different from the peak amplitude of the multipath arrivals. In order to compare the sensitivity of the focal spot versus that of the individual arrivals, the different sensitivity kernels are first divided by the peak pressure of the respective arrival.
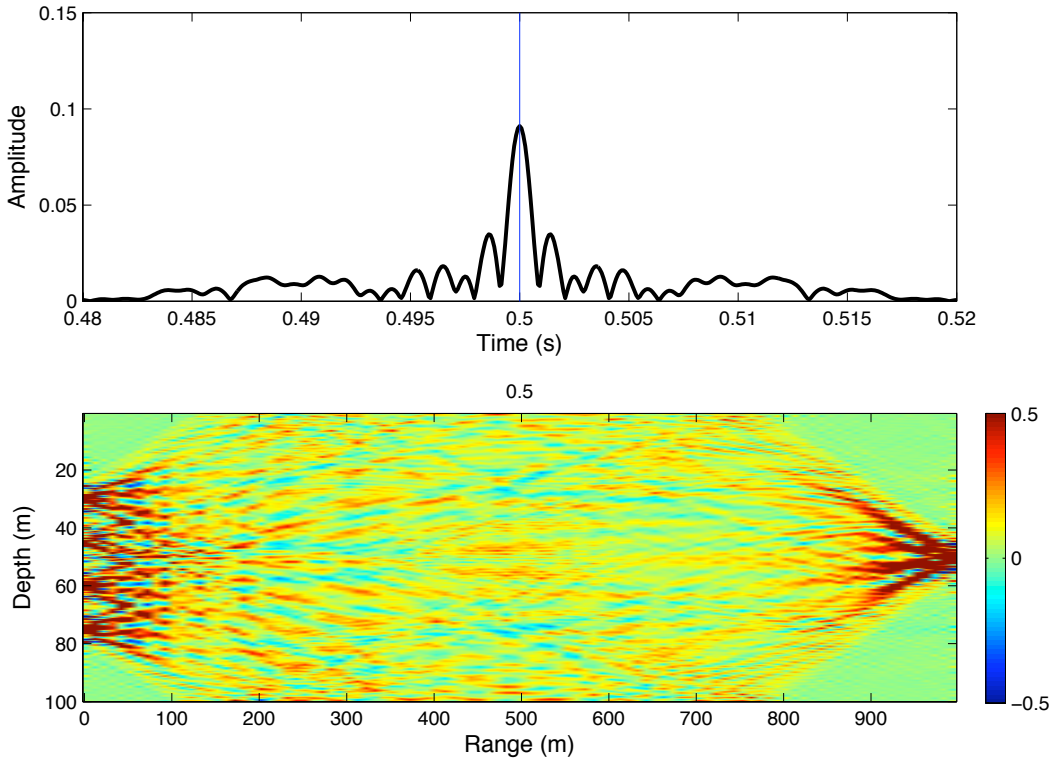
Figure 2.5: Time domain sensitivity kernels ($10^{-10}$ $\mu Pa$ $s$ $m^{-4}$) for the peak of the focal spot for a time-reversal mirror. There are 10 sources located between 30 m and 75 m and receiver 1000 m away at a depth of 50 m. **Top:** Pressure envelope of focal spot, **Bottom:** Time-domain sensitivity kernel for the focal spot, with the time-of-arrival in seconds.

Next, the use of an array (time-reversal mirror) is investigated, and the resulting sensitivity map is shown in Fig. 2.5. Ten sources are employed in the same configuration as shown in Fig. 2.1. The resulting sensitivity kernels are divided by the number of sources, in order to make a comparison with Figs. 2.3-2.4. It is seen that the sensitivity kernel for a time-reversal mirror is a superposition of sensitivity kernels corresponding to different sources, each of which transmits a time-reversed Green's function.

As seen in Table II, the use of a time-reversal mirror results in a reduction by 0.34 in sensitivity compared to a single-source time-reversed transmission (point-to-point time-reversal). This is caused by the averaging of the sensitivity kernels corresponding to the different sources in a manner similar to that of the free space

Table 2.2: The r.m.s sensitivities for one-way, time-reversal and a time-reversal mirror in a Pekeris waveguide, normalized to pressure sensitivity on the direct path.

| | One-way (point-to-point) | Time-reversal (point-to-point) | Time-reversal mirror (array-to-point) |
|---|---|---|---|
| Direct path | 1 | | |
| One bounce | 0.69 | 0.71 | 0.37 |
| Two bounces | 0.52 | | |

example in Sec. III, in addition to averaging over the multipath arrivals.

## 2.5  Source function optimization

As mentioned in Section II, expressing the array-to-point sensitivity kernel with the source transmissions as adjustable parameters allows for optimization of the source signal with regard to the sensitivity of the received signal to sound speed perturbations. Other constraints on the source signal can be added, resulting in a joint optimization problem. In this section, the optimization problem is posed in terms of obtaining a spatio-temporal (depth and time) focal spot, while at the same time minimizing the effect of fluctuations. The optimization is applied in the frequency domain since the pressure perturbations caused by sound speed fluctuations (eq. 2.7) is more simply expressed in the frequency domain. As a result of the optimization, the quality of the focal spot (mainlobe intensity, width, mainlobe to sidelobe ratio) may be traded off for increased stability.[5]

### 2.5.1  Minimizing pressure perturbations

In order to state the optimization problem in matrix form, the frequency domain, time domain and medium are discretized. To be conceptually simple, the medium is parameterized by a two-dimensional grid in range and depth. Thus, sound speed perturbations of the medium can be specified by the matrix $\Delta\mathbf{c}$, where the rows correspond to depth and columns to range. Similarly, the frequency-domain point-to-point sensitivity kernel (eq. 2.7) over the medium can be expressed

as a matrix $\mathbf{K}(\omega)$. Next, in order to express the integral in eq. 2.7 as the dot product of two vectors, the $N_z \times N_x$ two-dimensional matrices $\Delta\mathbf{c}$ and $\mathbf{K}(\omega)$ are written as $(N_z N_x) \times 1$ vectors after stacking the columns. Using the $vec\{\cdot\}$ notation to denote a vectorized (stacked columns) matrix, eq. 2.7 may be written as

$$\Delta P(x_r, z_r; \omega) = vec\{\mathbf{K}_{ap}(\omega)\}^T vec\{\Delta\mathbf{c}\}\Delta x \Delta z \qquad (2.18)$$

where the superscript $(\cdot)^T$ denotes matrix transpose. The area element (volume element for 3-D) $\Delta x \Delta z$ may be absorbed into $\Delta\mathbf{c}$ or $\mathbf{K}_{ap}(\omega)$ so the integral becomes a dot product. The two-dimensional $(N_z \times N_x)$ matrix $\mathbf{K}_{ap}$ is obtained by the multiplication of the three-dimensional $(N_z \times N_x \times N_s)$ matrix $\mathbf{M}_{pp}$ and the $N_s \times 1$ source vector $\mathbf{S}(\omega)$. The multiplication can also be presented in stacked form,

$$vec\{\mathbf{K}_{ap}(\omega)\} = vec\{\mathbf{M}_{pp}(\omega)\}\mathbf{S}(\omega) \qquad (2.19)$$

where $vec\{\mathbf{M}_{pp}(\omega)\}$ is the $(N_z N_x) \times N_s$ matrix obtained from stacking the first and second dimension of $\mathbf{M}_{pp}$. Eq. 2.19 will yield the $(N_z N_x) \times 1$ vector $vec\{\mathbf{K}_{ap}\}$ which expresses how the arrival at the receiver is sensitive to medium perturbations.

The received pressure perturbation (eq. 2.18) can now be expressed as

$$\Delta P(\omega) = \mathbf{S}(\omega)^T vec\{\mathbf{M}_{pp}(\omega)\}^T vec\{\Delta\mathbf{c}\} \qquad (2.20)$$

The portion of the optimization problem involving the minimization of the received pressure perturbation can now be conveniently stated in terms of a cost function component

$$
\begin{aligned}
J_1(\omega) &= <|\Delta P|^2> \\
&= \mathbf{S}(\omega)^H \; vec\{\mathbf{M}_{pp}(\omega)\}^H < vec\{\Delta\mathbf{c}\}vec\{\Delta\mathbf{c}\}^T > vec\{\mathbf{M}_{pp}(\omega)\} \; \mathbf{S}(\omega) \\
&= \mathbf{S}(\omega)^H \; vec\{\mathbf{M}_{pp}(\omega)\}^H \; \mathbf{C}_{dc} \; vec\{\mathbf{M}_{pp}(\omega)\} \; \mathbf{S}(\omega) \\
&= \mathbf{S}(\omega)^H \; \mathbf{C}_{mdc} \; \mathbf{S}(\omega) \qquad (2.21)
\end{aligned}
$$

where $\mathbf{C}_{dc}$ is the sound speed perturbation covariance matrix. The superscript $(\cdot)^H$ denotes matrix complex conjugate transpose (Hermitian). $\mathbf{C}_{mdc}$ is the $N_s \times N_s$ covariance matrix of the Born-approximation perturbed Green's functions at frequency $\omega$ between an array of sources and a single receiver. So element $ij$ of

$\mathbf{C}_{mdc}$ is the covariance between the pressure perturbation at the receiver from a transmission from source $i$ and the pressure perturbation at the receiver from a transmission from source $j$. $J_1$ is not minimized separately, but is done so as part of the joint optimization in order to avoid the trivial case of $S(\omega) = 0$.

The cost function component (eq. 2.21) does not take into account time and range shifts in the focal spot that may occur, caused for example, by internal wave induced sound speed fluctuations.[5] It also requires each realization of the focal spot to be stable, without addressing the ensemble average of focal spots, which was found to have a high stability.[6]

The cost function is computed independently for each frequency in the bandwidth of interest. This has been done in order to be consistent with the formulation of the inverse filter[18] which is more conveniently described on a single frequency basis. While the optimization can be done across all frequencies simultaneously, doing it on a frequency-by-frequency basis is a stronger constraint.

## 2.5.2   Obtaining a focal spot

The other part of the optimization is the choice of source function that will yield a focal spot. It was shown by Tanter et. al.[18] that while time-reversal only optimizes the pressure amplitude at the focus, the inverse filter adds constraints on the field around the focus, and is thus able to impose a desired sidelobe level or mainlobe width. Since this is a more general optimization problem, it is clearer to develop the optimized source function as a robust version of the inverse filter rather than as a robust version of time-reversal.

The ideal focal spot is defined as a delta function in depth and time at the range of the receiver,

$$u(t, z) = \delta(z - z_r)\delta(t - t_0) \tag{2.22}$$

In the frequency domain, $u(t, z)$ is written as the $N_p \times 1$ vector $\mathbf{U}(\omega)$, which is the desired focal spot, defined over $N_p$ depths. The problem now becomes one of choosing $\mathbf{S}(\omega)$ to produce a received pressure field at a set of $N_p$ depths that is as close to a delta function as possible, given a finite bandwidth. This may be stated

in the frequency domain as

$$\mathbf{U}(\omega) = \mathbf{G}(\omega)\mathbf{S}(\omega) + \Delta\mathbf{G}(\omega)\mathbf{S}(\omega) + \mathbf{r} \tag{2.23}$$

$\mathbf{G}$ is a $N_p \times N_s$ matrix of unperturbed Green's functions from each source to each of the $N_p$ depths at the range of the receiver. $\Delta\mathbf{G}$ is the (unknown) perturbation to the Green's function due to the perturbed sound speed field. In the absence of knowledge about $\Delta\mathbf{G}$, it is assumed that $\Delta\mathbf{GS}$ is a random variable, which can be included as part of the error term, $\mathbf{r}$. The misfit vector $\mathbf{r}$ is a $N_z \times 1$ random vector which is assumed to be jointly normally (Gaussian) distributed with prior joint probability density function (PDF) $\mathcal{N}(0, \mathbf{C_r})$. Eq. 2.23 then reduces to a linear model

$$\mathbf{U}(\omega) = \mathbf{G}(\omega)\mathbf{S}(\omega) + \mathbf{r} \tag{2.24}$$

While a full-depth representation is needed in eq. 2.24 in order to obtain a spatio-temporal focal spot, such a representation is not needed in the first cost function (eq. 2.21) where the emphasis is on minimizing received pressure sensitivity to fluctuations only at the receiver depth. Multiple receiver depths can be treated by adding terms to the cost function corresponding to other depths.

A Bayesian approach is now adopted to find the optimum estimator for $\mathbf{S}(\omega)$ that will satisfy eq. 2.24. The $N_s \times 1$ vector of source excitations $\mathbf{S}(\omega)$ is treated as an unknown random variable to be estimated. It is assumed to be jointly normally distributed with PDF $\mathcal{N}(0, \mathbf{C_S})$ . $\mathbf{C_S}$ expresses constraints on the size of $\mathbf{S}$ and the correlation between the signals from different sources. For example, assuming $\mathbf{C_S} = \beta\mathbf{I}$ means that the signals from different sources can be chosen independently, but the power of each source is constrained to be usually less than $2\beta$. Assuming $\mathbf{C_r} = \alpha\mathbf{I}$ means a uniformly distributed independent Gaussian misfit at each depth, with variance $\alpha$. This is a convenient assumption, but it may not be accurate, since the minimum width of the focal spot is determined by the multipaths available for focusing.

Solving eq. 2.24 is equivalent to minimizing the penalty function (where the penalty is the difference between the delta function and the focal spot at the receiver),

$$J_2 = \mathbf{r}^H \mathbf{C_r}^{-1} \mathbf{r} + \mathbf{S}^H \mathbf{C_S}^{-1} \mathbf{S} \tag{2.25}$$

$J_2$ may be recognized as the negative of log likelihood function for $\mathbf{S}$ given $\mathbf{U}$. The penalty function is affected by the number of depths at which the misfit vector is enforced, where a large number of closely spaced depths results in a larger penalty function. Minimizing $J_2$ with respect to $\mathbf{S}$ will give the maximum *a posteriori* estimator, which for the Gaussian-distributed case considered, is equivalent to the minimum mean square estimator,[29]

$$\hat{\mathbf{S}}(\omega) = (\mathbf{C_S}^{-1} + \mathbf{G}^H\mathbf{C_r}^{-1}\mathbf{G})^{-1}\mathbf{G}^H\mathbf{C_r}^{-1}\mathbf{U} \tag{2.26}$$

The above estimator, with $\mathbf{C_r} = \alpha\mathbf{I}$ and $\mathbf{C_S} = \beta\mathbf{I}$ gives a generalized inverse filter[10, 30] which does not require $\mathbf{G}$ to be full-rank,

$$\hat{\mathbf{S}}(\omega) = (\mathbf{G}^H\mathbf{G} + \frac{\alpha}{\beta}\mathbf{I})^{-1}\mathbf{G}^H\mathbf{U} \tag{2.27}$$

If the only concern is to obtain a temporal focal spot at a single depth (in which case $\mathbf{U}$, $\mathbf{r}$ and $\mathbf{GG}^H$ are scalars), it is simpler to solve eq. 2.26 in its equivalent form of,

$$\hat{\mathbf{S}}(\omega) = \mathbf{C_S}\mathbf{G}^H(\mathbf{G}\mathbf{C_S}\mathbf{G}^H + \mathbf{C_r})^{-1}\mathbf{U} \tag{2.28}$$

If $\mathbf{C_S} = \beta\mathbf{I}$, eq. 2.28 reduces to a scalar times $\mathbf{G}^H\mathbf{U}$ (phase conjugation). This shows that for purely temporal focusing, time-reversal and the inverse filter are the same.

## 2.5.3   Joint optimization

Adding the minimum sensitivity cost function in eq. 2.21 to the inverse filter cost function in eq. 2.25 gives

$$J_3 = \mathbf{S}^H\mathbf{C}_{mdc}\mathbf{S} + \mathbf{S}^H\mathbf{C_S}^{-1}\mathbf{S} + \mathbf{r}^H\mathbf{C_r}^{-1}\mathbf{r} \tag{2.29}$$

The source function that will minimize $J_3$ with respect to $\mathbf{S}$ has a form similar to eq. 2.26 except for the added sensitivity terms, and is given by,

$$\hat{\mathbf{S}}(\omega) = (\mathbf{C_S}^{-1} + \mathbf{C}_{mdc} + \mathbf{G}^H\mathbf{C_r}^{-1}\mathbf{G})^{-1}\mathbf{G}^H\mathbf{C_r}^{-1}\mathbf{U} \tag{2.30}$$

If $\mathbf{C_r} = \alpha\mathbf{I}$ and $\mathbf{C_S} = \beta\mathbf{I}$, then eq. 2.30 yields,

$$\hat{\mathbf{S}}(\omega) = (\frac{\alpha}{\beta}\mathbf{I} + \alpha\mathbf{C}_{mdc} + \mathbf{G}^H\mathbf{G})^{-1}\mathbf{G}^H\mathbf{U} \tag{2.31}$$

A few observations may be made regarding the optimized source function obtained in eq. 2.31. The ratio $\frac{\alpha}{\beta}$ is misfit to transmit power ratio. Setting $\alpha = 0$ (no error tolerated in the focal spot criterion) yields the inverse filter. Thus, eq. 2.31 is a modification of the generalized inverse filter, with a stability term ($\alpha \mathbf{C}_{mdc}$) that takes into account knowledge of the medium statistics and the sensitivity of the Green's function to sound speed perturbations ($\mathbf{C}_{mdc} = vec\{\mathbf{M}\}^T \ \mathbf{C}_{dc} \ vec\{\mathbf{M}\}$). In a medium with uncorrelated perturbations or extremely short scale inhomogeneities, pressure perturbations will tend to be uncorrelated between sources, so $\mathbf{C}_{mdc}$ will tend to be an identity matrix, and eq. 2.31 tends to the regularized inverse filter. Letting $\beta \to \infty$ (no constraint on transmit power) will yield an alternatively regularized inverse filter. Finally, setting $\alpha$ to large values will result in increased stability at the cost of degradation of the focal spot because $\alpha$ reflects the allowed difference between the observed focal spot and the desired delta-function like focal spot.

It is useful to look at the form of eq. 2.31 when only a temporal focus is desired (no focusing in depth). In such a case, $\mathbf{G}\mathbf{C_r}^{-1}\mathbf{G}^H$ is a scalar, and an equivalent form of eq. 2.31, similar to eq. 2.28, may be obtained by writing $\mathbf{P}^{-1} \equiv \frac{\alpha}{\beta}\mathbf{I} + \alpha\mathbf{C}_{mdc}$. The optimized source functions are then given by

$$
\begin{aligned}
\hat{\mathbf{S}}(\omega) &= \mathbf{P}\mathbf{G}^H(\mathbf{G}\mathbf{P}\mathbf{G}^H + \mathbf{C}_r)^{-1}\mathbf{U} \\
&= \lambda\mathbf{P}\mathbf{G}^H\mathbf{U}
\end{aligned}
\tag{2.32}
$$

It is thus seen that the optimized solution for purely temporal focusing reduces to the matrix $\mathbf{P}$ times the phase conjugated Green's function. If $\mathbf{P}$ is a scaled identity matrix, then this is again time-reversal.

As seen in eq. 2.31, the optimized source function requires rather complete knowledge of the medium in order to compute the sensitivity kernels, in addition to knowledge of statistics of sound speed perturbations. If these were available, then the optimized source function can be expected to perform better than time-reversal but it must be kept in mind that an attractive feature of time-reversal is that only the Green's function between source and receiver need be known.

## 2.6 Optimization applied to a Pekeris waveguide

Studies of the optimized source function with focusing in both time and depth are conducted for three scenarios involving different spatial structures of sound speed perturbations in a Pekeris waveguide. For each case, three transmission schemes are considered: time-reversal, the inverse filter (eq. 2.27), and optimized source function (eq. 2.31). The dimensions of the waveguide and number of sources are the same as in Sec. IV. Sound speed perturbations are assumed to be constant over a cell size of 10 m in range, 1 m in depth, and a long distance in the horizontal cross-range dimension. The sound speed perturbation in each cell is modeled as a Gaussian-distributed random variable. Changes in the perturbation variance with depth, and horizontal correlation scales of different lengths are introduced while comparing time-reversal with the optimized source shading function. In the first case, there is no correlation between perturbations in different cells. The second case involves a channel of zero variance in sound speed perturbations between source and receiver, while the third case has a long decorrelation scale in both range and depth for sound speed perturbations.

For the given medium, Green's functions were on the order of $10^{-4}$, resulting in sensitivities on the order of $10^{-8}$. In order to avoid plotting these extremely low values, the Green's functions were scaled up by $10^4$, resulting in sensitivities on the order of 1. The scaling used here is different from that in Sec. IV due to the fact that the sensitivity kernels in this section have been summed over $10\ m \times\ 1\ m$ cells in depth in order to deal with more manageable matrices.

Cost functions are calculated for the various perturbation scenarios, where the cost function for sensitivity, $J_1(\omega)$ is computed using eq. 2.21, and the cost function for the sharpness of the focal spot, $J_2(\omega)$, is computed according to eq. 2.25, with the ideal focal spot specified at 11 equally spaced depths from $25\ m$ to $75\ m$. Recognizing that the inverse filter produces the best achievable focal spot for a given medium, the ideal focal spot ($\mathbf{U}(\omega)$ in eq. 2.24) is chosen such that the focal spot cost function $J_2^{IF}(\omega) = 0$ for the unregularized inverse filter. The value of $\alpha$ is now chosen such that the focal spot cost function for time-reversal $J_2^{TR}(\omega) = 1$, for all frequencies. A value of 1 is chosen for the convenience of plotting, and can

be set to a different value in a practical problem. Next, $\beta$ can be varied to yield a focal spot cost function that varies between 0 and 1, depending on the amount of tradeoff desired between quality of focal spot and sensitivity to medium perturbations. For all case studies in this section, $\beta = 50$. The values of $\alpha$ and $\beta$ will depend on the specific scaling used for the Green's function.

Sensitivity kernels and source shading functions will be the same for time-reversal and the inverse filter for all three cases since they are ignorant of the presence or absence of structure in the sound speed perturbations. As a result, source shading functions and sensitivity kernels for time-reversal and the inverse filter are only shown for the first case where there is no structure in sound speed perturbations. The received signals for time-reversal and the inverse filter are also the same for different cases and hence are only shown for the first case. Finally, as seen in Table III, since the focal spot cost function is very similar for the inverse filter and the optimized source function, this is also not shown for the last two case studies. Sensitivity cost functions for the three transmission schemes (time-reversal, inverse filter and optimized source function), however, will be different for each case considered due to differences in the $\mathbf{C}_{mdc}$ term for each case (eq. 2.21). The range of values for the sensitivity cost function depends on the specific Green's functions considered and the statistics of the medium. The value of the sensitivity cost function also depends on the number of points (and spacing) at which the sensitivity kernel is evaluated.

The performance of time-reversal, the inverse filter (eq. 2.27) and the optimized source function under various sound speed perturbation scenarios are summarized in Table 2.3. The use of an inverse filter imposes explicit constraints on sidelobe levels in both time and depth.[18] Since the optimized solution is similar to the inverse filter, in the absence of noise, the focal spot obtained will have lower sidelobe levels, and hence, a smaller focal spot cost function (eq. 2.25) than time-reversal. The peak-to-sidelobe ratios for the inverse filter and optimized source function is about 2 dB greater than that of time-reversal. The focal spot cost function (Table III) for the inverse filter and the optimized source function is always about 90% less than that of time-reversal. However, although all three source

functions are normalized to have the same source power, time-reversal has a higher peak received power. This is because time-reversal is a matched filter, which is the optimal solution for maximizing received power, without other constraints.
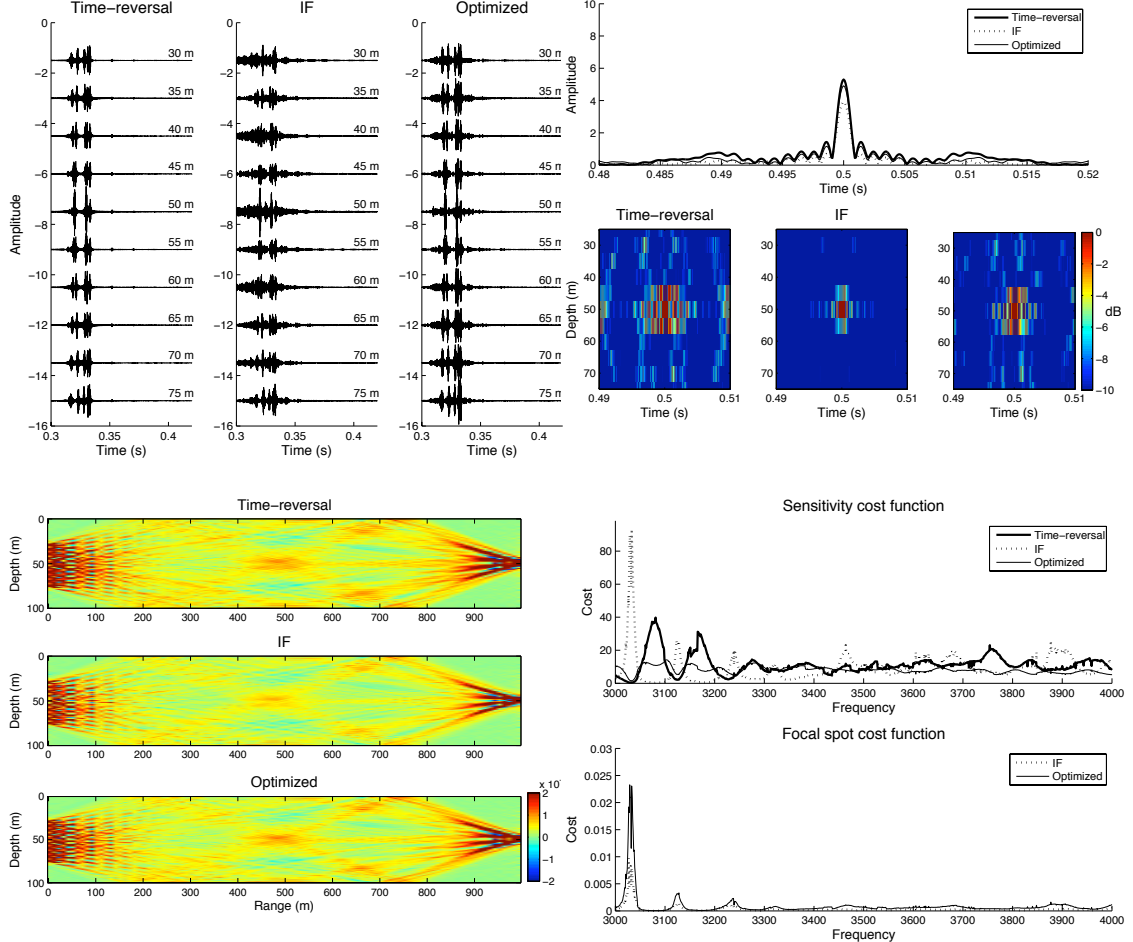


Figure 2.6: Performance of time-reversal, the inverse filter and the optimized source function. Sound speed perturbations are homogeneous, isotropic and uncorrelated on a 10m x 1m scale. **Top left:** Transmit signals across depth, **Top right:** Received signals, in time and depth, at the focal spot, **Bottom left:** Pressure sensitivity kernels ($10^{-4}$ $\mu Pa$ $s$ $m^{-4}$) for time-reversal, the inverse filter and the optimized source function, **Bottom right:** Cost functions. The focal spot cost function for time-reversal is fixed to be a constant value of 1.

Fig. 2.6 shows the results of the numerical simulation involving the first scenario where the sound speed perturbations have the same variance and are uncorrelated between grid points in both dimensions. The top panels of Fig. 2.6 show the transmit and receive signals for time-reversal and the optimized source

shading functions. The bottom left panel shows the sensitivity kernels for each scheme while the bottom right panel shows the cost function metrics over a 1 $kHz$ bandwidth for time-reversal and the optimized source function. The focal spot cost function for time-reversal is fixed to be 1, and is not shown in order to show more clearly the cost functions for the inverse filter and the optimized source function which are on the order of 0.01. The lack of structure in the sound speed perturbation results in only a 2.5% difference in sensitivity between the inverse filter and time-reversal (Table III). However, despite the lack of structure, the sensitivity cost function for the optimized source function is about 35% less than that of time-reversal, while the focal spot cost function for both the inverse filter and optimized source function is about 90% less than that of time-reversal.
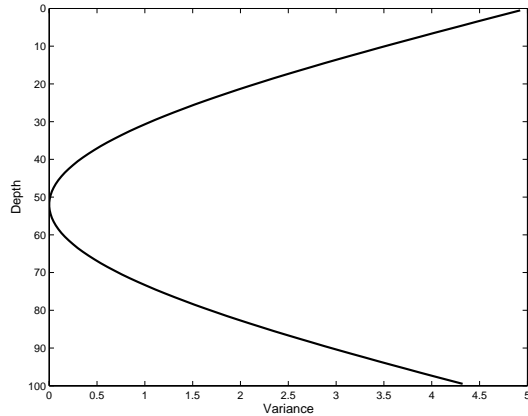


Figure 2.7: Shape of depth-dependent variance of sound speed perturbations. The sound speed perturbations obtained were used to obtain Fig. 2.8.

Next, structure in the sound speed perturbations is introduced by means of a region where the variance of the sound speed perturbations drops to zero. The depth of zero variance is placed at a constant depth of 52 $m$. The shape of the depth-dependent variance is shown in Fig. 2.7. The sound speed perturbations, however, are still uncorrelated between cells. The ratio of transmit power for the source at 50 $m$ to the average power at other depths for the optimized scheme is about 100% higher than that for time-reversal, indicating a concentration of power in the unperturbed region. For this case, the inverse filter is 26% more sensitive to sound speed perturbations than time-reversal, while the optimized source function
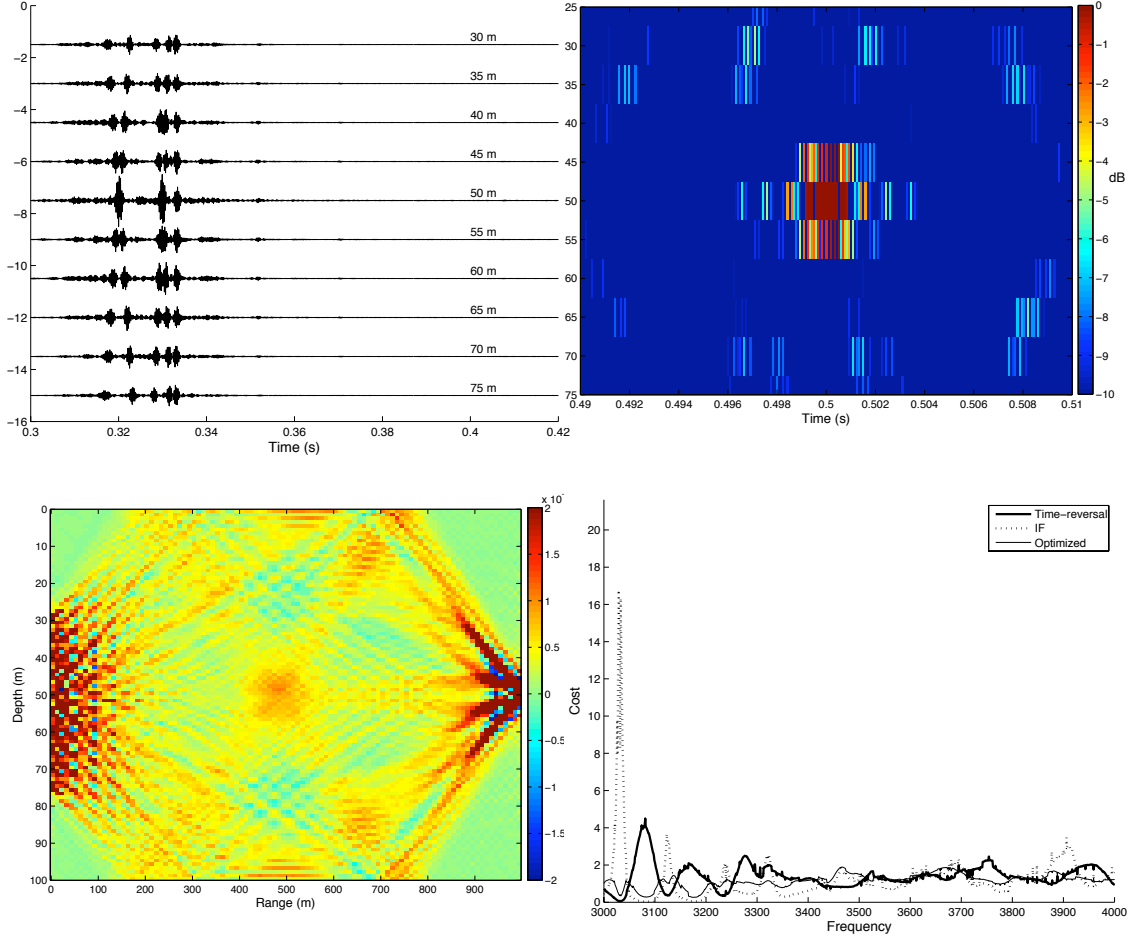
Figure 2.8: Performance of time-reversal, the inverse filter and the optimized source function. Sound speed perturbations are homogeneous, isotropic and uncorrelated on a 10m x 1m scale. The variance of sound speed perturbations reduces to zero at 52 m as shown in Fig. 2.7. The source shading function and sensitivity kernel for time-reversal and the inverse filter are identical to those in Fig. 2.6, and have been omitted. **Top left:** Optimized transmit signals across depth, **Top right:** Received signal in time and depth, near the focal spot, for the optimized source function, **Bottom left:** Optimized pressure sensitivity kernel ($10^{-4}$ $\mu Pa$ $s$ $m^{-4}$), **Bottom right:** Sensitivity cost function. The focal spot cost function is almost identical to the case in Fig. 2.6.

is about 20% less sensitive compared to time-reversal. The focal spot cost functions are similar to the previous case.
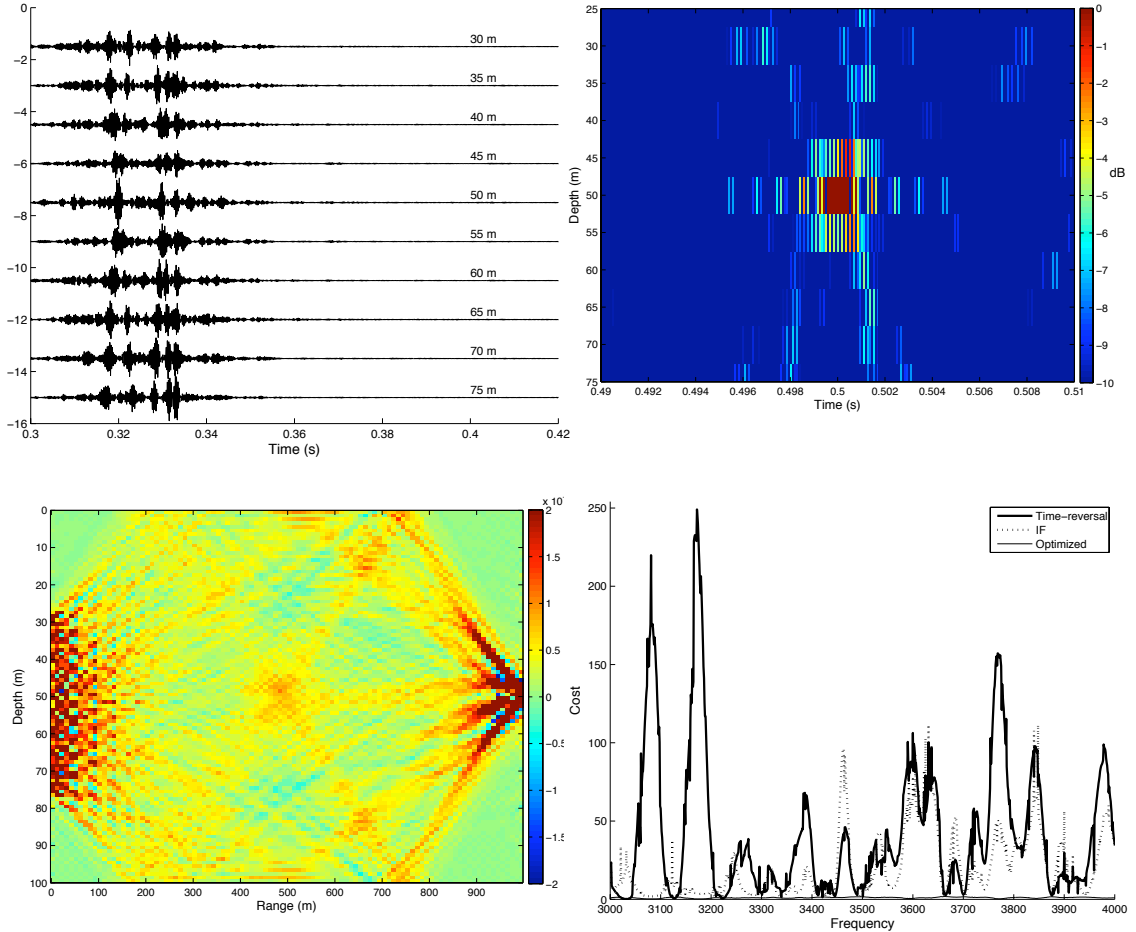
Figure 2.9: Performance of time-reversal, the inverse filter and the optimized source function. Sound speed perturbations have a long decorrelation scale in range (100 m) and depth (100 m). The source shading function and sensitivity kernel for time-reversal and the inverse filter are identical to those in Fig. 2.6, and have been omitted. **Top left:** Optimized transmit signals across depth, **Top right:** Received signal, in time and depth, near the focal spot, for the optimized source function, **Bottom left:** Optimized pressure sensitivity kernels ($10^{-4} \ \mu Pa \ s \ m^{-4}$), **Bottom right:** Sensitivity cost function. The focal spot cost function is almost identical to the case in Fig. 2.6.

The third study (Fig. 2.9) involves the use of a long (100 $m$ in range, 100 $m$ in depth) spatial decorrelation scale for the sound speed perturbations. The correlation decays exponentially over 100 $m$ in range and 100 $m$ in depth. The perturbations are still isotropic and homogeneous. This is meant to represent low-mode internal waves in the ocean. The optimized source function shows significantly lower sensitivity, with a 98 % reduction (Table 2.3) compared to time-reversal, while the inverse filter shows a 52% reduction with respect to time-reversal. At the same time, the quality of the focal spot is similar to that of the inverse filter in terms of peak-to-sidelobe ratio, although the peak amplitude has been reduced. Thus, the presence of structure allows the optimized source function to exploit the knowledge of sound speed perturbations to produce a focal spot that is very similar to that of the inverse filter, but at the same time considerably less sensitive to sound speed perturbations than time-reversal (Table III).

## 2.7 Conclusions

A pressure sensitivity kernel was developed for the case where an array of sources transmits to a single receiver. This kernel is extendable to multiple-input multiple-output scenarios. The Born-approximated sensitivity kernel for the received pressure was used to provide an explanation for why time-reversal and the inverse filter are more stable compared to a one-way transmission. In the absence of multipath, the sensitivity of a time-reversed transmission for a single source-receiver pair was shown to be identical to a one-way transmission. A reduction in pressure sensitivity is only obtained through the use of a time-reversal mirror which results in the coherent addition of the kernels from different sources as opposed to an incoherent addition in the case of a broadside transmission. Time-reversal allows for the coherent addition of the kernels corresponding to different paths arriving at the same time. The presence of multipath has an effect similar to a time-reversal mirror, with a lowering of sensitivity resulting from the superposition of the multipath kernels.

The linear (first Born) approximation is only valid when sound speed perturbations are very small compared to the background sound speed. Ongoing simulations, beyond the scope of this paper, show that the Born approximation for a 1 $km$ by 100 $m$ waveguide is valid for sound speed perturbations up to about 0.2 $m$/s, for a background sound speed of 1500 $m/s$. If only the envelope of the Green's function is of interest, the range of validity is extended until about 5 $m/s$. This is within the range of most internal wave induced sound speed fluctuations in the ocean. Further, as a result of the volume integral expression for the perturbed Green's function, the effect of longer path lengths is to lower the range of sound speed perturbations for which the linear approximation is valid.

The pressure sensitivity kernel was used to obtain an optimized source shading function that can be considered an environmentally adaptive version of time-reversal and the inverse filter. While this optimized source function was almost identical to the inverse filter when there is no structure in the sound speed perturbation field, the gains are significant in the presence of structure, such as a depth of zero variance, or a long decorrelation length in the sound speed perturbations.

Table 2.3: Peak-to-sidelobe ratio (PSR), sensitivity cost function ($J_1$), and focal spot cost function ($J_2$) for time-reversal (TR), inverse filter (IF), and the optimized source function (opt.). Cost functions are % reduction with respect to time-reversal, averaged over 1 kHz. 'No structure' corresponds to uncorrelated random Gaussian sound speed perturbations. 'Channel' denotes a channel of zero variance in sound speed perturbations at a constant depth of 52 $m$. 'Structure' denotes a long depth and range decorrelation scale for sound speed perturbations.

| | PSR (dB) | | | $J_1$ | | $J_2$ | |
|---|---|---|---|---|---|---|---|
| | TR | IF | opt. | IF | opt. | IF | opt. |
| No structure | 31.17 | 32.95 | 32.14 | $-2.5\%$ | 34.15% | 99.9% | 99.8% |
| Channel | 31.17 | 32.95 | 33.33 | $-26.58\%$ | 19.9% | 99.9% | 99.8% |
| Structure | 31.17 | 32.95 | 32.77 | 52.73% | 98.2% | 99.9% | 99.8% |

## 2.8  Acknowledgment

The text in this chapter is in full a reprint of the material as it appears in Kaustubha Raghukumar, Bruce Cornuelle, William Hodgkiss, William Kuperman, "Pressure sensitivity kernels applied to time-reversal acoustics", J. Acoustic Soc. Am., Vol. 124, Issue 1, pp. 98-112, 2008.

# Bibliography

[1] M. Fink, D. Cassereau, A. Derode, C. Prada, P. Roux, M. Tanter, J. L. Thomas, and F. Wu. Time-reversed acoustics. *Rep. Prog. Phys.*, 63:1933–1965, 2000.

[2] G. F. Edelmann, T. Akal, W. S. Hodgkiss, S. Kim, W. A. Kuperman, and H. C. Song. An initial demonstration of underwater acoustic communication using time-reversal. *IEEE J. Oceanic Engineering*, 27:602–608, 2002.

[3] H. Nguyen, J. Andersen, and G. Pederson. The potential use of time-reversal techniques in multiple element antenna systems. *IEEE commun. Lett.*, 9:40–42, 2005.

[4] W. S. Hodgkiss, H. C. Song, W. A. Kuperman, T. Akal, C. Ferla, and D. R. Jackson. A long-range and variable focus phase-conjugation experiment in shallow water. *J. Acoustic Soc. Am.*, 105:1597–1604, 1999.

[5] S. Kim, W. A. Kuperman, W. S. Hodgkiss, H. C. Song, and G. F. Edelmann. Robust time-reversal focusing in the ocean. *J. Acoustic Soc. Am.*, 114:145–157, 2001.

[6] D. R. Dowling and D. R. Jackson. Narrow-band performance of phase-conjugate arrays in dynamic random media. *J. Acoustic Soc. Am.*, 91:3257–3277, 1992.

[7] G. Papanicolaou, L. Rhyzhik, and K. Solna. Statistical stability in time reversal. *SIAM J. Appl. Math*, 64:1133–1155, 2004.

[8] G. Montaldo, G. Lerosey, A. Derode, A. Tourin, J. Rosny, and M. Fink. Telecommunication in a disordered environment with iterative time reversal. *Waves in Random Media*, 14:287–302, 2004.

[9] M. Stojanovic. Retrofocussing techniques for high rate acoustic communications. *J. Acoustic Soc. Am.*, 117:1173–1185, 2005.

[10] M. Tanter, J.-F. Aubry, J. Gerber, J.-L. Thomas, and M. Fink. Optimal focussing by spatio-temporal inverse filter. I. Basic principles. *J. Acoustic Soc. Am.*, 110:37–47, 2001.

[11] H. Marquering, G. Nolet, and F. A. Dahlen. Three-dimensional waveform sensitivity kernels. *Geophs. J. Int.*, 132:521–534, 1998.

[12] F. A. Dahlen, S. H. Hung, and Guust Nolet. Frechét kernels for finite-frequency traveltimes-I. Theory. *Geophs. J. Int.*, 141:157–174, 2000.

[13] F. A. Dahlen, S. H. Hung, and Guust Nolet. Frechét kernels for finite-frequency traveltimes-II. Examples. *Geophs. J. Int.*, 141:175–1203, 2000.

[14] E. K. Skarsoulis and B. D. Cornuelle. Travel-time sensitivity kernels in ocean acoustic tomography. *J. Acoustic Soc. Am.*, 116:227–238, 2004.

[15] B. Sarkar, B. Cornuelle, and W. A. Kuperman. Estimating sound-speed perturbations with full-wave environmental sensitivity kernels. *J. Acoustic Soc. Am.*, 119:3246, 2006.

[16] P. Hursky, M. B. Porter, B. D. Cornuelle, W. S. Hodgkiss, and W. A. Kuperman. Adjoint modelling for acoustic inversion. *J. Acoustic Soc. Am.*, 115:607–619, 2004.

[17] P. Roux and M. Fink. Time reversal in a waveguide: Study of the temporal and spatial focussing. *J. Acoustic Soc. Am.*, 107:2418–2429, 2000.

[18] M. Tanter, J. L. Thomas, and M. Fink. Time-reversal and the inverse filter. *J. Acoustic Soc. Am.*, 108:223–234, 2000.

[19] M. Born. Quantum mechanics of impact processes. *Z. Phys.*, 38:803–827, 1926.

[20] J. R. Taylor. *Scattering Theory.* Wiley, New York, 1972.

[21] E. K. Skarsoulis, G. A. Athanassoulis, and U. Send. Ocean acoustic tomography based on peak arrivals. *J. Acoustic Soc. Am.*, 100:797–813, 1996.

[22] T. Chen, P. Ratilal, and N. C. Makris. Mean and variance of the forward field propagated through three-dimensional random internal waves in a continental-shelf waveguide. *J. Acoustic Soc. Am.*, 118:3560–3574, 2005.

[23] C. Garret and W. Munk. Space-time scales of internal waves. *Geophysical Fluid Dynamics*, 2:225–264, 1972.

[24] M. Bruhl, G. J. O. Vermeer, and M. Kiehn. Fresnel zones for broadband data. *Geophysics*, 61:600–604, 1996.

[25] J. Pearce and D. Mittleman. Defining the fresnel zone for broadband radiation. *Physical Review E*, 66:056602/1–4, 2002.

[26] B. Cornuelle, M. Dzieciuch, and E. Skarsoulis. Wave-theoretic kernels for long-range ocean travel-time measurement. *J. Acoustic Soc. Am.*, 119:3248, 2006.

[27] W. A. Kuperman, W. S. Hodgkiss, H. C. Song, T. Akal, C. Ferla, and D. R. Jackson. Phase conjugation in the ocean: Experimental demonstration of an acoustic time-reversal mirror. *J. Acoustic Soc. Am.*, 103:25–40, 1998.

[28] F. B. Jensen, W. A. Kuperman, and M. B. Porter aand H. Schmidt. *Computational Ocean Acoustics*. American Institute of Physics, Woodbury, NY, 1994.

[29] S. M. Kay. *Fundamentals of statistical signal processing - Estimation theory.* Prentice Hall, New Jersey, 1993, Ch. 10.

[30] W. J. Higley, P. Roux, and W. A. Kuperman. Relationship between time-reversal and linear equalization in digital communications. *J. Acoustic Soc. Am.*, 120:35–37, 2006.

# Chapter 3

# Experimental Demonstration of Pressure Sensitivity Kernels

Pressure sensitivity kernels were recently applied to time-reversal acoustics in an attempt to explain the enhanced stability of the time-reversal focal spot [Raghukumar *et al.*, J. Acoust. Soc. Am. **124**, 98-112 (2008)]. The theoretical framework developed was also used to derive optimized source functions, closely related to the inverse filter. The use of these optimized source functions results in an inverse filter-like focal spot which is more robust to medium sound speed fluctuations than both time-reversal and the inverse filter. The theory is now applied to experimental data gathered during the Focussed Acoustic Fields experiment, conducted in 2005, north of Elba Island in Italy. Sensitivity kernels are calculated using a range-independent sound-speed profile, for a geometry identical to that used in the experiment, and path sensitivities are identified to observed arrivals. The validity of the kernels in tracking time-evolving Green's functions is studied, along with limitations as a result of their linearized nature. An internal wave model is used to generate an ensemble of sound speed profiles, which are then used along with the calculated sensitivity kernels to derive optimized source functions. Focal spots obtained using the observed Green's functions with these optimized source functions are then compared to those obtained using time-reversal and the inverse-filter. It is shown that these functions are able to provide a focal spot superior to time-reversal while being more robust to sound speed fluctuations than

the inverse filter or time-reversal.

## 3.1 Introduction

The ability to focus sound in a waveguide has been found to be useful in a variety of applications such as underwater communications, target detection, medical ultrasonics and non-destructive testing of materials.[1, 2, 3] Time-reversal has been the tool of choice in these applications due its simplicity and robustness to environmental perturbations. The time-reversal operation consists of first acquiring the Green's functions between an array of sources and a receiver at whose location the sound is to be focused. This set of acquired Green's functions, when time-reversed and retransmitted, produces a focal spot at the receive location. Focusing is often observed even after the Green's functions have changed during the time that has elapsed between acquisition and retransmission.

While the focal spot has been shown to persist several minutes to days after the initial acquisition of the Green's function,[4, 5] there is a measurable degradation in quality which eventually makes the re-acquisition of the Green's function necessary. In addition, the focal spot produced by time-reversal maximizes the energy at the focal spot without constraints on sidelobes in depth, range and time. The inverse filter has been suggested as an alternative to time-reversal which can produce a sharper focal spot,[6, 7, 8] at the cost of knowledge required to obtain additional Green's functions in depth, and a reduced amplitude of the focal spot. However, the stability of the focal spot with respect to environmental fluctuations is still not constrained. In order to achieve enhanced stability of the focal spot, Kim et. al.[5] proposed a modification of narrowband time-reversal which makes the focus more stable, but with considerable broadening of the focal spot. This paper demonstrates the practical use of optimized source functions which are able to produce a sharp inverse filter-like focal spot, while at the same time being robust to environmental fluctuations, via a sensitivity kernel-based regularization term included in the inverse filter formulation.

Sensitivity kernels were originally proposed in seismology as wave-theoretic

tomography tools as opposed to the more commonly used ray-theoretic time-of-arrival tomography. [9, 10, 11] In the ocean waveguide, travel-time sensitivity kernels[12] were shown to have the same properties as those developed in seismology, and were used to invert for sound speed perturbations in deep water. Pressure sensitivity kernels are currently being employed as a means of doing sound speed inversions in shallow water.[13]

Recently, pressure sensitivity kernels were used a means of explaining the remarkable stability of the time-reversal focus.[14] It was shown that the time-reversal operation, which causes the various multipath arrivals in a waveguide to arrive at the same time, also results in the pressure sensitivity kernel for each arrival to overlap with the kernels for other arrivals, resulting in a net reduction in sensitivity for time-reversal compared to a one-way transmission. An offshoot of this work was the formulation of optimized source functions using pressure sensitivity kernels that were based on the inverse filter. This paper demonstrates the use of these optimized source functions using experimental acoustic and environmental data gathered during the Focussed Acoustic Fields 2005 (FAF05) experiment, conducted off of Elba Island, Italy in July 2005. The focal spot obtained using these source functions is seen to have a peak-to-sidelobe level in between that of time-reversal and the inverse-filter, but a greater stability to environmental perturbations than both schemes. The use of optimized source functions requires knowledge of the covariance matrix for sound speed perturbations and sensitivity kernels. This scheme, therefore, should be viewed as being synergistic with a shallow-water observation program, which requires similar knowledge.

This paper is organized as follows. Sec. II briefly describes the Focused Acoustic Fields experiment. More comprehensive details may be found in the paper by Song et. al.[15] Acoustic data from this experiment is used to compare the time-reversal focal spot with that obtained by the optimized source functions. The propagation model used to compute sensitivity kernels is also validated against acoustic data. Environmental data gathered during the experiment is used to validate the internal wave model, which in turn is used to generate range-dependent sound speed profiles. Sec. III presents a review of pressure sensitivity kernels

previously derived[14], and explores the limits of the linear assumption used to derive the kernels. The ability of the sensitivity kernels to track a time-evolving Green's function is shown for time-scales on the order of a few minutes, after which the linear assumption no longer holds. Sec. IV discusses the optimized source functions and compares the focal spot properties with experimental time-reversal data. It is shown that focal spot quality can be traded off for robustness to environmental fluctuations, and that the optimized source functions can obtain an inverse filter-like focal spot, while being robust to sound speed perturbations. Finally, Sec. V concludes the chapter followed by an appendix which provides details on the internal wave model used.

## 3.2   Experiment overview

The FAF05 experiment was conducted north of Elba Island off the west coast of Italy in July 2005.[16, 4, 15] The experiment layout is shown in Fig. 3.1. Acoustic transmissions were made using a 29-element Source Receive Array (SRA), and received over a 32-element Vertical Receive Array (VRA). The SRA spanned water depths 34 m to 112 m, with an array element spacing of 2.786 m, while the VRA spanned water depths 48 m to 110 m, with an array element spacing of 2 m. The water depth in the vicinity of the experiment was 121 m, and the arrays were 4.071 km apart in range. As seen in Fig. 3.1, various environmental measurements were made during the course of the experiment, such as surface waves using a waverider buoy (WR), temperature profiles using two thermistor chains (TC's), and current measurements using an acoustic doppler current meter (ADCP). The thermistor chains had 11 elements each and spanned water depths 18.5 m to 76.5 m, with a sampling period of 10 minutes. In addition, conductivity-temperature-depth (CTD) measurements were made approximately every 30 minutes. In this paper, only the CTD and TC data are analyzed.

Round-robin pseudo-pulse transmissions were made every 20 seconds over a period of 9 hours on 2005, Day 197. These transmissions, meant to measure Green's functions between the source and receive arrays, consisted of 1-second chirps with

a bandwidth of 1.4 kHz, and a center frequency of 3.5 kHz. The received signals on the VRA were then match-filtered to yield Green's function estimates.
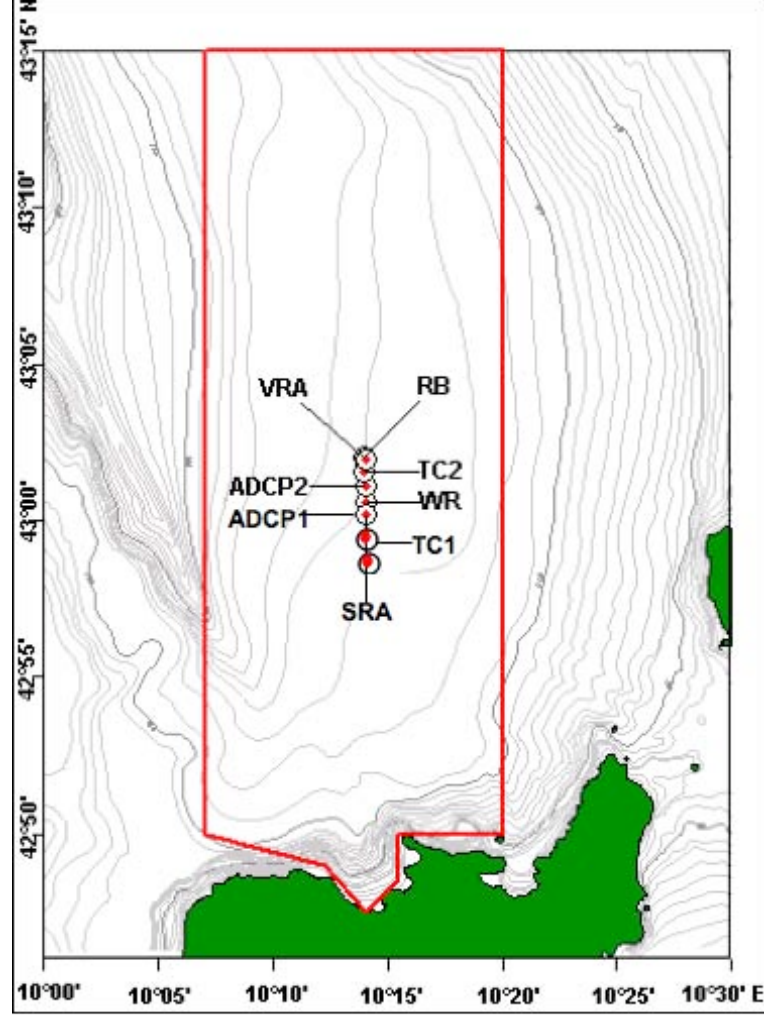


Figure 3.1: Locations of various moorings during the FAF05 experiment. In green at the bottom is Elba Island.

Fig. 3.2 shows the temperature, salinity and sound speed profiles obtained from a CTD cast that was made at the beginning of the transmissions, close to the VRA. The sound speed profile is downward refracting, with the thermocline located around 30 m. Temperature measurements made by the thermistor chains at the same time are also plotted. While there is a close agreement with between the CTD and the nearby TC2, the TC1 measurement is a little different, show-

ing range dependence. Fig. 3.3 shows the temperature fluctuations measured on thermistor chain TC2 during the FAF experiment. Temperature fluctuations are plotted as filtered above and below the inertial frequency. Fluctuations above the inertial frequency are shown over a period of 24 hours, while sub-inertial frequency fluctuations are shown over 12 days. It appears that there is some internal wave activity between the 30-40 m depth, with decreasing activity towards the surface and bottom. Also included are the r.m.s plots for the high- and low-pass filtered temperature chain data. The shorter time scale of the high-pass filtered data allows for a closer look at the internal wave energy structure around the thermocline. The r.m.s of the temperature data is used to constrain the energy parameter of the internal wave model in Sec. III.
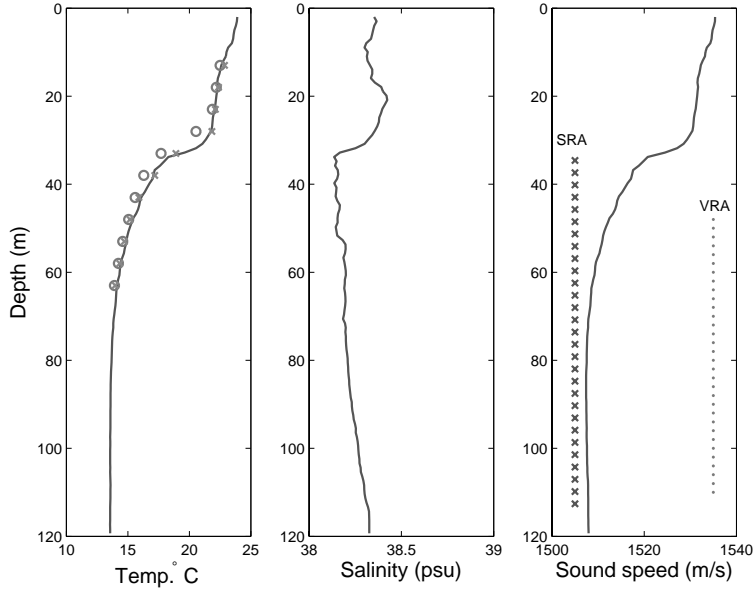


Figure 3.2: Temperature, salinity and sound speed profile. Crosses on temperature plot denote measurements made by thermistor chain TC2, and circles denote measurements made by thermistor chain TC1, at the same time. Crosses and dots on the sound speed plot denote and SRA and VRA hydrophone depths.

Fig. 3.4 shows the evolution, over 10 minutes, of two observed Green's function estimates. The first is between a source at 112.6 m and receiver at 110 m, located close to the bottom, while the second is between a source at 112.6 m, near the bottom and a receiver at 48 m, near the surface. While both Green's functions
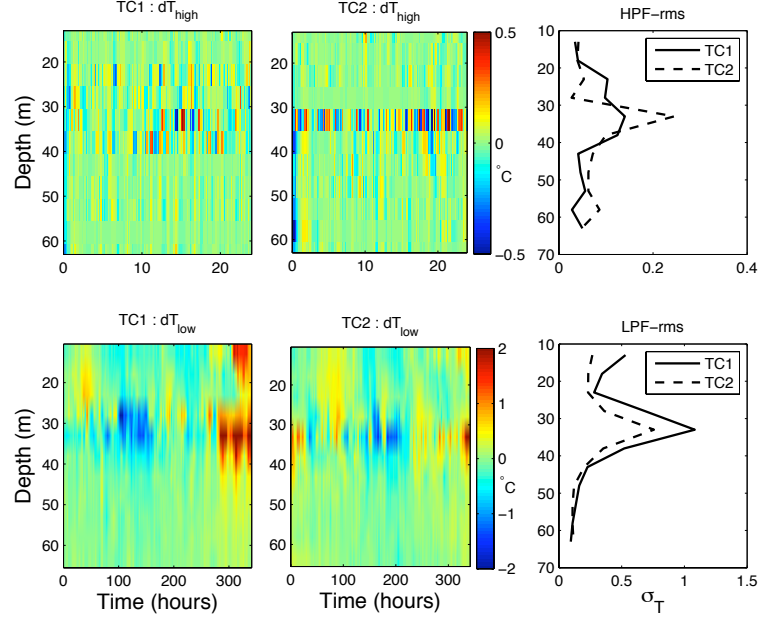
Figure 3.3: Temperature anomalies (with respect to mean) derived from thermistor chains TC1 (blue solid)and TC2 (green dashed). The upper panel shows fluctuations above the inertial frequency over 1 day while the lower panel shows sub-inertial frequency temperature fluctuations over two weeks. Also included are the r.m.s plots for the high- and low-pass filtered temperature chain data.

appear to be relatively stable, the right panel shows more dynamic variation over the 10 minute interval, due to its location in a region of internal-wave induced sound speed fluctuations.

## 3.3    Environmental modeling

In order to compute the optimized source functions, it is necessary to calculate pressure sensitivity kernels and estimate the covariance matrix for sound speed perturbations. Using the Born approximations, sensitivity kernels can be derived from the Green's functions between the source and points in the medium, and between the same points and the receiver.[14] Experimental data typically only have available the source-receiver Green's functions. Green's functions are hence computed via computer simulations and tested by comparison with those that were
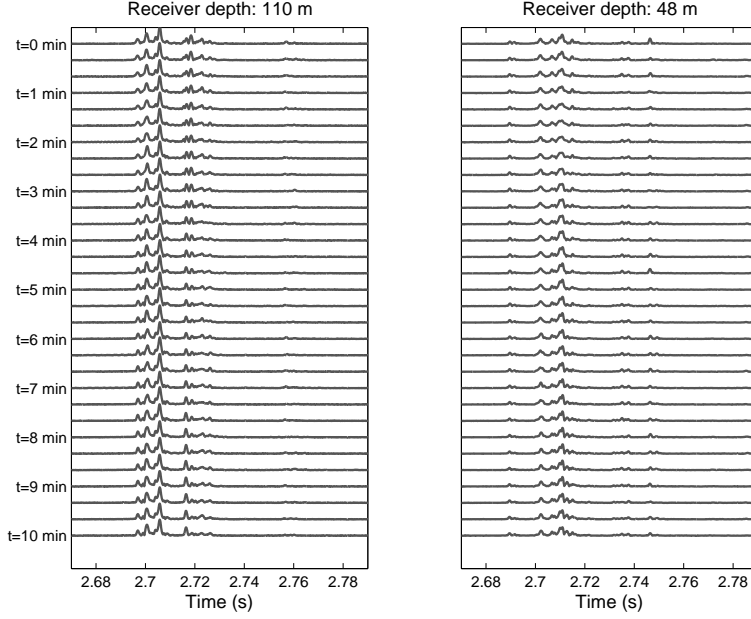
Figure 3.4: Temporal evolution of FAF05 Green's functions, for a source at 112.6 m.

experimentally available. A parabolic equation model is used to simulate acoustic propagation in a range-dependent environment, and a Garrett-Munk-based internal wave model is used to generate time-varying sections of sound speed profiles. [5]

To estimate the kernels, a single sound speed profile from a CTD cast (Fig. 3.2) taken at the beginning of the transmissions was used in a split-step Padé parabolic equation model (RAM)[17] was used to model sound propagation through a range-independent environment. [18] The parabolic equation had a delta-function starter, range and depth steps of 1 m and 0.05 m respectively, and 6 Padé coefficients, which gives negligible phase errors over a 75° angle range. Green's functions were computed every 8 Hz over the 2800 - 4200 Hz bandwidth. Fig. 3.5 shows the waveguide parameters employed for the simulation of acoustic propagation for the FAF05 environment.

The data-derived Green's function is obtained by match-filtering the receptions using a 2800 - 4200 Hz Hanning-windowed chirp with a roll-off factor of 0.2. In order to make a fair comparison with the data, the same match-filtering method

SRA (35–113 m)

VRA (48–110 m)

121 m

4.071 km

1520 m/s

2.5 m

1.75 g/cc          0.18 $dB/\lambda$

1600 m/s

1580 m/s

1.8 g/cc          0.2 $dB/\lambda$
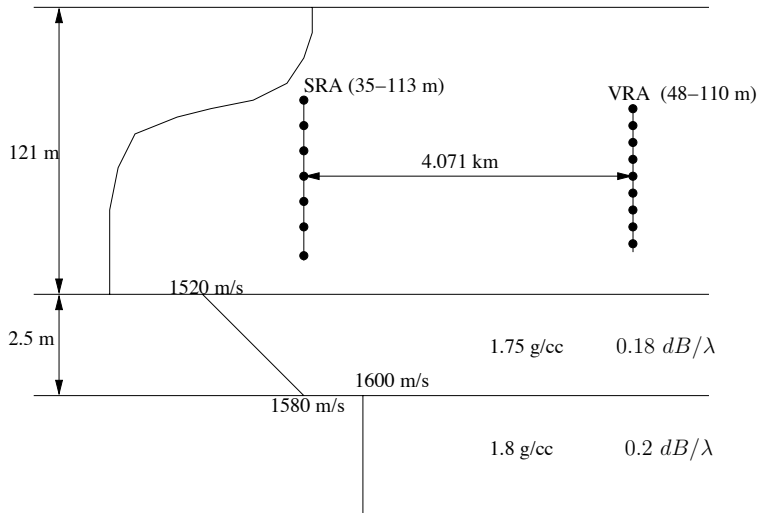
Figure 3.5: Waveguide parameters used in the acoustic propagation model.

was applied to the model-derived Green's functions.

Fig. 3.6 shows the full-depth Green's function on the VRA obtained using a source at 112.6 m. The same source depth is used for a number of plots in this paper. This is the deepest source depth available in the data, and gives the maximum stability when transmitting to a deep receiver. The upper panel shows the experimentally obtained Green's function, while the lower two panels show that obtained using the parabolic equation, for a range independent and range dependent sound speed profile. Range-dependent sound speed profiles were obtained using the internal wave model, described in the following paragraphs. The range-dependent calculation does not differ greatly from the range-independent calculation because the horizontal decorrelation scale is about 4 km, not much smaller than the range itself. Almost all the paths in the experimental Green's function are resolved by the parabolic equation. The close visual agreement between the two allowed for the use of an experimentally obtained range-independent sound speed profile in order to compute the sensitivity kernels.

Internal waves are a major source of sound speed fluctuations, particularly in the absence of any significant surface wave activity, as was the case during the course of the FAF05 experiment. In addition, the downward-refracting sound
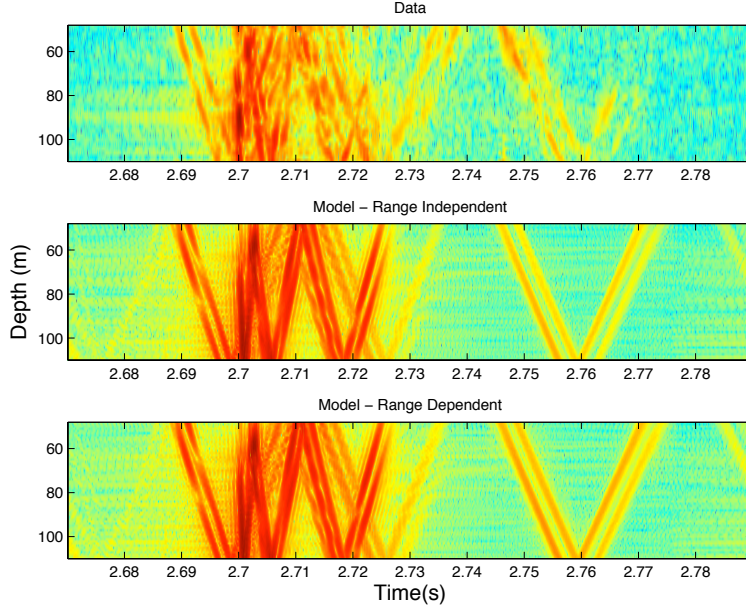
Figure 3.6: Green's functions, model v/s data, for a source at 112.6 m

speed profiles encountered (Fig. 3.2) minimize the effects of surface waves on the energetic arrivals. A modified Garrett-Munk internal wave model,[5, 19] was used to calculate vertical displacements, from which sound speed fluctuations were calculated according to,

$$\delta c(r, z, t) = c_p[z - \eta(r, z, t)] - c_p(z) \tag{3.1}$$

where $c_p(z)$ is the potential sound speed and $\eta(r, z, t)$ is the vertical displacement of internal waves. The method used to calculate the vertical displacements due to the internal waves, identical to that followed by Kim et. al.[5], is summarized in the Appendix. Model parameters such as the internal wave spectrum, vertical mode shapes, mode amplitudes and variance of temperature fluctuations are validated against the thermistor chain data.

Fig. 3.7 shows a representative buoyancy profile calculated from a CTD cast whose details are shown in Fig. 3.2. The internal wave spectrum calculated using this buoyancy profile is also shown, along with the power spectrum of the temperature time series. The energy parameter for the internal wave model (Appendix) is constrained by choosing a value such that the peak standard deviation of model
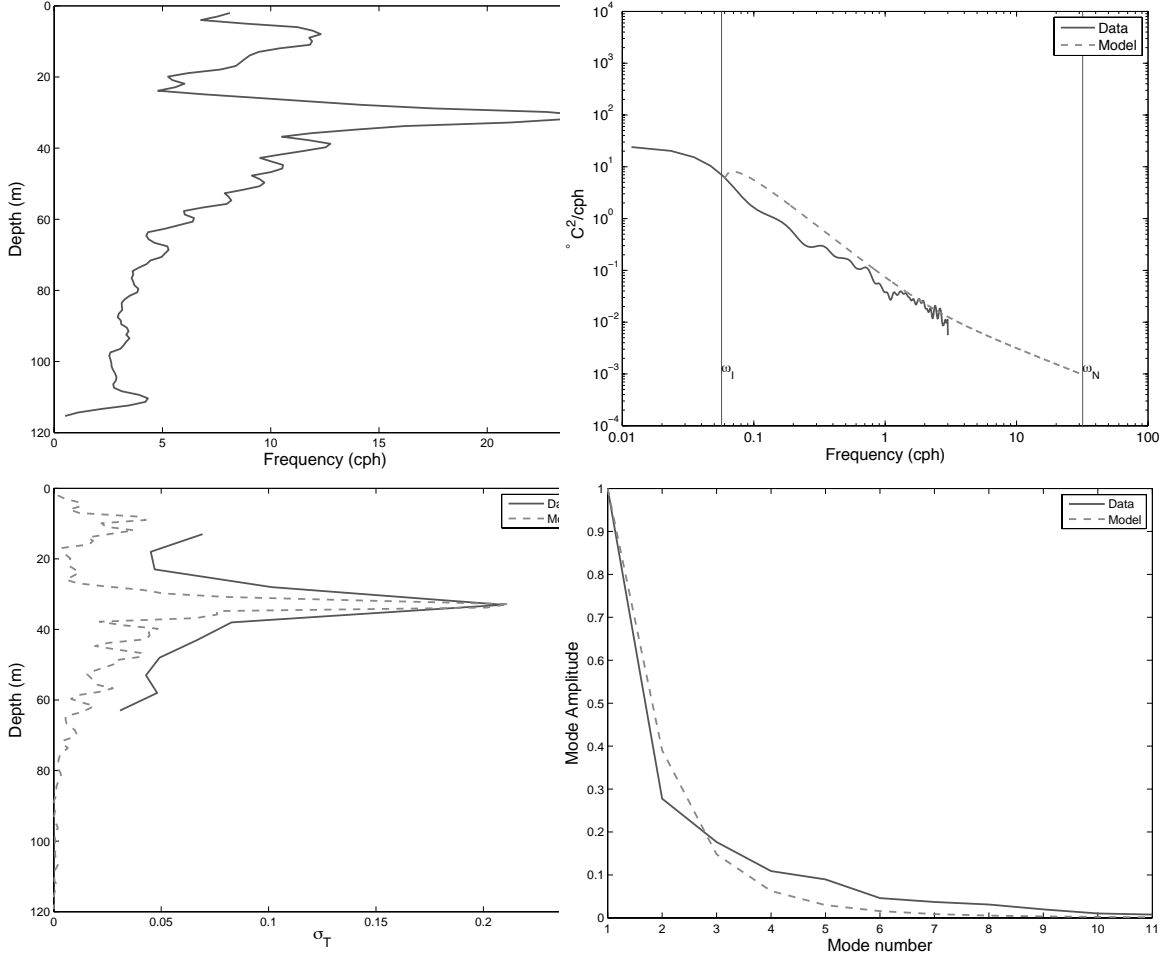
Figure 3.7: **Top left:** Buoyancy profile calculated from CTD data, **Top right:** G-M model spectrum (dashed) v/s thermistor chain spectrum (solid), **Bottom left:** Standard deviation of model-based and thermistor chain temperature fluctuations, **Bottom right:** G-M model mode amplitudes v/s temperature EOF mode amplitudes

fluctuations matches that of the temperature fluctuations, high-pass filtered above the inertial frequency. Even so, the energy parameter that is used is probably too low due to the sharp thermocline in the single profile. Undoing the effect of these sharp transitions is currently work in progress. Mode amplitudes as used by the model are compared to temperature chain data by projecting the temperature data onto its EOF modes to yield the mode amplitudes for the temperature time series. Mode shapes are also compared to the temperature data, and the first four mode shapes are shown in Fig. 3.8. The first mode two mode shapes, which contribute

about 75% (Fig. 3.7) of the total internal wave energy, show a match between the model and data. Details of the method used to calculate mode shapes and mode amplitudes may be found in the Appendix.
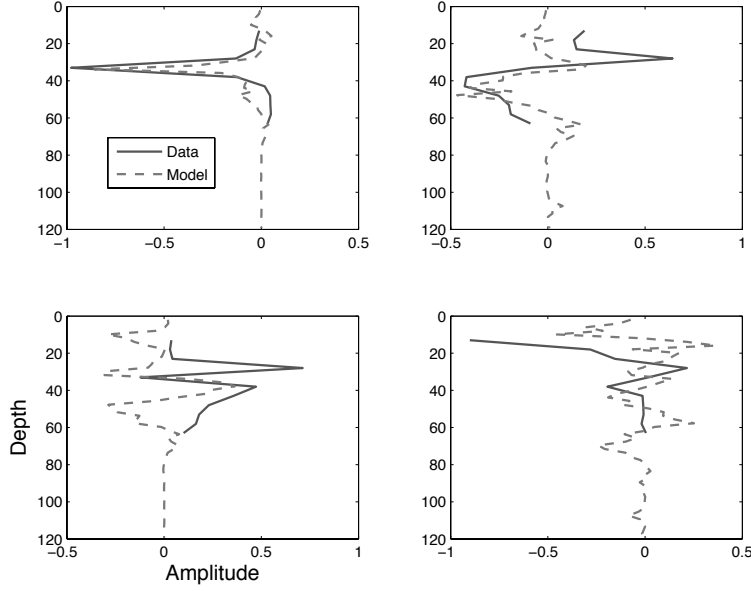


Figure 3.8: Model mode shapes (dashed) v/s data-derived EOF mode shapes (solid)

The final model test involves combining the internal wave model and acoustic propagation code, and comparing the behavior of the time-reversal focal spot between theory and observation. Ten source transducers were chosen, spaced 5.6 m apart, spanning the same depths as ten similarly-spaced SRA transducers. The internal wave model was used to generate 2 days of range-dependent sound speed profiles. The parabolic equation model was then implemented for the first 10 minutes of sound speed profiles. The first set of Green's functions between the source array and the receiver is time-reversed and used as the source shading function in order to compute the time-evolving focal spot for the model. Next, focal spots for the FAF05 data are computed by taking 10 minutes of the Green's function data, time-reversing the first set, and match-filtering with the rest to give time-evolving focal spots. Fig. 3.9 shows the evolution of the peak pressure for the time-reversal focal spot at four different depths in the water column. The vertical bars represent

90% confidence intervals obtained using 9 different 10-minute segments of Green's functions. While the model is able to capture the initial slope in the evolution of the focal spot, some observed changes in slope are not reproduced. This limitation is particularly relevant in the context of pressure sensitivity kernels, which will be discussed in the next section. The ability to model the slope, however, is a test of the validity of the energy parameter used in the internal wave model. For example, a larger energy parameter should increase the rate at which the focal spot pressure varies. This method can also be used as a means to constrain the energy parameter of an internal wave model.
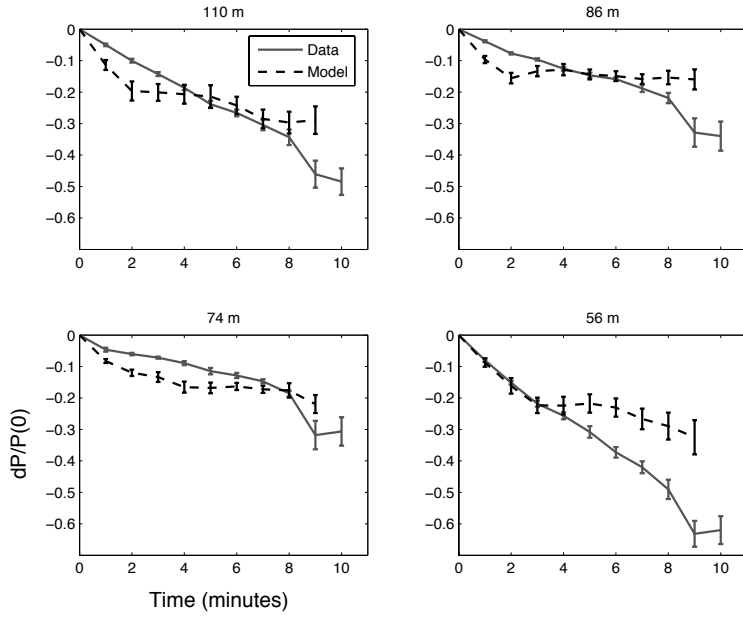


Figure 3.9: A comparison of the evolution of the time-reversal focal spot peak amplitude for the model and data.

## 3.4 Pressure sensitivity kernels

### 3.4.1 Background

This section essentially summarizes the derivation of pressure sensitivity kernels as presented in Skarsoulis et. al.[12]

The pressure perturbation to the Green's function $G(\boldsymbol{r}|\boldsymbol{r}_{\mathrm{s}})$ between at a location $\boldsymbol{r}$ due to a harmonic point source of unit strength located at $\boldsymbol{r}_s$ can be expressed as

$$\Delta G(\boldsymbol{r}|\boldsymbol{r}_{\mathrm{s}}) = -2\omega^2 \int_V G(\boldsymbol{r}|\boldsymbol{r}')G(\boldsymbol{r}'|\boldsymbol{r}_{\mathrm{s}})\frac{\Delta c(\boldsymbol{r}')}{c^3(\boldsymbol{r}')}d\boldsymbol{r}' \tag{3.2}$$

where $\omega$ the circular frequency of the source, and $c(\boldsymbol{r})$ is the sound-speed distribution.

This is called the first Born approximation.[20] It is also called the single- or weak-scattering approximation, or wave-field linearization, and is widely used in connection with scattering problems.[21] It is a linear relation between the perturbation in the sound-speed distribution and the induced perturbation in the Green's function. The integration volume in eq. 3.2 is all space or the region encompassing the source and receiver over which sound speed perturbations result in perturbations to the Green's function.

A key assumption upon which the validity of the first order Born approximation rests is that $\Delta c/c$, integrated over the volume, be small. The limits of the first Born approximation in connection with experimental data are explored in the next sub-section.

For a single point source the resultant pressure field can be written as

$$P(\boldsymbol{r}_r; \omega; c) = G(\boldsymbol{r}_r|\boldsymbol{r}_s; \omega; c)S(\boldsymbol{r}_s; \omega) \tag{3.3}$$

where $P(\boldsymbol{r}_r; \omega; c)$ is the frequency-domain pressure at receiver location $\boldsymbol{r}_r$, from a source located at $\boldsymbol{r}_s$. $G(\boldsymbol{r}_r|\boldsymbol{r}_s; \omega; c)$ is the frequency-domain Green's function that turns pressure at the source at frequency $\omega$ to pressure at the receiver. $S(\boldsymbol{r}_s; \omega)$ is the signal at source $\boldsymbol{r}_s$ at frequency $\omega$. For an array transmitting to a single receiver, the received signal is given by adding up all source contributions:

$$P(\boldsymbol{r}_r; \omega; c) = \sum_{i=1}^{N_s} G(\boldsymbol{r}_r|\boldsymbol{r}_{si}; \omega; c)S(\boldsymbol{r}_{si}; \omega) \tag{3.4}$$

where $\boldsymbol{r}_{si}$ is the location of the $i^{th}$ source element, and $N_s$ is the number of source elements.

In a perturbed propagation environment, the frequency domain perturbation to the received pressure can be approximated by substituting the perturbed

Green's function into eq. 3.4

$$\Delta P(\boldsymbol{r}_r; \omega; c) = \sum_{i=1}^{N_s} \Delta G(\boldsymbol{r}_r | \boldsymbol{r}_{si}; \omega; c) S(\boldsymbol{r}_{si}; \omega) \tag{3.5}$$

Using eq. 3.2 for the perturbed Green's function yields and expression for the pressure perturbation at the receiver for an arbitrary source function,

$$
\begin{aligned}
\Delta P(\boldsymbol{r}_r; \omega) &= \int_V \sum_{i=1}^{N_s} -2\omega^2 \, G(\boldsymbol{r}_r | \boldsymbol{r}; \omega; c) \, G(\boldsymbol{r} | \boldsymbol{r}_{si}; \omega; c) \frac{\Delta c(\boldsymbol{r})}{c^3(\boldsymbol{r})} S(\boldsymbol{r}_{si}; \omega) d\boldsymbol{r} \\
&= \int_V K_{ap}(\boldsymbol{r}; \omega; c) \Delta c(\boldsymbol{r}) d\boldsymbol{r} \tag{3.6}
\end{aligned}
$$

where $K(\boldsymbol{r}; \omega; c)$ is the sensitivity of the received pressure to a sound speed perturbation at location $\boldsymbol{r}$, for an array of sources transmitting to a single receiver.

Eq. 3.6 is a linear relation between the pressure perturbation at the receiver and sound speed perturbations in the medium, valid when $\Delta c/c$ is sufficiently small. It provides the framework for studying the effect of a source transmission scheme on the received pressure perturbation. Replacing $S(\boldsymbol{r}_S; \omega)$ by $G^*(\boldsymbol{r}_r | \boldsymbol{r}_s; \omega; c)$, will result in an expression for the pressure perturbation for time-reversal. Replacing $S(\boldsymbol{r}_s; \omega)$ by $1/G(\boldsymbol{r}_r | \boldsymbol{r}_s; \omega; c)$ will result in an expression for the pressure perturbation for the inverse filter.[22] In Sec. V, eq. 3.6 is examined in terms of an optimization problem where the goal is to obtain a set of source transmissions that will minimize pressure perturbations at the receiver.

### 3.4.2   Experimental demonstration

In this section, the validity of pressure sensitivity kernels, briefly summarized in the previous section and the references contained therein, is tested using experimental data collected during the FAF05 experiment.

The same parabolic equation code mentioned in Sec. III-A is used to calculate the pressure sensitivity kernel (eq. 3.6) for a given source-receiver pair. For every source-receiver pair, two forward runs of the code are required. The first with the source placed at the source depth, propagated out to the range of the receiver, and the second with the source placed at the depth of the receiver, propagated out

to the same range. The results of the second run, flipped in the range dimension is multiplied at each range and depth step with the result of the first run to yield the pressure sensitivity kernel at each range and depth step, for each frequency (eq. 3.6). The background sound speed profile at which the sensitivity kernels are calculated is obtained from one of the CTD casts, taken at the beginning of the transmissions (Fig. 3.2). Sensitivity kernels are calculated for a range-independent sound speed profile, on top of which range-dependent sound speed perturbations are imposed in order to compute Green's function perturbations.

Fig. 3.10 shows the pressure sensitivity kernels, in the time-domain, for a source at a depth of 112.6 m and a receiver at a depth of 110 m. These depths correspond to the depths of the deepest element of the SRA and VRA respectively. The Green's function is shown on the upper panel, with various paths identified as *A-F*. FAF05 observations of the Green's functions for the same source and receiver depths can be seen in Fig. 3.4. Time-domain sensitivity kernels are calculated by taking the inverse Fourier transform of the frequency domain sensitivity kernels and then evaluating the resulting time-series at the time-of-arrival of the various paths.

The pressure sensitivity kernels in Fig. 3.10 show an oscillatory structure around the ray paths which is associated with Fresnel-zone behavior[12], arising from the interference of two plane waves (eq. 3.6).[23] While the Fresnel-zone is a single frequency concept, the broadband analogue, called the "zone-of-influence"[24], is a superposition of several single-frequency Fresnel zones. The effect of bandwidth then is a decaying of the oscillatory structure away from the first zone, with increased bandwidth resulting in a faster decay. The effect of increasing central frequency is a narrowing of the width of each zone-of-influence. The combined effect of increasing bandwidth and central frequency is that the wave-theoretic sensitivity kernel starts to approach the ray-theoretic kernel.

Next, the limits of the linear first Born approximation used to derive the pressure sensitivity kernels (eq. 3.2), are tested numerically for the sound speed profiles observed in the experiment. The linearity test involves computing a perturbed Green's function via a forward model run, and then comparing with the
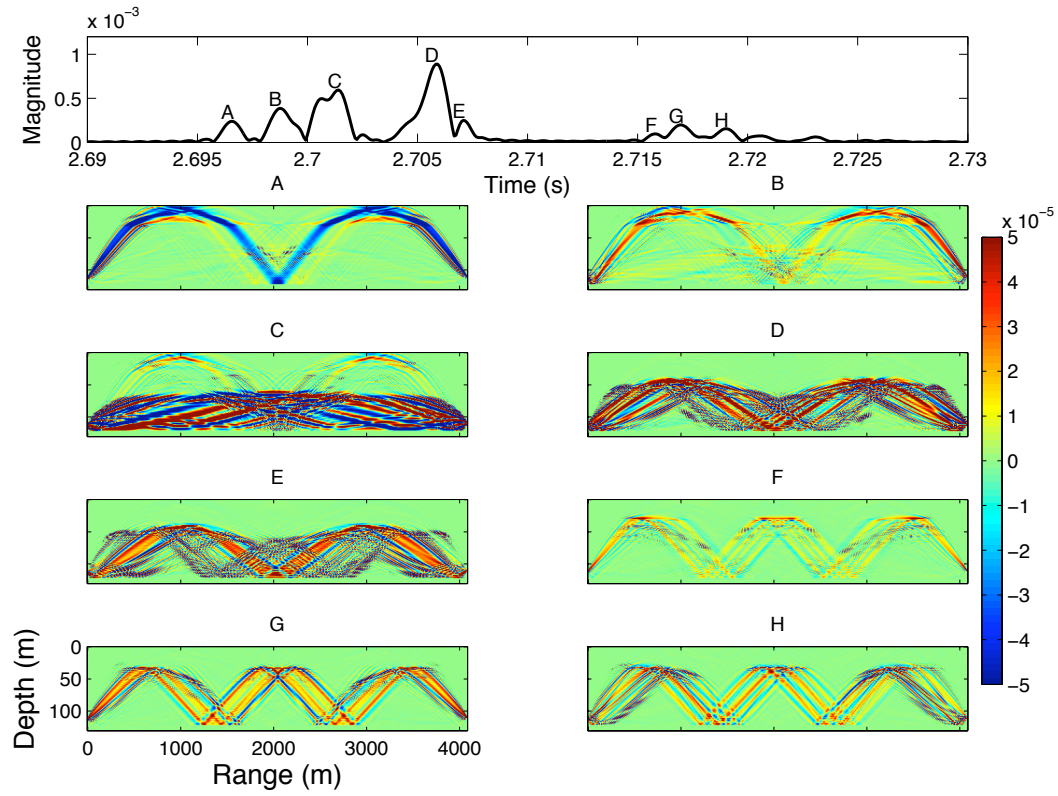
Figure 3.10: Sensitivity kernels for FAF05 paths, for a source at 112.6 m, and receiver at 110 m. The topmost panel shows the specific Green's function for whose paths sensitivity kernels are shown in the lower panels. Units of sensitivity are $\mu Pa\ s\ m^{-4}$. FAF05 Green's function observations can also be seen in Fig. 3.4.

estimate obtained using the sensitivity kernel. The estimate produced using the sensitivity kernel is given by

$$G_{kernel}(t) = G_{orig}(t) + \sum_{r,z} K(r, z, t)\delta c(r, z) \qquad (3.7)$$

where $G_{orig}(t)$ is the unperturbed time-domain Green's function, $K(r, z, t)$ the time-domain sensitivity kernel and $\delta c(r, z)$ the sound speed perturbation.

A single arrival (arrival C in Fig. 3.10) is considered. The arrival is refracted and bottom-reflected. A sound speed perturbation uniform in range and depth is introduced so that the arrival pattern is nearly uniformly advanced or delayed. The linearity of several different sensitivity kernels is tested: the full-wave kernel as given by eq. 3.6 for a one-way transmission (unity source function), the envelope

kernel for a one-way transmission, the full-wave kernel for time-reversal with a single source, and the envelope kernel for time-reversal with a single source. The envelope kernel is given by[25]

$$K_{env}(t) = \frac{G_R(t) \ K_R(t) \ + \ G_I(t) \ K_I(t)}{|G(t)|} \tag{3.8}$$

where $G_R(t)$ and $G_I(t)$ are the real and imaginary parts of the unperturbed basebanded Green's function, and $K_R(t)$ and $K_I(t)$ are the real and imaginary parts of the basebanded pressure sensitivity kernels.

The results of the linearity tests (Fig. 3.11) show the highly quadratic nature in which the magnitude of the arrival reacts to sound speed changes. For a one-way transmission, using the envelope of the sensitivity kernel increases the range of linearity over which the first Born approximation is valid. The range of linearity for time-reversal (full-wave) is less than the range over which the linear approximation is valid for a one-way transmission. Time-reversal effectively delays each path such that they all arrive at the same time at the receiver. In terms of sensitivity kernels, this results in a single sensitivity kernel for the peak of the focal spot which is characterized by several overlapping sensitivity kernels, one for each path.[14] The reduced linearity exhibited by the kernels for time-reversal is a a result of this overlap, since the amplitude of each multipath will affect the kernel of the combination at a full-wave level. This is similar to the problem faced in tomography, where an arrival peak made up of two different ray paths is not generally useful for inversion.[12] The time-reversal kernel, therefore, cannot be expected to reproduce the evolution of the focal spot for very long. The quadratic nature of the peak amplitude variation can be tackled using the second Born approximation, demonstrated by Piperakis et. al. in weakly range-dependent ocean environments[26], but is beyond the scope of this paper. The optimized source functions, described in the next section, are derived and tested within the range of sound speed perturbations over which pressure perturbations are linear.

Next, the sensitivity kernels are used to calculate Green's functions in order to study how long one can expect the assumption of linearity to hold for the FAF05 environment. This is done by first computing a baseline and a perturbed Green's function using a forward run of the parabolic equation model. The sensitivity
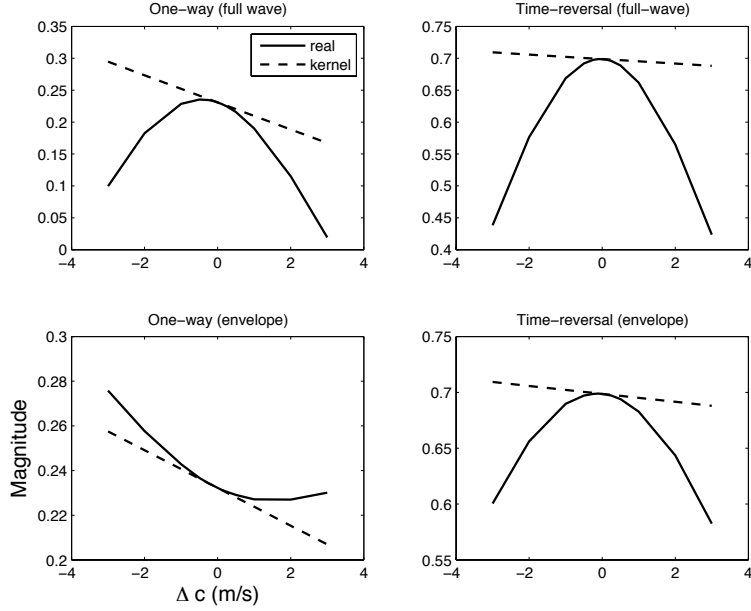
Figure 3.11: Linearity test of one-way and time-reversal sensitivity kernels. Sound speeds are varied uniformly over the waveguide, and the resulting change in peak pressure is measured as returned by a forward run (solid), and the kernel estimate (dashed).
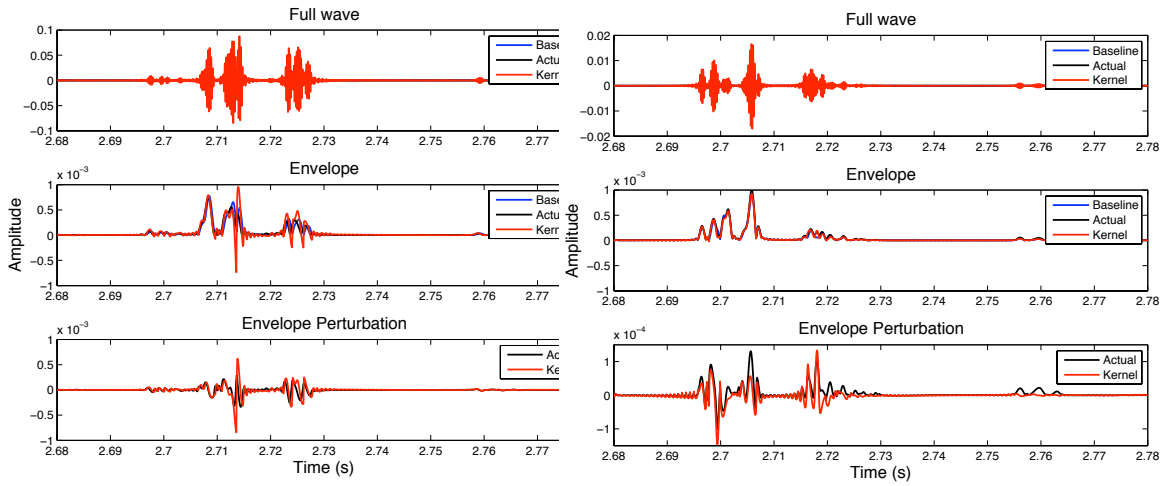


Figure 3.12: **Left:** Kernel linearity test using TC chain derived ssp's (10 minutes apart), **Right:** Kernel linearity test using range dependent IW model. Blue lines represent unperturbed Green's functions, black lines the perturbed forward run, and red lines the kernel estimate.

kernel is then used, along with the known sound speed perturbation, to estimate a Green's function perturbation, which is then compared to that obtained using the forward run. The source is at a depth of 112.6 m and receiver at a depth of 110 m. Two such tests are conducted. The first uses range-independent sound speed profiles computed using the thermistor chain data. The second test uses range-dependent sound speed profiles obtained from the internal wave model. For each test, results are displayed in three ways. The first simply displays the baseline, perturbed and kernel-estimated Green's functions (called the full-wave Green's function, due to the presence of carrier-frequency modulation). The second displays the envelope of the baseline and perturbed Green's function together with the kernel estimate computed using the envelope kernel (eq. 3.8). The third displays the perturbation to the envelope compared to the baseline Green's function.

For the left panel of Fig. 3.12 sound speed profiles are computed from the thermistor chain data located close to the VRA (TC2), at roughly the same time that the CTD shown in Fig. 3.2 was taken. The sound speed profiles are assumed to be range-independent. The Green's function as predicted by the full-wave kernel is considerably higher in amplitude than both the original Green's function and the actual perturbed Green's function. The envelope kernel does a much better job of predicting the perturbed Green's function, as seen in the middle panel. This is in agreement with the lower left figure in Fig. 3.11 where the envelope kernel is seen to have a larger range of linearity. The lowest panel in Fig. 3.12 shows the perturbation to the envelope of the Green's function. While the envelope kernel is able to predict the envelope perturbation at a 10 minute interval, it was seen to degrade rapidly for longer intervals.

The linearity of the sensitivity kernels are then tested along with the range-dependent sound speed profiles taken from the internal wave model. The results shown in the right hand panels of Fig. 3.12. The baseline Green's function is the same as in Figs. 3.6, 3.10. Again, while the full-wave kernel quickly loses its validity, the use of the envelope kernel is able to extend the linear regime over which perturbations can be predicted.

## 3.5 Optimized source functions

The mathematical framework that expresses the pressure sensitivity as a function of the source transmission, summarized in Sec. IV, allows for the derivation of optimized source functions that can give an inverse filter-like focal spot, whose quality can be traded-off for robustness to sound speed fluctuations. While the complete derivation can be found in Raghukumar et. al.[14], a brief summary is given below. The main focus of this section is on comparing the focal spot obtained using the optimized source functions with experimental time-reversal data gathered during the FAF05 experiment.

### 3.5.1 Theory

The optimized source functions are derived through a joint optimization process that seeks to minimize two cost functions: the first being a minimization of pressure perturbations at the receiver due to the changing sound speed, with the second being to obtain a focal spot that is a delta-function in depth and time.

In order to be able to perform the derivation using linear algebra, the various quantities involved, such as sensitivity kernels, sound speed profiles, and source functions, are discretized. The frequency-domain sensitivity kernel, originally three-dimensional $(N_z \times N_x \times N_s)$, where $N_z = 60$ is the number of depth points, $N_x = 204$ is the number of range points, and $N_s = 10$ the number of sources, is stacked in range to give the two-dimensional discrete sensitivity kernel $\mathbf{K}(\omega)$ with dimensions $N_z N_x \times N_s$. Similarly the two-dimensional sound speed profile is also stacked in range to give the $N_z N_x \times 1$ vector $\Delta \mathbf{c}$. The pressure perturbation (eq. 3.4) is then written as

$$\Delta P(\omega) = [\mathbf{K}(\omega) \, \mathbf{s}(\omega)]^T \, \Delta \mathbf{c} \tag{3.9}$$

where the superscript $(\cdot)^T$ denotes matrix transpose. This is the pressure pertur-

bation that is to be minimized via the cost function

$$
\begin{aligned}
J_1(\omega) &= \ <|\Delta P|^2> \\
&= \ \mathbf{s}(\omega)^H \ \mathbf{K}(\omega)^H <\Delta\mathbf{c}\Delta\mathbf{c}^T> \mathbf{K}(\omega) \ \mathbf{s}(\omega) \\
&= \ \mathbf{s}(\omega)^H \ \mathbf{K}(\omega)^H \ \mathbf{C}_{dc} \ \mathbf{K}(\omega) \ \mathbf{s}(\omega) \\
&= \ \mathbf{s}(\omega)^H \ \mathbf{C}_{mdc} \ \mathbf{s}(\omega)
\end{aligned}
\tag{3.10}
$$

where $\mathbf{C}_{dc}$ is the sound speed perturbation covariance matrix and the superscript $(\cdot)^H$ denotes matrix complex conjugate. $\mathbf{C}_{mdc}$ is the $N_s \times N_s$ covariance matrix of the Born-approximation perturbed Green's functions at frequency $\omega$ between an array of sources and a single receiver. So element $ij$ of $\mathbf{C}_{mdc}$ is the covariance between the pressure perturbation at the receiver from a transmission from source $i$ and the pressure perturbation at the receiver from a transmission from source $j$.

The second condition that is addressed is that a focal spot be present. In the process of achieving this, the inverse filter was re-derived. While time-reversal maximizes the acoustic intensity at the focal spot, the inverse filter adds additional constraints such as the minimization of sidelobes in depth, range and time. The derivation starts with a Bayesian linear model

$$
\mathbf{u}(\omega) = \mathbf{G}(\omega)\mathbf{s}(\omega) + \mathbf{r}
\tag{3.11}
$$

where $\mathbf{u}(\omega)$ is an objective function, whose frequency-domain representation is a delta function in depth and time, defined at $N_p$ depths. $\mathbf{G}$ is the $N_p \times N_s$ matrix of Green's functions, and $\mathbf{r}$ a misfit vector. Solving eq. 3.11 is equivalent to minimizing the cost function

$$
J_2 = \mathbf{r}^H \mathbf{C_r}^{-1}\mathbf{r} + \mathbf{s}^H\mathbf{C_s}^{-1}\mathbf{s}
\tag{3.12}
$$

The joint minimization of $J_1$ and $J_2$ with respect to $\mathbf{s}$ results in the maximum *a posteriori* estimator[27, 14]

$$
\hat{\mathbf{S}}(\omega) = (\frac{\alpha}{\beta}\mathbf{I} + \gamma\mathbf{C}_{mdc} + \mathbf{G}^H\mathbf{G})^{-1}\mathbf{G}^H\mathbf{u}
\tag{3.13}
$$

which is obtained by assuming that $\mathbf{C_r} = \alpha\mathbf{I}$ and $\mathbf{C_S} = \beta\mathbf{I}$. $\gamma$ is introduced through a scaling parameter for the sensitivity cost function $J_1$ when adding the two

cost functions together to perform the joint optimization. The optimized source function (eq. 3.13) may be recognized as a regularized inverse filter,[8] with the terms $\frac{\alpha}{\beta}\mathbf{I}+\gamma\mathbf{C}_{mdc}$ being the physics-based regularization term that adds robustness to environmental perturbations to an inverse filter-like focal spot. These functions are different from the robust time-reversal method proposed by Kim et. al.[5] where the cost of stability was a focal spot being smeared out in range, depth and time.

### 3.5.2   Experimental demonstration

This section brings together experimental time-reversal data, the internal wave model, the parabolic equation propagation model, and the optimized source functions.

In order to compute the optimized source functions, the various components of eq. 3.13 need to be computed. The covariance matrix $\mathbf{C}_{mdc}$ is the weighted inner product of the sensitivity kernel $\mathbf{K}(\omega)$ with the weighting vector $\mathbf{C}_{dc}$, the covariance matrix of sound speed perturbations. As outlined in Sec. IV, an experimentally gathered range-independent sound speed profile is used to conduct the forward model runs. Sensitivity kernels are calculated using the parabolic equation model, between 9 sources and 11 receivers over a 1.4 kHz bandwidth (2.8 kHz-4.2 kHz). The internal wave model is used to generate an ensemble of range-dependent sound speed profiles from which the covariance matrix for sound speed perturbations is calculated. The Green's function matrices, $\mathbf{G}$ may either be calculated using the acoustic propagation code, or if available, taken directly from experimental data. The presence of source and receive vertical arrays during the FAF05 experiment allowed for the use of experimental Green's functions in eq. 3.13. Although there were 29 source elements and 32 receive elements only 9 source elements and 11 receive elements are used in the examples. The 9 sources are chosen to be every third SRA hydrophone starting from the bottom, and the 11 receivers are chosen to be every fourth VRA hyrdrophone starting from the bottom. This is done in order to observe greater differences between time-reversal and the inverse filter/optimized source functions. The relative gains of using an optimized source transmission

scheme are diminished with an increasing number of source elements since the quality of the time-reversal focal spot improves significantly.

The next quantity that needs to be chosen in eq. 3.13 is the shape of the focal spot $\mathbf{u}(\omega)$. Initially, $u(z,t)$ is set to be a delta function in the baseband sampled at twice the bandwidth (1.4 kHz). This is then centered around the carrier frequency (3.5 kHz) and Fourier-transformed using a 12 kHz sampling rate to give $\mathbf{u}(\omega)$, whose amplitude is adjusted to be the same as that of the time-reversal focal spot. For a given bandwidth, this is the best attainable focal spot. The inverse filter is computed using eq. 3.13 with $\alpha = \gamma = 0$. The focal spot produced by this inverse filter is then chosen to be the new objective function $\mathbf{u}(\omega)$ that is used in further calculations. The use of this objective function will result in the focal spot cost function $J_2^{IF}$ (eq. 3.12) to be zero for the inverse filter. Next, the scaling parameter $\alpha$ is chosen such that the focal spot cost function for time-reversal $J_2^{TR} = 1$. The focal spot cost function for the optimized source function will thus be conveniently between 0 (inverse filter) and 1 (time-reversal). Finally, $\beta$ and $\gamma$ are varied such that desirable cost function characteristics are achieved, such as a focal spot that is similar to the inverse filter, and with a peak stability greater than time-reversal. Fig. 3.13 shows a representative plot of the cost functions that are a result of computing optimized source functions at one of the times a CTD was taken during the FAF experiment (133000 UTC on 16 July 2005). Additional plots of cost functions for various scenarios may be found in Raghukumar et. al.[14]

Time-reversal focal spots are computed by choosing a time-reversed Green's function at the beginning of a 20-minute window as a source shading function, and then correlating this with Green's functions experimentally acquired every minute. Optimized source transmissions and the inverse filter are calculated using eq. 3.13, with $\alpha$ and $\gamma$ set to zero to produce the inverse filter. Focal spots are then computed by calculating the respective source shading function as outlined above, and then correlating these with experimental Green's functions over the 20-minute window. In the FAF experiment, nine CTD's were taken during the time that Green's function estimates were made. Sensitivity kernels and optimized source fuunctions
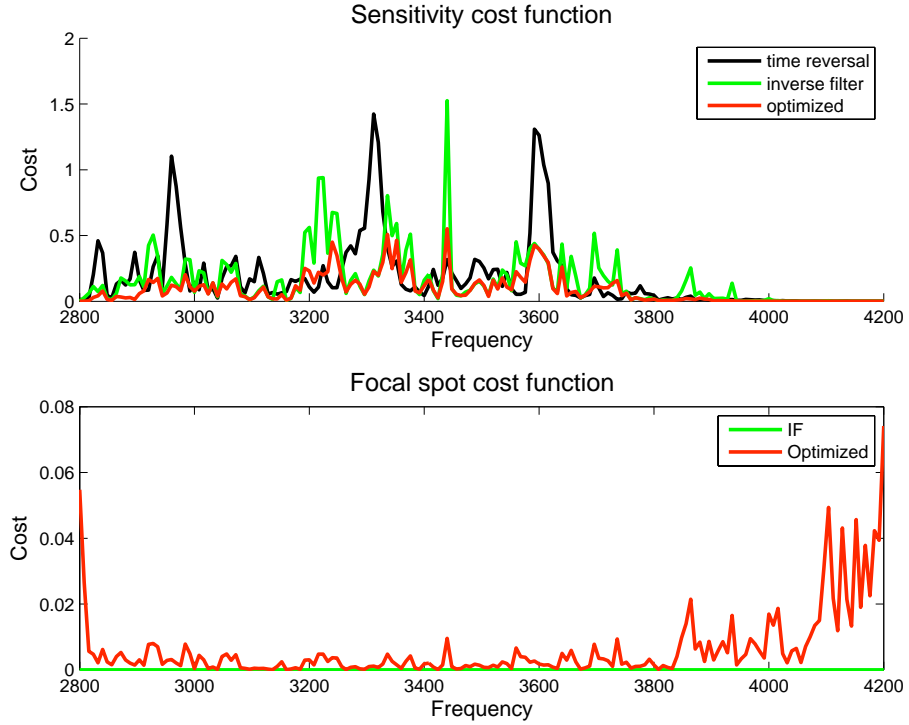
Figure 3.13: **Upper:** Sensitivity cost function ($J_1$ in eq. 3.10) for time-reversal (black), inverse filter (green) and optimized source functions (red), and **Lower:** Focal spot cost function ($J_2$ in eq. 3.12) for the inverse filter and optimized source function. The plot is normalized so that the focal spot cost function for time-reversal is fixed at 1 and that of the inverse filter is 0.

are calculated using the range-independant parabolic equation code for each of the CTD profiles. Focal spots are compared for 20-minute windows beginning at the time the CTD's were taken. This allows for calculating error bars for the various focal spot metrics by averaging over the 9 realizations. The linearity of the kernels is only valid for approximately 10 minutes, after which the linear first Born approximation breaks down and the sensitivity kernels are no longer able to track the evolution of the Green's function due to evolution of the sound speed field. However, focal spots are still compared for a 20-minute window, in order to see if results change significantly as a result of the kernels no longer being in the linear regime. The values of $\beta$ and $\gamma$ were typically $10^{11}$ and $0.1\alpha$ respectively. The large value of $\beta$ is chosen due to $\alpha$ being on the order of $10^{14}$ due to the units used in

representing the experimental Green's functions. These choices of $\beta$ and $\gamma$ result in all the terms in eq. 3.13 that are inside the inverse being on the order of $10^3$.

Three metrics are used to evaluate the quality of focal spots for the different schemes. All metrics are computed relative to the values for time-reversal. The first is the peak-to-sidelobe ratio, where the sidelobe level is taken to be the magnitude of the highest sidelobe in depth or time. The peak-to-sidelobe ratio is a measure of the sharpness of the focal spot. The second metric reflects the sensitivity to sound speed perturbations, and measures the change in pressure at the expected time and depth of the focal spot due to changes in the sound speed field. The third metric is the peak power for each focusing scheme.
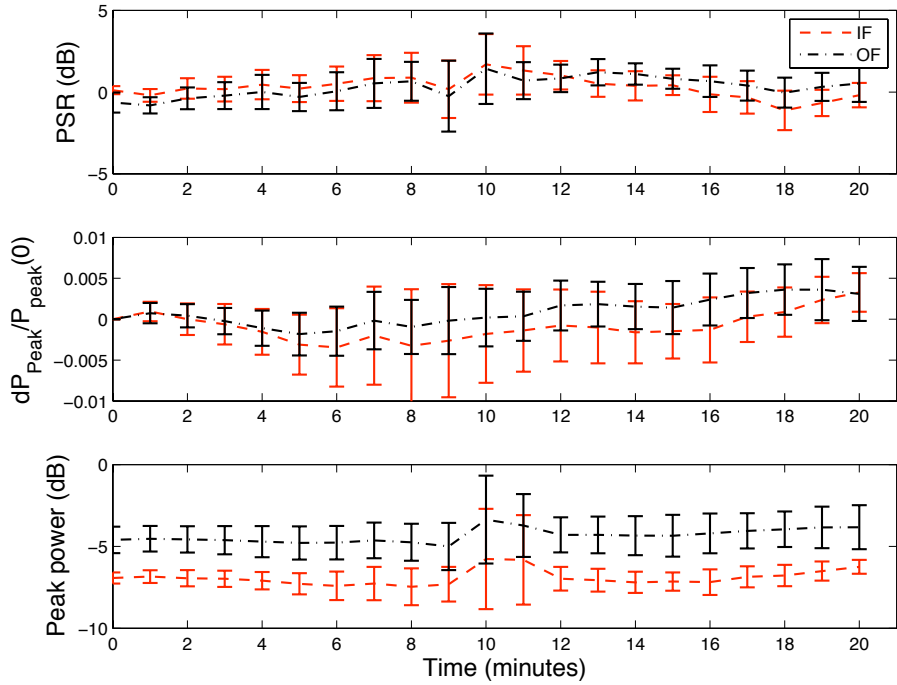


Figure 3.14: **Upper:** Peak-to-sidelobe ratio, **Middle:** peak stability and **Lower:** peak power for the inverse filter (red dashed) and optimized source function (black dot-dash), using experimentally derived Green's functions. The curves plot the changes with respect to time-reversal.

Fig. 3.14 shows the peak-to-sidelobe (PSR) ratio (top panel), peak stability (middle panel) and peak power (lower panel) for the inverse filter and optimized source function, along with error bars. In order to compare with time-reversal, the

curves for time-reversal have been subtracted out for each of the nine 20-minute windows, after which the mean and standard error are calculated. It should be pointed out that $dP$ in the middle panel is calculated using the pressure at the time of the peak of an unperturbed focal spot. Fluctuations of the peak will cause it to be shifted in time as a result of which $dP$ will always be negative. Hence, after the curve for time-reversal has been subtracted out, a positive value in the middle panel of Fig. 3.14 reflects a reduction with respect to time-reversal.

The optimized source function has a PSR that starts off a little higher than time-reversal, and builds up to about 0.5 dB higher than time-reversal 10 minutes into the window. The optimized source function closely follows this trend until about 12 minutes after which it starts to show the highest PSR. The peak sensitivity of the optimized source function is about the same as the inverse filter and time-reversal until about 5 minutes, after which it has the lowest peak sensitivity of all the three transmission schemes. The peak power for the inverse filter is about 7 dB lower than time-reversal, and that of the optimized source function is about 2 dB higher than the inverse filter. Time-reversal has the highest peak power since it is a matched filter, whose specific goal is to maximize peak power. Fig. 3.14 thus shows the optimized source function having a higher peak power than the inverse filter (but lower than time-reversal), while showing a reduced sensitivity to environmental fluctuations, at the cost of a lowered PSR compared to the inverse filter. The peak power, PSR and sensitivity for the optimized source function can be controlled by varying $\beta$ and $\gamma$. For example, in order to increase the peak power, $\beta$ or $\gamma$ can be reduced. However, this would come at the cost of increased sensitivity to sound speed fluctuations.

While the differences seen in Fig. 3.14 are small and the error bars mostly overlap, they are in the right sense, and provide insight into the use of sensitivity kernels for optimal signal design. In order to verify the results, the same exercise was undertaken using just the internal wave model. The internal wave model was used to generate 4 days of time-varying, range-dependent sound speed profiles, using which time-evolving Green's functions are computed for the first 10 minutes. Optimized source functions were then computed, and compared to time-reversal

and the inverse filter over nine of these 10-minute windows. The gains obtained using the optimized source functions were similar to those using data. It was found, however, that when the covariance matrix for sound speed perturbations used to compute the optimized source functions is calculated using just the 10 minutes of sound speed profiles, the gains are much higher. Thus, while using the longer covariance matrix better captures the internal wave dynamics over several days, one cannot expect this to result in sensitivity reduction over the relatively short 10 to 20 minute windows over which the kernels are valid.

Another drawback of the results shown in Fig. 3.14 is the overlap of error bars due to the small number of windows available to compute the optimized source functions. This limitation is due to the limited availability of CTD profiles during the transmissions, and that the sensitivity kernels operate in linear regime for only a few minutes after the time the CTD was taken. However, the results show that the optimized source functions are able to produce a focal spot that is inverse filter-like, while at the same time being more robust to environmentally induced sound speed fluctuations.

## 3.6    Conclusions

Pressure sensitivity kernels, which were introduced in a previous paper[14], are studied using experimental data via a multi-pronged approach. The results of an internal wave model are compared against thermistor chain data gathered during the FAF05 experiment. A parabolic equation code is then used to model time-reversal through a range-dependent environment, and the evolution of the focal spot is compared with experimental acoustic data. This can be thought of as an acoustic test of the internal wave model. Sensitivity kernels are then derived using environmental data gathered during the experiment with the intention of predicting the evolution of the time-reversal focal spot, and to demonstrate the use of optimized source functions. The first goal was not met due to the quadratic nature by which the peak pressure varies, a phenomenon that the linear sensitivity kernels are not capable of capturing. Time-reversal only exacerbates the problem

due to the presence of overlapping paths. In fact, the same process which makes time-reversal robust to sound speed fluctuations also reduces the linear regime for the time-reversal sensitivity kernel.

Sensitivity kernels were then used to derive optimized source functions that can provide a focal spot superior to time-reversal by taking advantage of knowledge of the propagation environment. The presence of adjustable parameters allows for fine-tuning focal spot properties such as peak-to-sidelobe ratio or robustness to environmental fluctuations. These optimized source functions were compared to experimental acoustic data gathered during a recent experiment, which validated their utility. In order to compute the optimized source functions, sensitivity kernels are calculated using a parabolic equation model. In addition, an internal wave model (validated against environmental data) was used to compute the covariance matrix for sound speed perturbations, also required to compute the optimized source functions.

The limitations of the scheme proposed are several. First, the internal wave model used may not be adequate, in which case insufficient, or inaccurate knowledge of the sound speed fluctuation covariance matrix is a limiting factor. The same is true if the background sound speed is not adequately known, in which case the sensitivity kernels would be inaccurate. If sound speed perturbations are large, then the linearity of the kernel is quickly violated. Finally, other sources of error, such as surface effects (which were small during FAF05), or array motion, if unaccounted for, would also limit the use of the optimized source functions.

While time-reversal is still an enormously attractive focusing scheme due its simplicity, it is often inadequate for applications such as underwater communications, which often require equalization in order to mitigate temporal sidelobe levels. On the other hand, the use of optimized source functions requires the computation of sensitivity kernels and the covariance matrix for sound speed perturbations, information which is often not available. However, the rich reception dataset available in FAF05 provided observed Green's functions, which made the use of these optimized source functions considerably easier.

## 3.7 Acknowledgments

The text in this chapter is in full a reprint of the material as it appears in Kaustubha Raghukumar, Bruce Cornuelle, William Hodgkiss, William Kuperman, "Experimental demonstration of pressure sensitivity kernels", to be submitted to J. Acoustic Soc. Am., 2009.

## 3.A Internal wave modeling

The vertical displacement of internal waves, $\eta(r, z, t)$ can be expressed as sum of vertical eigenmodes

$$\eta(r,z,t) = \int_0^{2\pi} \int_{\omega_I}^{N_{max}} \sum_l f(\omega_l(k), l, \theta)\phi_l(\omega_l(k), z) exp\ i(kr\cos\theta - \omega_l(k)t)d\omega d\theta$$

(3.14)

where $\omega_I$ is the local inertial frequency, $N_{max}$ is the maximum buoyancy frequency and $k$ and $\phi_l(\omega_l(k), z)$ are the horizontal wave number and vertical eigenfunction respectively. For the FAF05 experiment, $\omega_I$ at $43°\ N$ is 0.06 cycles per hour and $N_{max}$ is 31.8 cycles per hour. Due to the absence of azimuthal information in the thermistor chain data, the vertical displacement as given by the model is integrated in azimuth. $F(\omega, l) = \int_0^{2\pi} f(\omega, l, \theta)d\theta$ is a zero mean, complex Gaussian random variable associated with the internal wave power spectrum,[5]

$$|F(\omega, l)|^2 = bE_{GM}\rho\Big(\int N(z)dz\Big)^2 H(l)B(\omega)$$

(3.15)

where $bE_{GM}$ is the internal wave energy parameter $(1\ m)$, $\rho$ is the water density and $H(l)$ is the mode amplitude spectrum given by

$$H(l) = M(l^2 + l_*^2)^{-p/2}$$

(3.16)

and $M$ is a normalization factor such that $\sum_{l=1}^{ll_{max}} H(l) = 1$. The $p$ and $l_*$ determine the relative mode amplitude by power law.[5] The following functional spectrum

$B(\omega)$ was used, which is compared to the spectrum of detrended thermistor chain time series at a depth of 39 m in Fig. 3.7.

$$B(\omega) = W \frac{\omega_I \sqrt{\omega^2 - \omega_I^2} \sqrt{N_{1/3}^2 - \omega_I^2 + \omega^2}}{\omega^3} \tag{3.17}$$

where $W$ is a normalization factor such that $\int_{\omega_I}^{N_{max}} B(\omega) d\omega = 1$. The spectrum decreases with a slope of $\omega^{-2}$ and then $\omega^{-2/3}$ from $N_{1/3} = \int N(z) dz / 3D$.

The dispersion relation $\omega_l(k)$ and vertical eigenfunction $\phi_l(\omega_l(k), z)$ are calculated by numerically solving, via the WAVE code [28], the differential equation

$$\frac{d^2\phi}{dz^2} + k^2 \left[ \frac{N^2(z) - \omega^2}{\omega^2 - \omega_I^2} \right] \phi = 0 \tag{3.18}$$

subject to the boundary conditions $\phi(0) = \phi(D) = 0$ where D is the water depth. $N(z)$ is the buoyancy frequency, calculated from a representative CTD cast. A range of 50 horizontal wavenumbers $k$ is chosen to represent internal wave wavelengths ranging from 20 m to 1km. For each wavenumber $k$, WAVE returns an eigenfrequency $\omega_l(k)$ for mode $l$ and the mode shape $\phi_l(\omega_l(k), z)$. Mode shapes are calculated for 11 modes, in order to be consistent with the number of temperature sensors in the thermistor chain. In order to compare displacement mode shapes as returned by the model with those derived from the thermistor chain data, the displacement modes need to be converted to temperature modes. This conversion is done by first multiplying the displacement in eq. 3.14 by $dT/dz$ obtained from the CTD profile to give model temperature fluctuations. Next, the covariance matrix for temperature fluctuations is calculated whose eigenmodes can then be compared to those of the thermistor chain data. Fig. 3.8 shows a comparison between the eigenmodes calculated by the model and that computed from the displacement time series, for the first 4 modes.

The covariance matrix can be calculated directly from eq. 3.14 by recognizing that

$$\eta(r, z, k) \quad \sim \quad \sum_l B(k) H(l) \phi_l(k, z) e^{ikr} \tag{3.19}$$

$$\sim \quad \sum_l A(k, l) \phi_l(k.z) e^{ikr} \tag{3.20}$$

Discretizing the range and depth quantities gives the relation

$$\mathbf{d}\eta(k) = \mathbf{P}\ \mathbf{a} \tag{3.21}$$

where $\mathbf{P}$ is the $N_r N_z \times l$ matrix $\phi_l(k, z)\ e^{ikr}$ and $\mathbf{a}$ is the $l \times 1$ vector $B(k)H(l)$. $N_r$ is the number of range points and $N_z$ is the number of depth points. The covariance matrix for temperature fluctuations can then be calculated as

$$\mathbf{C}_{dT} = < \mathbf{dT}\ \mathbf{dT}^T >_k \tag{3.22}$$

where $\mathbf{dT} = \mathbf{d}\eta \cdot \mathbf{dT}/\mathbf{dz}$.

# Bibliography

[1] M. Fink, D. Cassereau, A. Derode, C. Prada, P. Roux, M. Tanter, J. L. Thomas, and F. Wu. Time-reversed acoustics. *Rep. Prog. Phys.*, 63:1933–1965, 2000.

[2] G. F. Edelmann, T. Akal, W. S. Hodgkiss, S. Kim, W. A. Kuperman, and H. C. Song. An initial demonstration of underwater acoustic communication using time-reversal. *IEEE J. Oceanic Engineering*, 27:602–608, 2002.

[3] H. Nguyen, J. Andersen, and G. Pederson. The potential use of time-reversal techniques in multiple element antenna systems. *IEEE commun. Lett.*, 9:40–42, 2005.

[4] W. S. Hodgkiss, H. C. Song, W. A. Kuperman, T. Akal, C. Ferla, and D. R. Jackson. A long-range and variable focus phase-conjugation experiment in shallow water. *J. Acoustic Soc. Am.*, 105:1597–1604, 1999.

[5] S. Kim, W. A. Kuperman, W. S. Hodgkiss, H. C. Song, and G. F. Edelmann. Robust time-reversal focusing in the ocean. *J. Acoustic Soc. Am.*, 114:145–157, 2001.

[6] M. Tanter, J.-F. Aubry, J. Gerber, J.-L. Thomas, and M. Fink. Optimal focussing by spatio-temporal inverse filter. I. Basic principles. *J. Acoustic Soc. Am.*, 110:37–47, 2001.

[7] J.-F. Aubry, M. Tanter, J. Gerber, J.-L. Thomas, and M. Fink. Optimal focussing by spatio-temporal inverse filter. II. Experiments. Application to focusing through absorbing and reverberating media. *J. Acoustic Soc. Am.*, 110:37–47, 2001.

[8] W. J. Higley, P. Roux, and W. A. Kuperman. Relationship between time-reversal and linear equalization in digital communications. *J. Acoustic Soc. Am.*, 120:35–37, 2006.

[9] H. Marquering, G. Nolet, and F. A. Dahlen. Three-dimensional waveform sensitivity kernels. *Geophs. J. Int.*, 132:521–534, 1998.

[10] F. A. Dahlen, S. H. Hung, and Guust Nolet. Frechét kernels for finite-frequency traveltimes-I. Theory. *Geophs. J. Int.*, 141:157–174, 2000.

[11] F. A. Dahlen, S. H. Hung, and Guust Nolet. Frechét kernels for finite-frequency traveltimes-II. Examples. *Geophs. J. Int.*, 141:175–1203, 2000.

[12] E. K. Skarsoulis and B. D. Cornuelle. Travel-time sensitivity kernels in ocean acoustic tomography. *J. Acoustic Soc. Am.*, 116:227–238, 2004.

[13] B. Sarkar, B. Cornuelle, and W. A. Kuperman. Estimating sound-speed perturbations with full-wave environmental sensitivity kernels. *J. Acoustic Soc. Am.*, 119:3246, 2006.

[14] K. Raghukumar, Bruce D. Cornuelle, William S. Hodgkiss, and William A. Kuperman. Pressure sensitivity kernels applied to time-reversal acoustics. *J. Acoustic Soc. Am.*, 124:98–112, 2008.

[15] H. C. Song, W. S. Hodgkiss, W. A. Kuperman, T. Akal, and M. Stevenson. Multiuser communications using passive time reversal. *IEEE J. Oceanic Engineering*, 32:915–926, 2007.

[16] W. A. Kuperman, W. S. Hodgkiss, H. C. Song, T. Akal, C. Ferla, and D. R. Jackson. Phase conjugation in the ocean: Experimental demonstration of an acoustic time-reversal mirror. *J. Acoustic Soc. Am.*, 103:25–40, 1998.

[17] M. D. Collins. A split-step padé solution for the parabolic equation method. *J. Acoustic Soc. Am.*, 93:1736–1742, 1993.

[18] F. B. Jensen, W. A. Kuperman, and M. B. Porter aand H. Schmidt. *Computational Ocean Acoustics*. American Institute of Physics, Woodbury, NY, 1994.

[19] F. S. Henyey, D. Rouseff, J. M. Grochoncinski, S. A. Reynolds, K. L. Williams, and T. E. Ewart. Effects of internal waves and turbulence on a horizontal aperture sonar. *IEEE J. Oceanic Engineering*, 22:270–280, 1997.

[20] M. Born. Quantum mechanics of impact processes. *Z. Phys.*, 38:803–827, 1926.

[21] J. R. Taylor. *Scattering Theory*. Wiley, New York, 1972.

[22] M. Tanter, J. L. Thomas, and M. Fink. Time-reversal and the inverse filter. *J. Acoustic Soc. Am.*, 108:223–234, 2000.

[23] J. Pearce and D. Mittleman. Defining the fresnel zone for broadband radiation. *Physical Review E*, 66:056602/1–4, 2002.

[24] M. Bruhl, G. J. O. Vermeer, and M. Kiehn. Fresnel zones for broadband data. *Geophysics*, 61:600–604, 1996.

[25] B. Sarkar, B. Cornuelle, and W. A. Kuperman. Inversion of full wave data using sensitivity kernels. *in preparation.*

[26] G. S. Piperakis, E. K. Skarsoulis, and G. N. Makrakis. Rytov approximation of tomographic receptions in weakly range-dependent ocean environments. *J. Acoustic Soc. Am.*, 120:120–134, 2006.

[27] S. M. Kay. *Fundamentals of statistical signal processing - Estimation theory.* Prentice Hall, New Jersey, 1993, Ch. 10.

[28] R. Evans. *WAVE.* oalib.hlsresearch.com/Other.

# Chapter 4

# Temperature Profile Estimation using Thermistor Chain Data

This chapter demonstrates an iterative inversion scheme that inverts thermistor chain data for a reference high-resolution temperature profile. Temperature fluctuations that are observed on a thermistor chain array are assumed to be caused by the displacement of water masses from different depths, whose underlying temperature profile is unknown[1]. Given a sufficient overlap of temperature time-series between successive thermistor chain elements, it is shown that the underlying temperature profile can be extracted, along with the displacement time-series that resulted in the measured thermistor time-series. Several test cases are demonstrated, starting with a piecewise linear profile with identical displacements at each observation depth. A measured CTD profile is then used, along with a temperature time-series generated using a linear internal wave model. Finally, the algorithm is demonstrated on a time-series measured during the course of making environmental measurements as part of the Focused Acoustic Fields experiment in 2006.

## 4.1   Introduction

Temperature fluctuations observed on a thermistor chain array are a valuable tool to measure and understand an ocean environment. Temperature observa-

tions can be easily converted to sound speed estimates. An understanding of sound speed fluctuations is of vital interest in acoustic propagation modeling[2], in order to be able to accurately predict the acoustic field in a waveguide. A thermistor chain deploys relatively easily, and can provide a time- and depth-scale for temperature observations. In shallow water environments, their utility is enhanced due to their ability to span almost the entire water column. This property is especially useful in studying internal waves in shallow water.

Internal waves cause displacements of water parcels having different temperatures, resulting in a temperature time-series[3, 4]. It is possible to directly relate temperature and displacement, given a time and depth temperature observations, along with a reference temperature profile. Fig. 4.1 shows an example of a reference temperature profile, whose displacement results in a temperature time-series. This reference temperature profile can be difficult to measure. Thermistor chain elements are often widely spaced (1-10 m apart) making it impossible to obtain a high-resolution temperature estimate in depth. Besides, even if a high-resolution CTD (conductivity-temperature-depth) measurement were made at the same location as the thermistor chain, it will simply be one realization of a fluctuating temperature profile. Thus, there is a need for a method of estimating the background temperature profile, the repeated displacement of which results in the observations. A typical temperature profile, while often monotonic, is non-linear, resulting in a non-linear mapping of temperature to displacement, and vice-versa. Thus, in order to invert the temperature time-series for a reference temperature profile, iterative methods are an attractive option. The thermistor chain, in such an application, can be seen as a 'synthetic aperture' array, which samples a repeatedly displaced temperature profile.

It has been observed by Pinkel[5] that displacements can often be described by a Gaussian distribution. Given a reference profile, temperatures observed at a certain depth will half as often be above the reference profile at that depth, as below it. Thus the median of temperature observations is very close to the true reference, as shown by Pinkel in coastal waters.

This paper demonstrates once such iterative method, based on the Gauss-
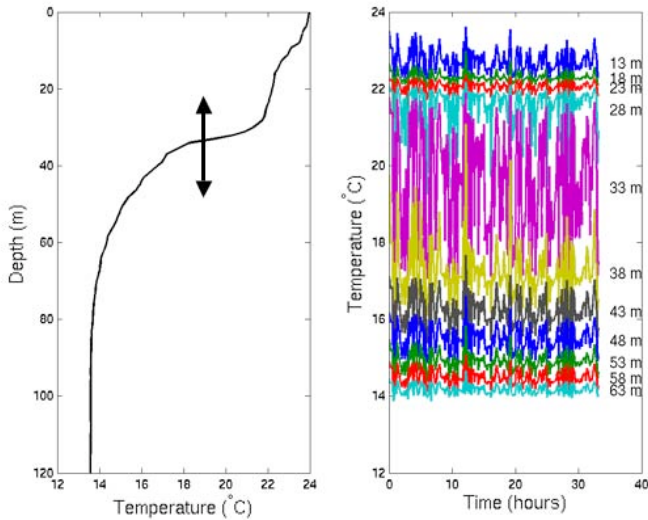
Figure 4.1: Illustration of the principle underlying the inversion scheme. Displacement of the profile on the left-hand panel results in the time-series measured in the right-hand panel

Newton method[6, 7], that performs the inversion. The method is described in more detail in the next section. Having described the method, Sec 3 demonstrates the iterative inversion algorithm using several simulation test cases. The first set of test cases have a known reference temperature profile that can be compared with the estimate to judge the validity of the method. A simple test case is that of a piecewise linear temperature profile with uniform displacement depths at several observation points. Next, a measured CTD profile is used, again with uniform displacements. Finally, displacements are modeled using a linear internal wave model, and the method is tested. Section 4 applies the inversion method to a measured set of observations, made during the course of an underwater acoustics experiment, Focused Acoustic Fields 2006 (FAF06). Brief details of the experiment are provided, with more information available in Song et. al. [8]. While the analysis in previous chapters utilized environmental and acoustic measurements made during FAF05, the thermistor chain elements were spaced too far apart in depth, and sampled too sparsely in time for the estimation method used in this chapter to be effective. Sec. 5 concludes the chapter and points to improvements

that can be made.

## 4.2   Method

This section explains the iterative technique based on the Gauss-Newton method that is used to invert the temperature observations to yield an estimate of the background temperature profile.

The basic principle behind the inversion scheme is that the temperature observations are caused by displacements of the reference profile. Thus, each thermistor chain element measures the temperatures of water parcels associated with water depths above and below. If between two successive thermistor elements, all water depths between the two are measured (the time-series is long enough), then it is possible to unscramble the time-series to yield an estimate of the true profile at the depths spanned by the thermistor chain.

Before delving into the method, a simple observation is in order that yields insight into the validity of the inversion. If there are $Nz_{obs}$ observations depths, each with a $Nt_{obs}$ point long time-series, then the number of known parameters is $Nz_{obs} \times Nt_{obs}$. Let the unknown true profile be determined at $Nz_t$ depths. It is assumed that temperature observations are caused by displacements of the water column at $Nz_d$ depths, at $Nt_d$ points in time. If $(Nz_d \times Nt_d + Nz_t) \leq (Nz_{obs} \times Nt_{obs})$, then the number of unknowns is less than the number of knowns, and the inversion has a unique solution. This situation can be expected when variations in displacements have a depth- and/or time-scale greater than that of temperature variations. For example, while temperature fluctuations might have a decorrelation scale of 1-5 m, that of displacement fluctuations might be 10-20 m. This assumption is used in the test cases involving a uniform displacement, and shown to be true for the test case using the internal wave model. The internal wave model has been tuned to have similar statistics as the temperature observations in FAF06, and hence the same assumption about displacement depth-scales is used in Sec. 4.

The iterative method is now discussed. Given a set of temperature observa-

tions $T_{obs}(z, t)$, a starting estimate for the reference profile $T(z)$ is made. Following Pinkel[5],the starting estimate is chosen to be the median of $T_{obs}(z, t)$, interpolated at $z_t$ depths. An estimate of the displacement field $z_{obs}(T)$ can then be made using $T_{obs}(z, t)$ and the $T(z)$ estimate. As mentioned previously, the displacement field is assumed to vary on a depth scale greater than $z_{obs}$, and hence needs to be mapped to $z_d$ depths, with $Nz_d \leq Nz_{obs}$. A displacement increment field $dz_d(z, t)$ is then computed as a time-difference, along with a $T(z)$ increment field $dT(z)$ referenced to the value of $T(z)$ at the bottom-most depth. The vectorized increment field is then stored as the vector $\mathbf{m}$, ordered as the displacement increment field, followed by the temperature profile increment field.

$$\mathbf{m} = \begin{pmatrix} vec\{\mathbf{dz_d}\} \\ \mathbf{dT} \end{pmatrix} \tag{4.1}$$

The vector $\mathbf{m}$ can be used to resynthesize a temperature time-series. The algorithm then consists of successively incrementing $\mathbf{m}$ such that the least-squares fit between the temperature field produced by each iteration of $\mathbf{m}$ and the observed temperature field is minimized.

Let the function that maps displacement and temperature increments to a temperature time-series $T_{est}(z, t)$ be denoted by $\mathbf{F(m)}$. Thus, the relation that expresses the difference between the estimated time-series and the observations, $\Delta T(z, t)$, and the increment to $\mathbf{m}$ ($\hat{\mathbf{m}}$) that is required to minimize the difference can be expressed as,

$$\begin{aligned} \mathbf{\Delta T} &= \frac{\mathbf{dF}}{\mathbf{dm}}\hat{\mathbf{m}} \\ &= \mathbf{G}\hat{\mathbf{m}} \end{aligned} \tag{4.2}$$

where $\mathbf{G}$ can be recognized as the Jacobian of $\mathbf{F}$. The increment $\hat{\mathbf{m}}$ can then be calculated as

$$\hat{\mathbf{m}} = (\mathbf{G}^H\mathbf{G} + \lambda\mathbf{I})^{-1}\mathbf{G}\mathbf{\Delta T} \tag{4.3}$$

where $(\cdot)^H$ is the conjugate transpose, or Hermitian. $\hat{\mathbf{m}}$ is calculated iteratively, where for each iteration, $\mathbf{G}$ is computed by incrementing each displacement and $T(z)$ point, and storing the resulting time-series caused by an individual increment.

Thus $\mathbf{G}$ is a $Nz_{obs} \times Nt_{obs} \times N_{par}$ array, where $N_{par} = Nz_d \times Nt_d$. $\mathbf{G}$ has been stacked to produce a two-dimensional array prior to the inversion in eq. 4.3. The new estimate for displacement and temperature increments is then calculated as

$$\mathbf{m_{new}} = \mathbf{m} + \mathbf{\hat{m}} \tag{4.4}$$

The new increment field now allows for the next iteration. In the test cases described, 5-15 iterations are typically sufficient to converge to a solution.

Various metrics and cost functions are computed during the inversion to gauge the quality of the estimation for the current iteration. These are described in the following section when describing the test cases.

## 4.3    Test case - Simulation

This section describes various test cases in order to demonstrate the inversion procedure. Test cases are generated by first starting with a known temperature profile. Known displacements are then generated either as random displacements or using an internal wave model, at the various sensor depths in the water column. These displacements, together with the temperature profile, are used to generate the temperature observations that will then be inverted. Although the test cases are ordered in an increasing order of complexity of temperature and displacement profiles, no explicit assumptions are made during the inversion that indicate a prior knowledge of the complexity, or lack thereof.

The water depth in all cases is chosen to be 121 m, with 11 sensors placed between 13 m to 63 m (5 m apart). These settings are chosen based on their being identical to those used in the FAF05 experiment.

In order to motivate the discussion, all plots are only shown for first test case. For all the others, only those plots which show unique case-sensitive behavior are shown. This also applies to the next section, where experimental observations are used.

### 4.3.1 Piecewise linear temperature profile with uniform displacements

The first test case deals with a piecewise linear temperature with uniform displacements. Displacements at any depth have a Gaussian distribution, with a mean displacement of 0 m, and a standard deviation of 2 m. For any given time, displacements at all depths are equal. Displacements are uncorrelated in time, and sampled every 10 minutes. Fig. 4.2 shows the temperature profile and displacement time-series used to generate the temperature observations (Fig. 4.3).

Due to identical displacements at all depths, the displacement scale in depth is large, and even just 2 displacement points ($Nz_d = 2$) should be sufficient to estimate the profile. The depths at which the displacement is estimated are chosen to be 5 m and 95 m. The high resolution temperature profile is estimated at 1 m steps, and 100 points in the time-series for temperature observations are considered.
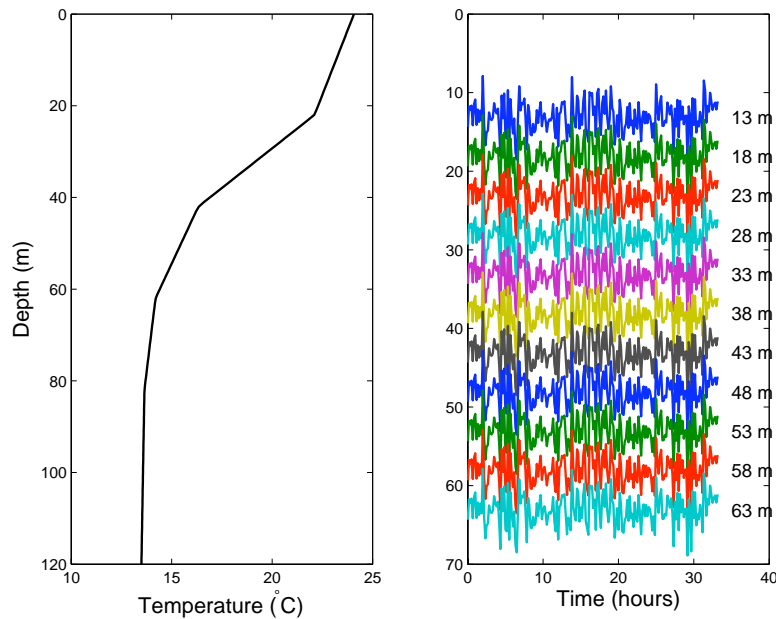


Figure 4.2: Known piecewise linear temperature profile and uniform displacement time-series. The numbers on the righthand panel indicate sensor depths. Displacements at any sensor depth are uncorrelated Gaussian random variables. Displacements at any give time are equal at all sensor depths.
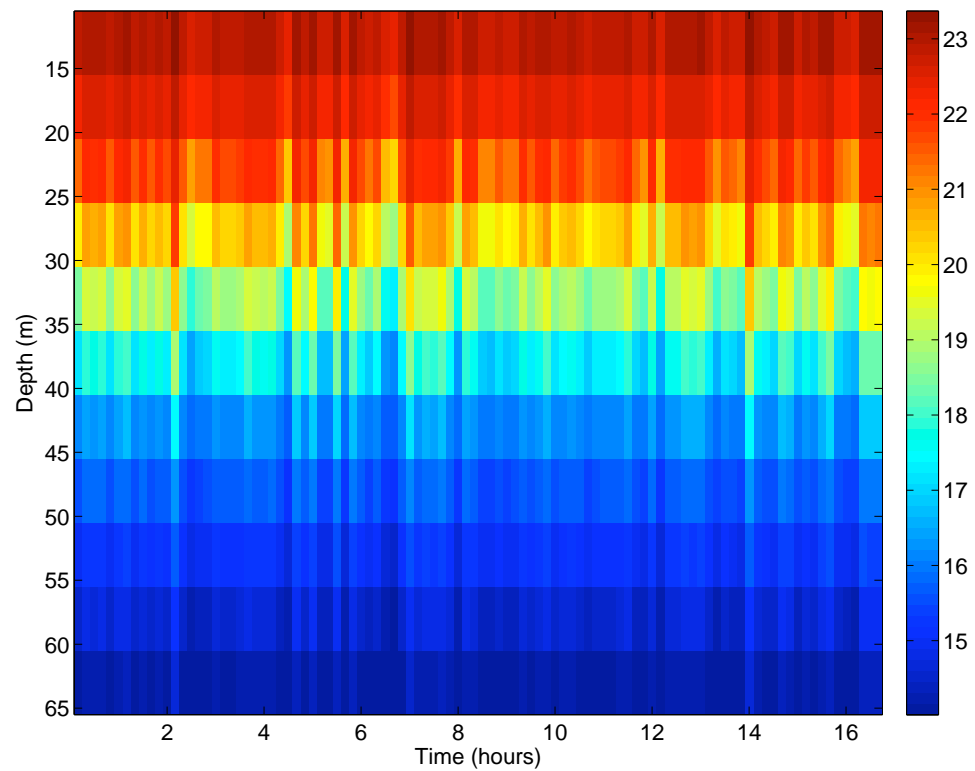
Figure 4.3: Observed temperature profile ($^\circ C$) for the test case with a piecewise linear profile and uniform displacements.

The starting profile estimate (Fig. 4.4) is chosen to be the temporal mean of the observations, which is then linearly extrapolated to $Nz_t$ depths at which the profile estimate is required.
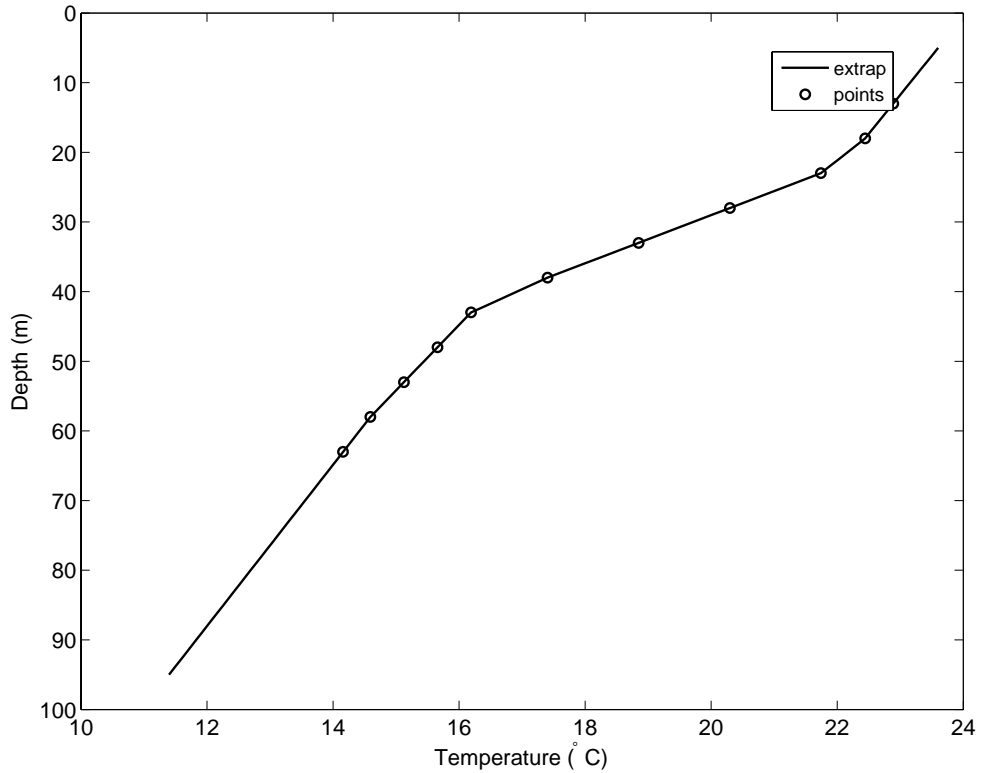


Figure 4.4: First T(z) guess extrapolated to $Nz_t$ depths. Circles show the mean of observations at each depth, and the blue line shows the extrapolation to $Nz_t$ depths.

This profile estimate is then used along with the temperature observations $T_{obs}(z,t)$ to get an estimate for the displacement time-series $z_{obs}(T,t)$, shown in Fig. 4.5. This figure, when compared to the righthand panel of Fig. 4.2 reveals differences in the displacement estimate requiring the use of the inversion.
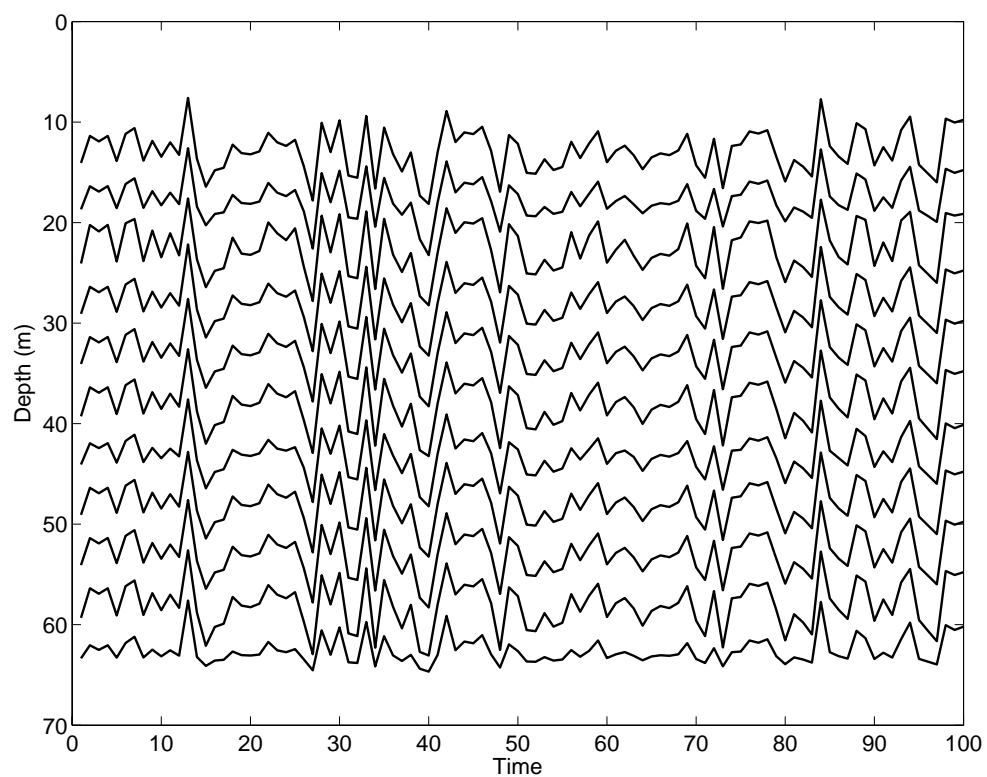
Figure 4.5: First estimate for displacement depths.

Another measure of the error in displacement estimates can be seen in Fig. 4.6 which is essentially the mean and r.m.s of Fig. 4.5. For this particular test case, the mean of displacements was 0 m, and the r.m.s 2 m, at all depths. Deviations from this are a sign of an incorrect estimate.
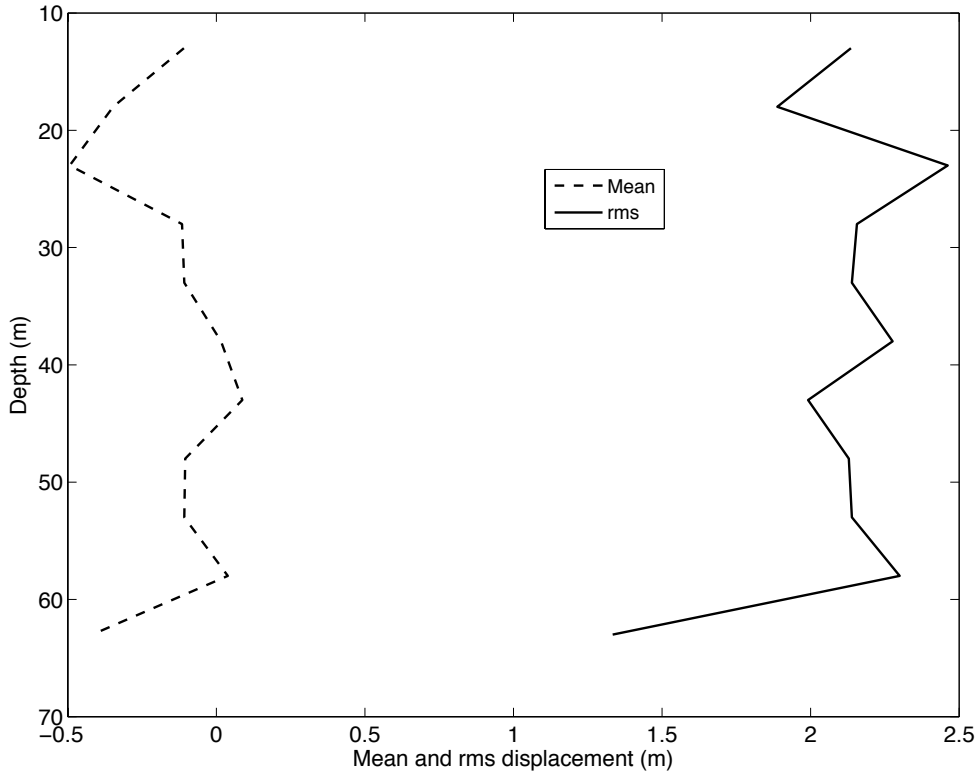


Figure 4.6: Mean (dashed) and r.m.s (solid) for estimated displacement depths. For this test case, if the estimates were perfect, the mean should be 0, and r.m.s should be 2.

Fig. 4.7 shows the depthwise correlation, again obtained using the displacement estimate. This figure is yet another indication of the current error in estimation. Due to the uniform nature of the synthetic displacements, the figure should have indicated a full correlation at all depths. However, this not so, especially at the fringes, where observations are not available. As a result, profile estimates cannot be expected at these depths.

Of course, displacement time-series are only available for synthetic test cases. In more realistic cases, an idea of the errors in displacement estimates can
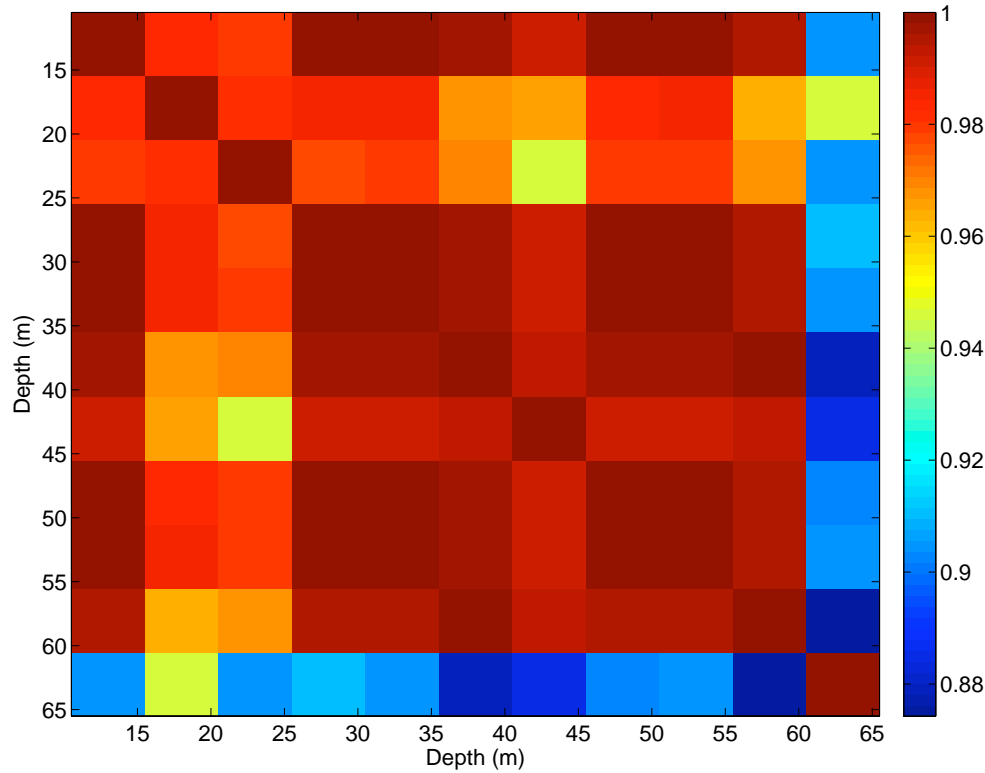
Figure 4.7: Depth-depth correlation coefficient for displacement estimate. For this test case, if the estimate were perfect, it would be 1 everywhere.

only be obtained by once again mapping the displacement estimate to a temperature time-series (using the initial profile estimate), and comparing that with the observations. Such a comparison is shown in Fig. 4.8 where the observations have been subtracted out to show the error in the estimate.
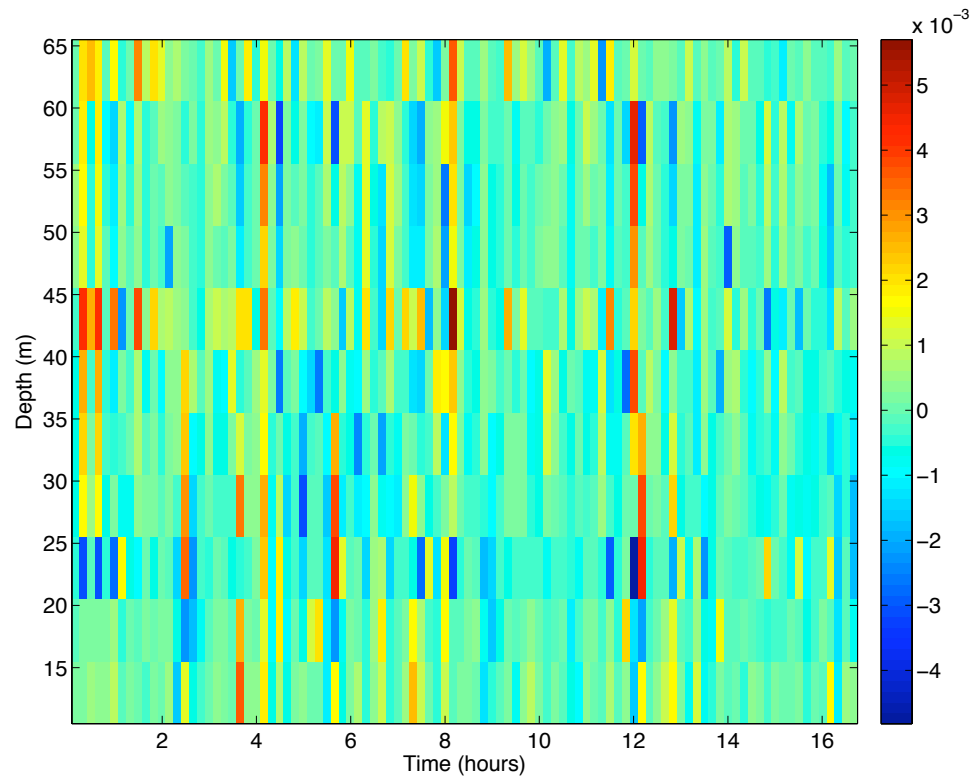
Figure 4.8: Error ($^{\circ}C$) in estimate of temperature observations. Displacements are computed using the T(z) estimate, and these displacements are used to compute the estimated time series. The error between the estimate and observations is plotted. If all zero, then the estimate is perfect.

Figs. 4.9 and 4.11 show the prior and posterior parameter uncertainities for displacement and temperature profile increments. The priors are fixed before hand, and for this case are 1 m for the displacements and scales with depth for the temperature. These are the parameters whose increments are determined after the inversion. If a solution is being converged upon, these covariances get smaller with each iteration, as seen in Fig. 4.11. Once again, higher values below 70 m reflect a lack of observations at those depths, due to which a correct estimate will never be arrived at below 70 m.
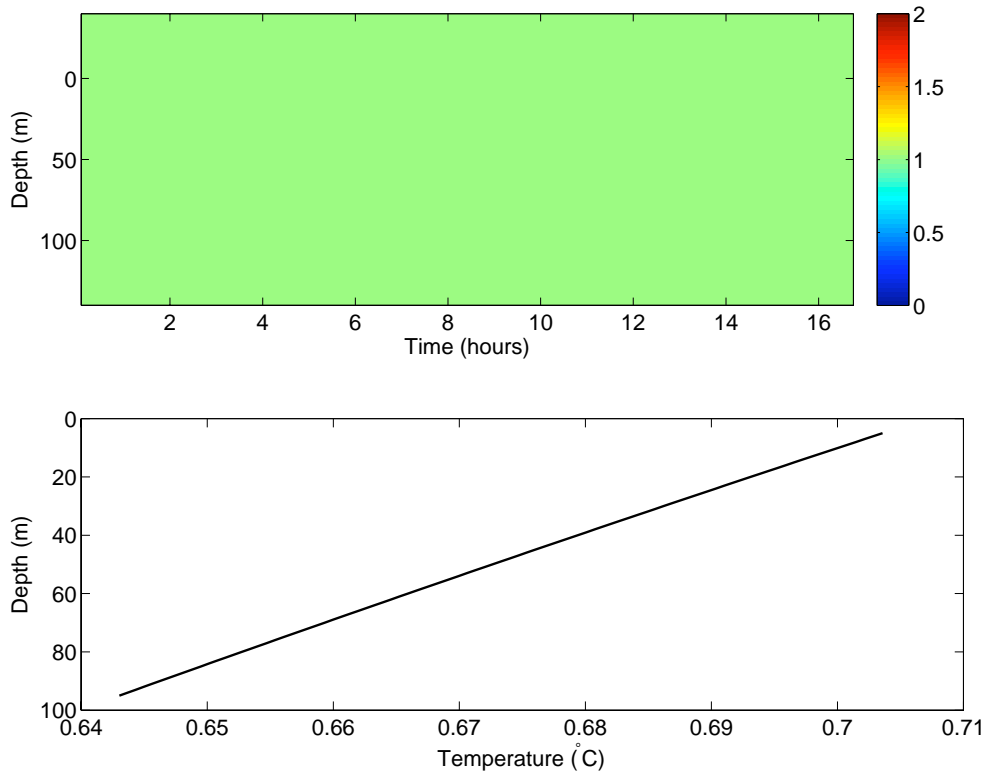


Figure 4.9: Prior displacement (upper panel) and temperature increment (lower panel) rms. This is first set by the user, and has the form shown.

The next figure (Fig. 4.10) for this test case shows the profile estimate compared to the true (known) profile and the starting estimate. Also shown is a plot of the error with respect to the true profile. It is seen that the inversion works well for depths at which observations are available. Beyond these depths, the estimate is simply extrapolated, which works at the surface, but not the bottom.

A gauge of the quality of the estimate may be seen in Fig. 4.11 where the lack of observations below 63 m result in poor estimation quality. However, the final estimate is seen to be accurate until 70 m which marks the lowest depth from which water parcels are being advected to the sensor array. This observation also points to the 'synthetic aperture' -like nature of the estimation.
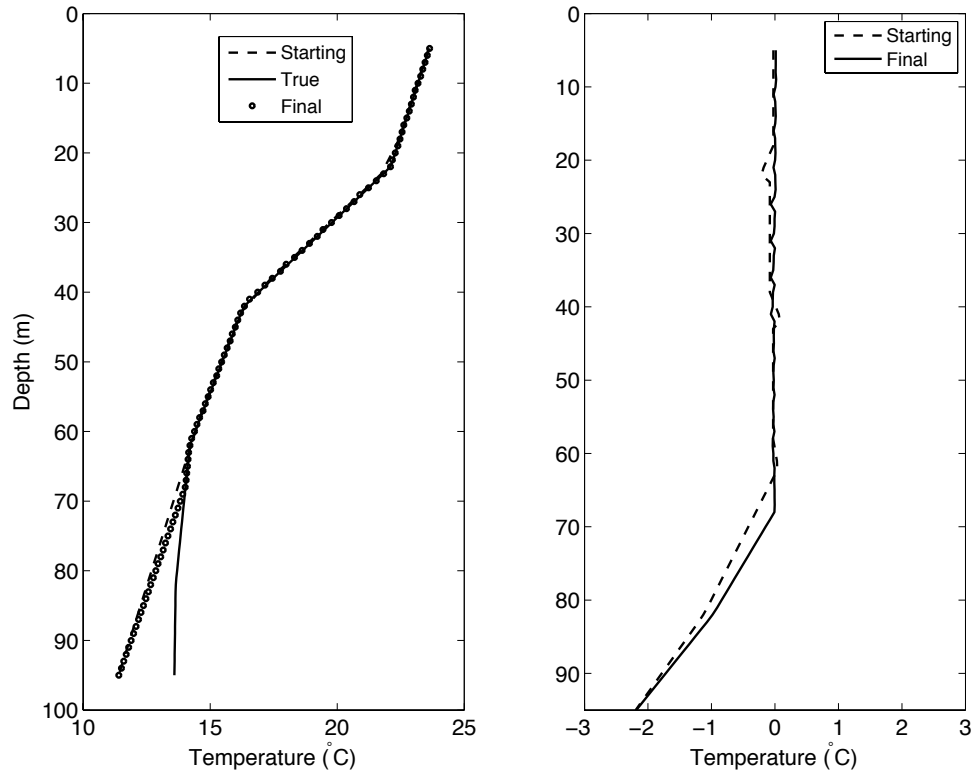


Figure 4.10: Profile estimates and estimation error for the test case with a piecewise linear profile and uniform displacements. The left-hand panel shows the starting estimate (dashed), final estimate (circles) and the true profile (solid). The right-hand panel shows the estimation error with respect to the true profile
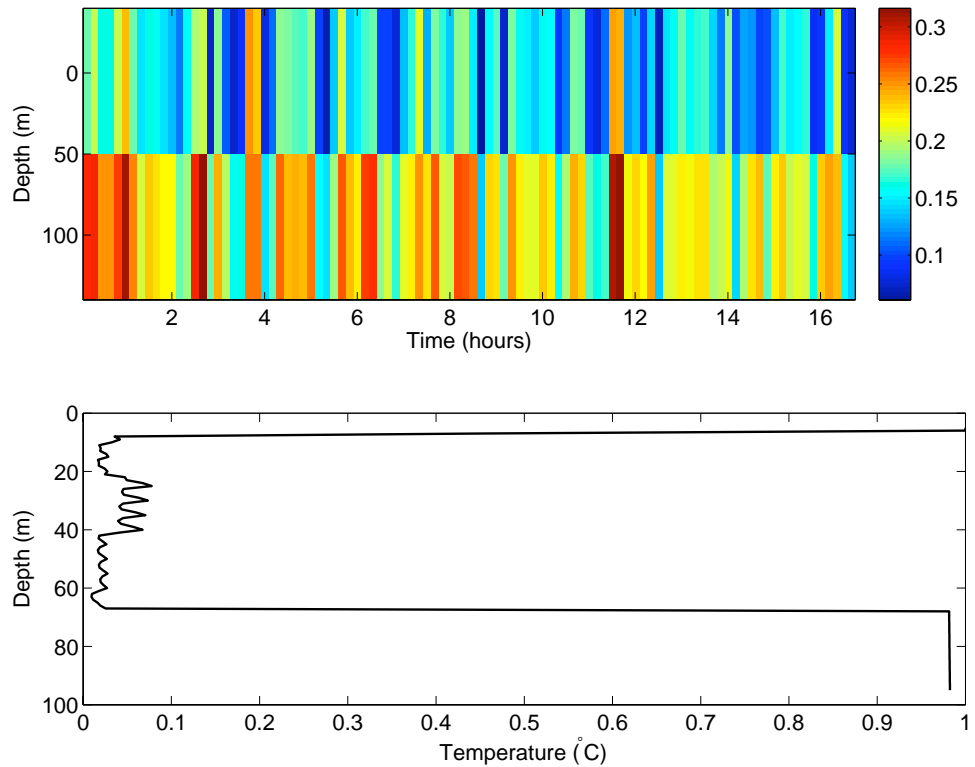
Figure 4.11: Posterior displacement increment rms (upper panel) and temperature increment rms (lower panel). Low values show a gradual convergence. If it were 0, then no further increments need be made. High values at the fringes indicate the absence of observations at those depths.

### 4.3.2  CTD profile with uniform displacements

This test case adds an additional level of complexity to the previous case by having a more realistic temperature profile, while still having uniform displacements, that need only be estimated at two depths (5 m and 95 m). The temperature profile shown in Fig. 4.12 has been obtained from a CTD cast made during the course of the FAF05 experiment. Temperature observations (Fig. 4.13) are generated via Gaussian random displacements with a mean displacement of 0 m and and standard deviation of 2 m. For a given time, displacements are identical at all depths. Displacements are uncorrelated in time and are 10 minutes apart. Depth steps for the temperature profile estimate are set to be 1 m, and is the same as the previous test case.
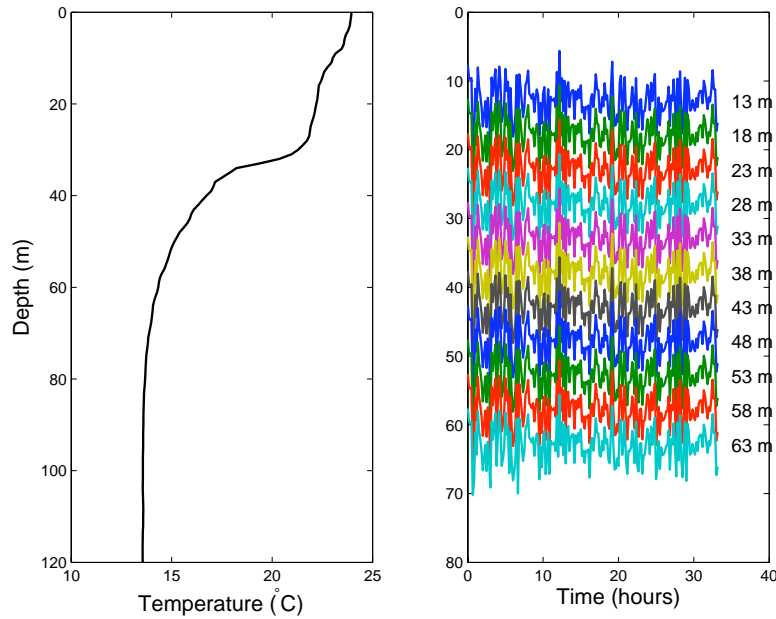


Figure 4.12: Known FAF05 CTD temperature profile and uniform displacement time-series. The numbers on the righthand panel indicate sensor depths. Displacements at any sensor depth are uncorrelated Gaussian random variables. Displacements at any give time are equal at all sensor depths.

Not all plots shown in the previous test case are shown for this test case, especially since the displacement time-series are almost the same.

The final temperature estimate can be seen in Fig. 4.14, along with an error
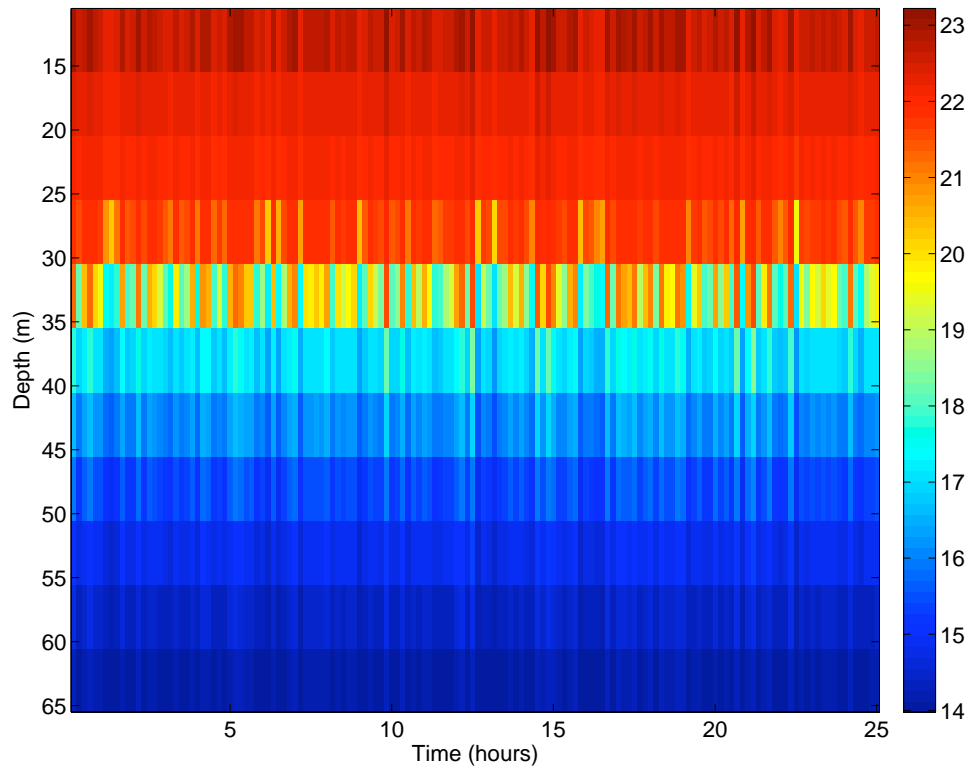
Figure 4.13: Observed temperature profile ($^\circ C$) for the test case with a FAF05 CTD profile and uniform displacements.

in the estimate. Once again, the estimation is seen to work well for this synthetic case.

Fig. 4.15 shows the uncertainty variance for displacement and temperature increments. A note should be made of the jump in uncertainty around 30 m. This can be attributed to the non-linearities that arise when the slope of $T(z)$ changes with depth. Displacements will be sensitive to the to the estimated temperature gradient at that depth. The displacement may not be right, in which case it samples the profile at the wrong depth, tries to correct the temperature at the wrong depth, and the iteration may not converge.
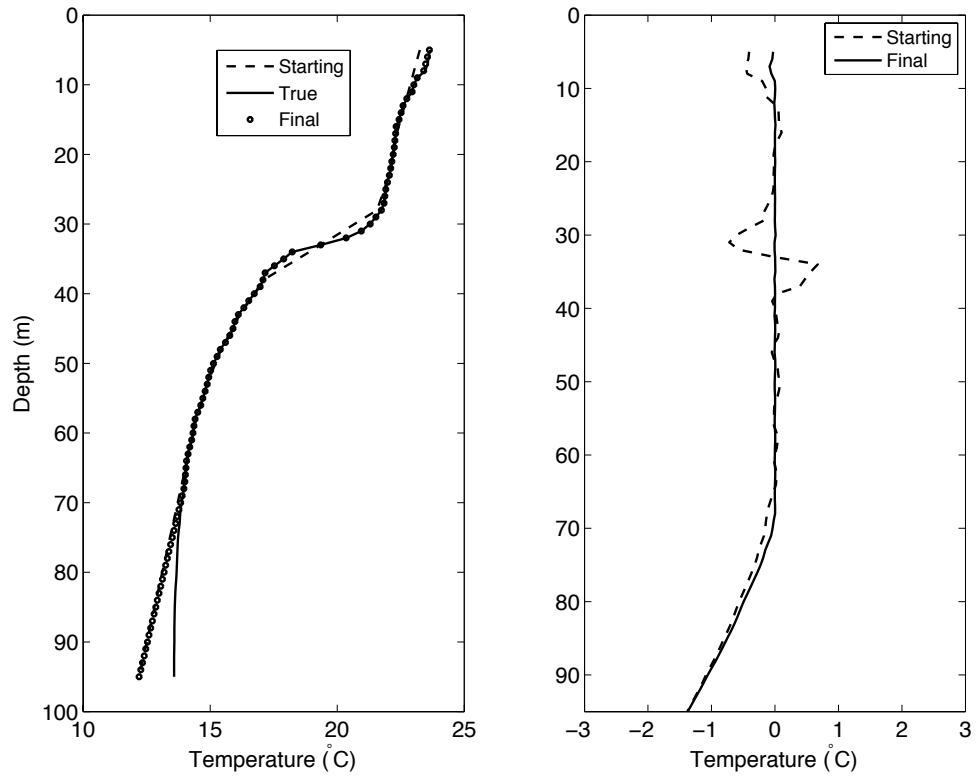
Figure 4.14: Profile estimates and estimation error for the test case with a FAF05 CTD profile and uniform displacements. The left-hand panel shows the starting estimate (dashed), final estimate (circles) and the true profile (solid). The right-hand panel shows the estimation error with respect to the true profile.
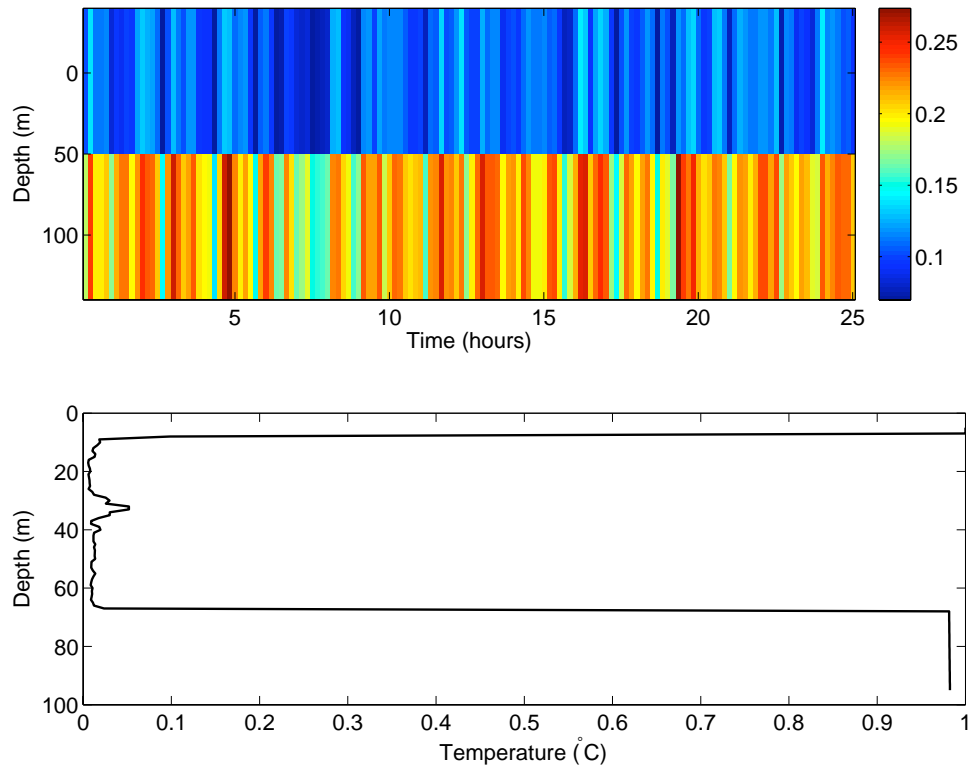
Figure 4.15: Posterior displacement increment rms (upper panel) and temperature increment rms (lower panel). Low values show a gradual convergence. If it were 0, then no further increments need be made. High values at the fringes indicate the absence of observations at those depths.

### 4.3.3 CTD profile with IW-induced displacements

The last test case involving synthetic data utilizes temperature observations that are obtained via an internal wave model. Brief details regarding the internal wave model are provided below, with further details available in Raghukumar et. al.[9].

The same CTD profile that was used in the previous test case is used to compute the buoyancy profile, which in turn is used to solve for the vertical modes and the dispersion relation for internal waves in the given environment. For a given mode number and wavenumber, the dispersion relation gives information as to the which frequencies the internal waves can exist. The buoyancy profile is also used to derive the internal wave spectrum which follows a power law and is a shallow water version of the Garret-Munk spectrum. Mode amplitudes are also chosen using the Garett-Munk model. All these ingredients are then combined as a Fourier superposition to give displacement time series for each sensor depth. Temperature observations can then be easily derived.

The true (known) temperature profile is assumed to stay constant throughout the entire observation interval. This assumption may not always be true in reality, in which case any single estimate made using the entire time-series may not be accurate.

Due to the higher level of complexity involved, the depth steps for estimating the high resolution temperature profile has been reduced to 0.5 m, and 150 points in the time-series are used for the inversion. Data are samples every 10 minutes so this corresponds to 25 hours of data.

Fig. 4.16 shows the CTD profile and displacement time-series used to derive the temperature observations (Fig. 4.17).
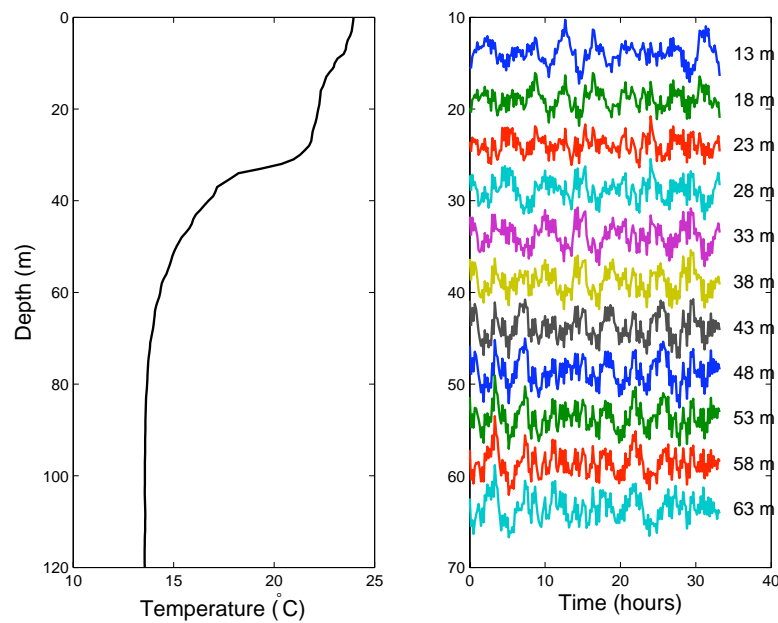
Figure 4.16: Known FAF05 CTD temperature profile and modeled internal wave displacement time-series. The numbers on the righthand panel indicate sensor depths.
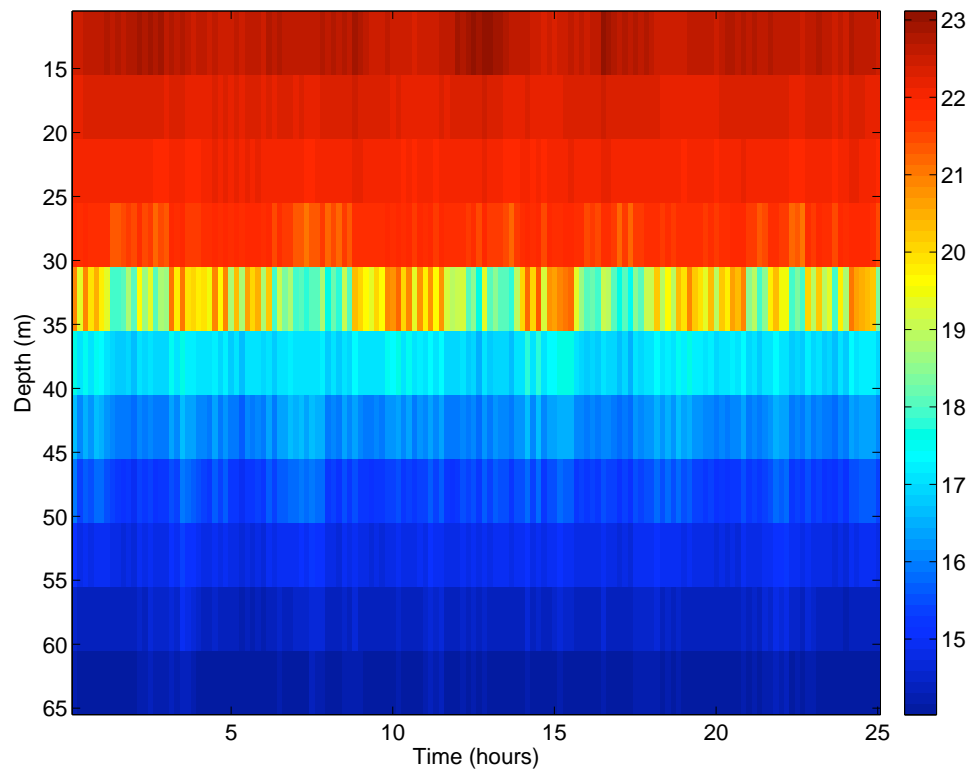
Figure 4.17: Observed temperature profile ($^{\circ}C$), for the test case involving a FAF05 CTD profile with modeled internal wave displacements.

Fig. 4.18 shows the depth-depth correlation coefficient using the initial displacement estimate. It should be recalled that the initial displacement estimate is made by first making an initial estimate for the temperature profile, which for this case was the mean of the observations linearly extrapolated to $Nz_t$ depths. There is significant difference in correlation structure compared to Fig. 4.7, due to the non-uniform nature of displacements for this test case. As a result, displacements have to be estimated at several depths, and not just 2 depths as was done in the previous test cases. Nine displacement depths are chosen, 10 m apart, from 5 m to 85 m. There is also the option to have custom displacement depths based on the depth correlation scale, with closer-spaced displacement depths near the thermocline where the correlation between depths is lowest. However, equally spaced displacement depths provided the best estimate for this case.
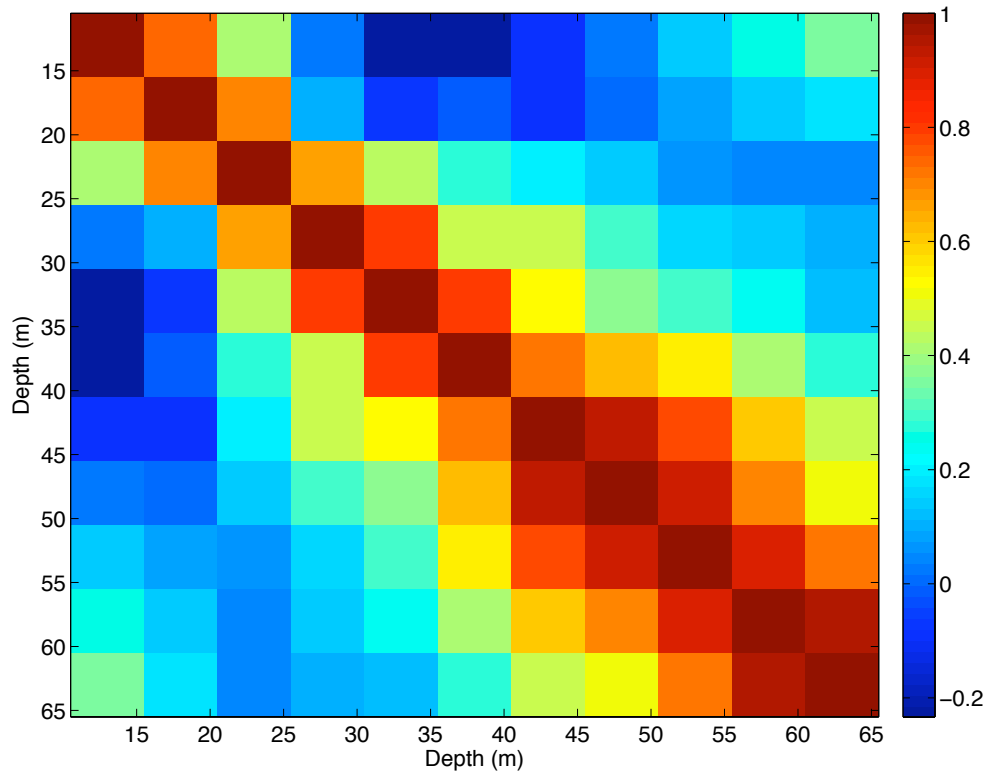


Figure 4.18: Depth-depth correlation coefficient for displacement estimate, for the test case involving a FAF05 CTD profile, with modeled internal wave displacements.

The next figure (Fig. 4.19) shows the temperature anomaly at the end of 15 iterations. This is the error between the estimated and actual temperature observations. Maximum error is seen around the thermocline, with the overall error level much higher compared to that in Fig. 4.8.
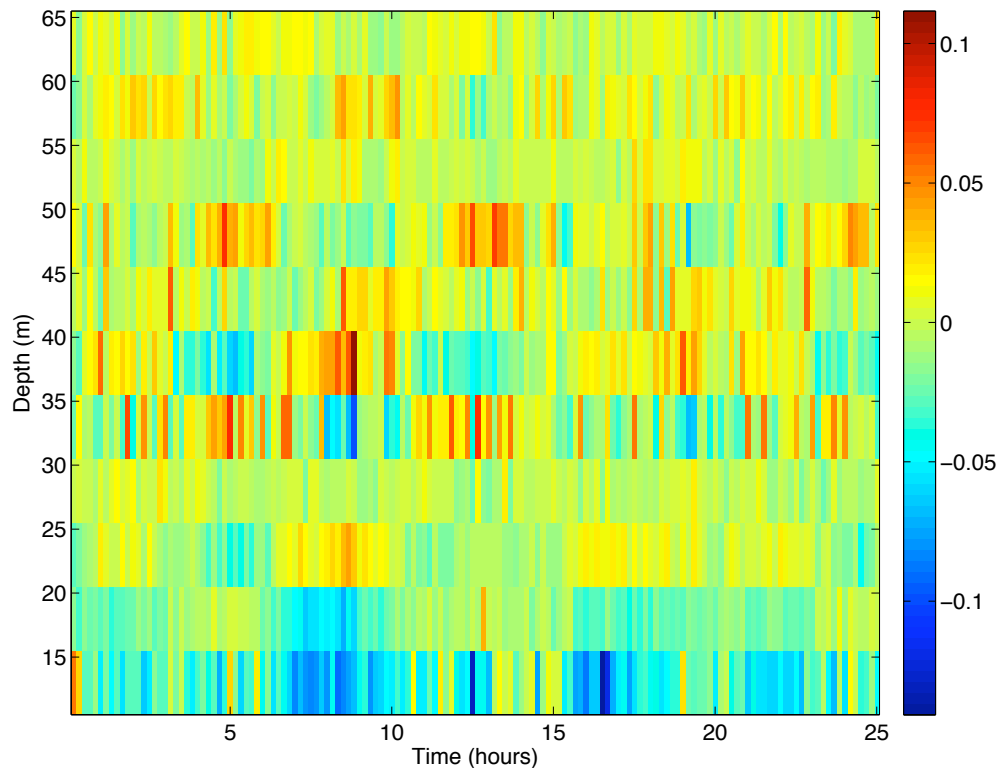


Figure 4.19: Error in first temperature estimate ($^{\circ}C$). Displacements are computed using the first guess for T(z), and these displacements are used to compute the estimated time series. The error between the estimate and observations is plotted. If all zero, then the estimate is perfect.

A jump in the uncertainty at 35 m can also be seen in the final temperature estimate in Fig. 4.20 where the profile estimate shows the largest error around 35 m. Depths above 13 m and below 65 m are not considered due to a lack of observations below these depths, indicating that no water parcels from these depths are being advected to nearby sensors.
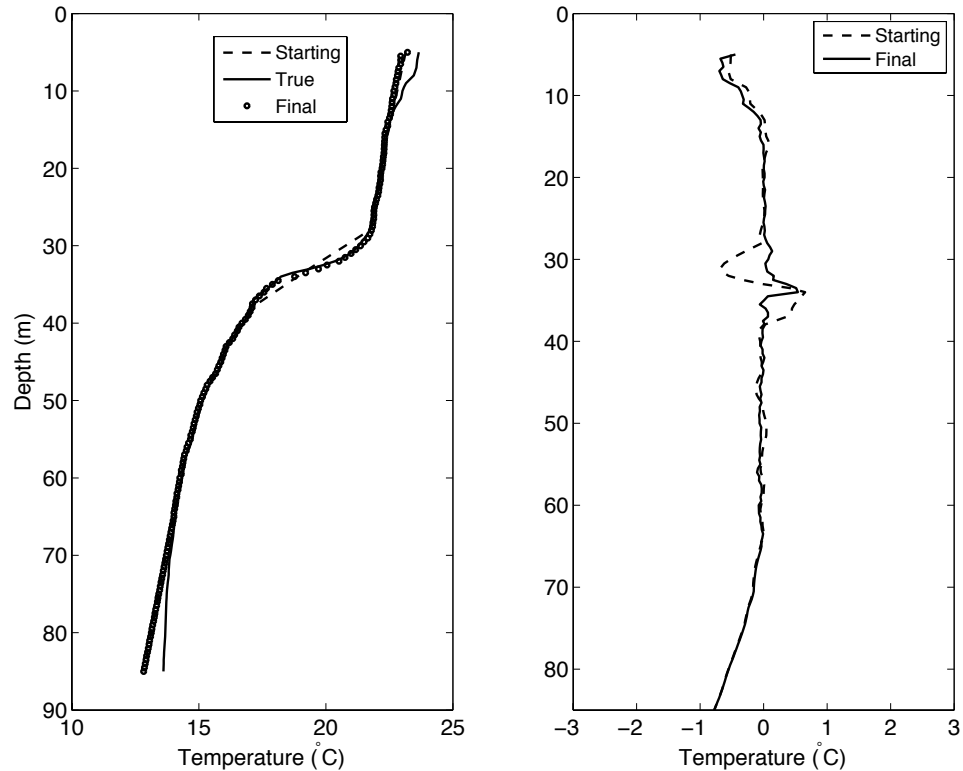


Figure 4.20: Profile estimates and estimation error for the test case with a FAF05 CTD profile and modeled internal wave displacements. The left-hand panel shows the starting estimate (dashed), final estimate (circles) and the true profile (solid). The right-hand panel shows the estimation error with respect to the true profile.

Fig. 4.21 shows the uncertainty variance for displacement and temperature increments. A much higher level of uncertainty is seen compared to Fig. 4.15, with the maximum occuring in the region of the thermocline, around 35 m.
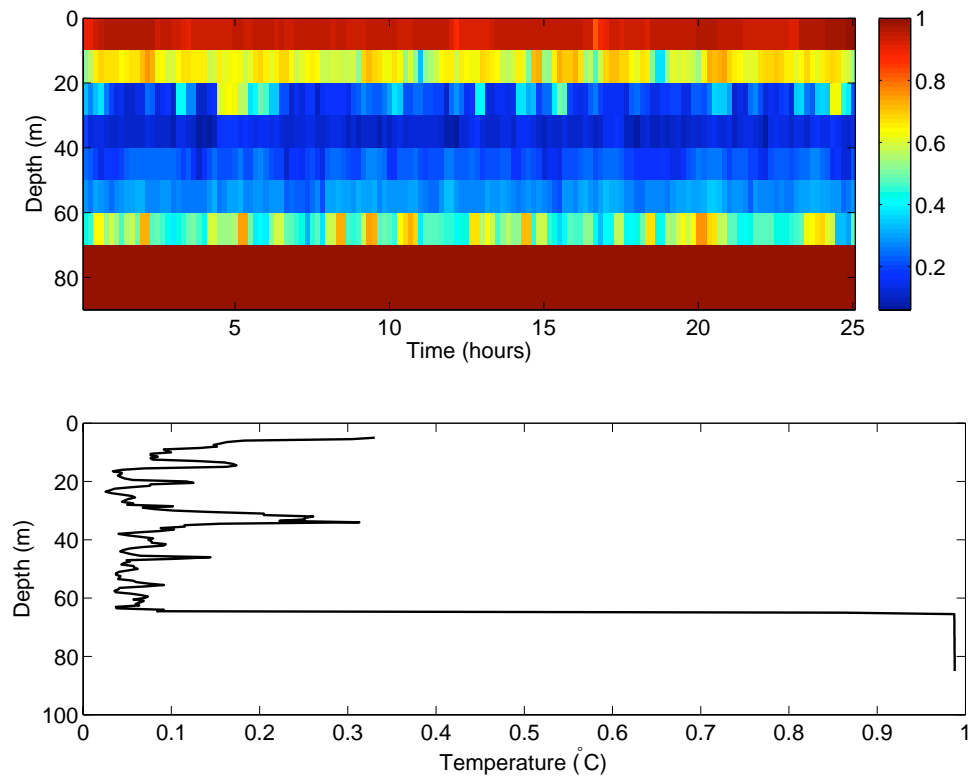
Figure 4.21: Posterior displacement increment rms (upper panel) and temperature increment rms (lower panel). Low values show a gradual convergence. If it were 0, then no further increments need be made. High values at the fringes indicate the absence of observations at those depths.

## 4.4   Inversion applied to FAF06 observations

This section demonstrates the ability of the inversion technique to estimate the reference temperature profile given a set of temperature observations gathered during the course of the FAF06 experiment.

A 16-element thermistor chain was deployed over a period of 17 days. In order to demonstrate the inversion, only 300 samples, or 50 minutes of data are used. The water depth was 121 m, and the sampling interval 10 seconds. The array spanned water depths from 10 m to 40 m. Fig. 4.22 shows the temperature observations over the period of interest.
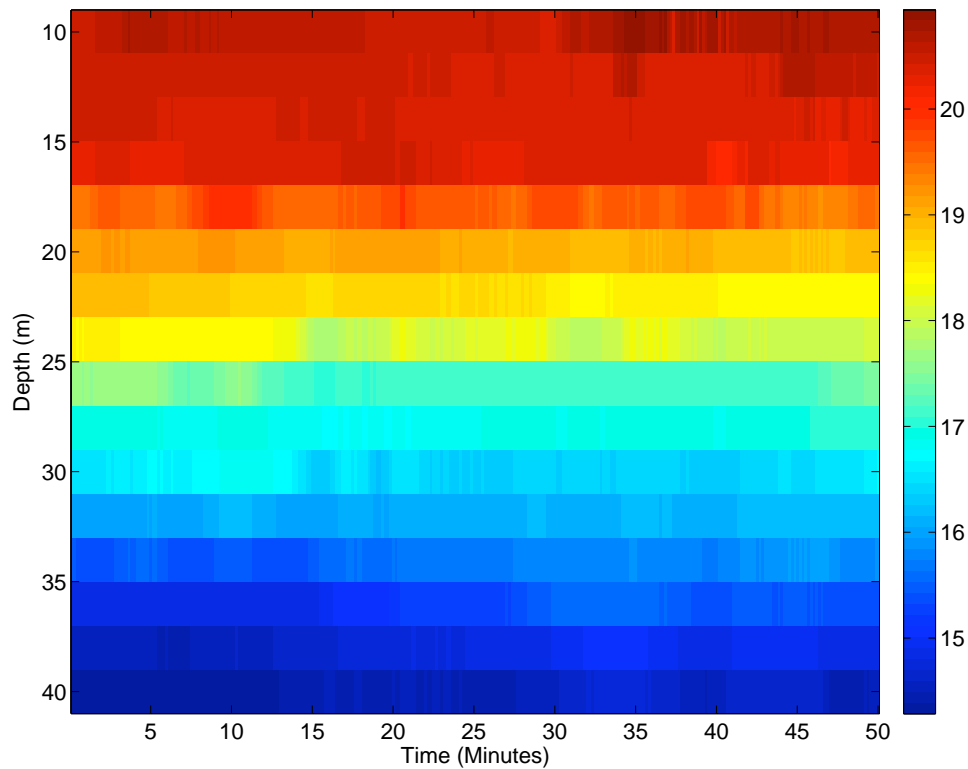


Figure 4.22: Observed temperature profile ($^{\circ}C$) for the FAF06 experiment.

Fig. 4.23 shows the displacement estimate computed using the median of temperature observations as a reference profile. The presence of high-frequency content in the displacement time-series is an indication of inaccuracies in the estimate. This figure, compared to Fig. 4.28 further illustrates this point.
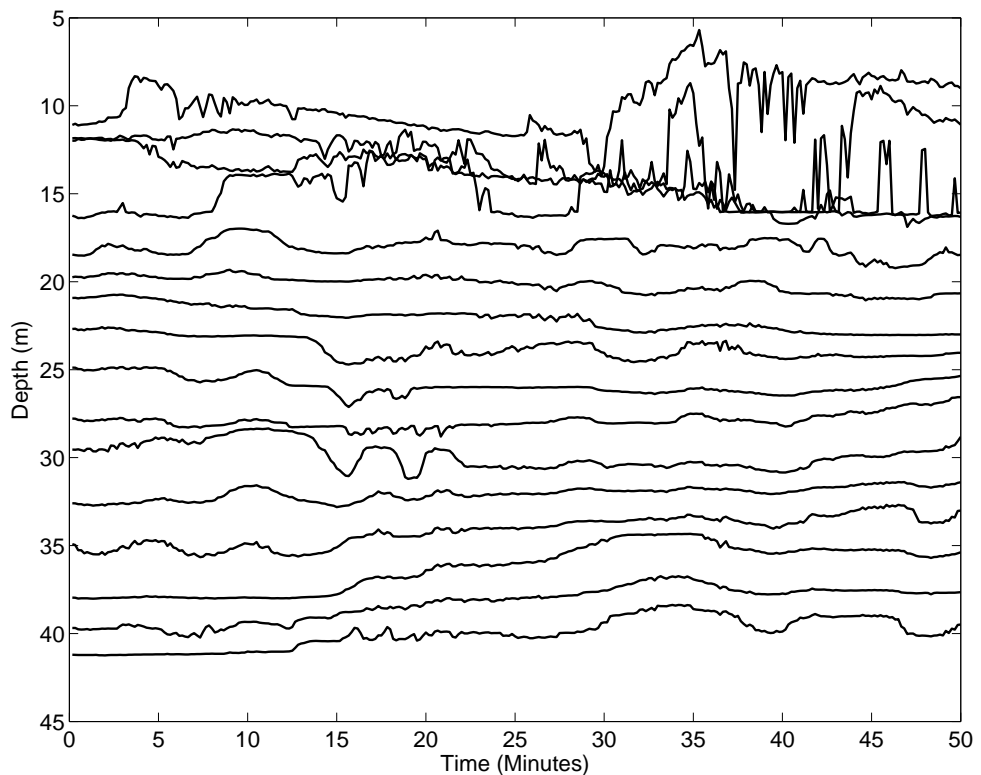
Figure 4.23: Displacement estimates computed using the median of temperature observations for the FAF06 experiment.

Fig. 4.18 shows the depth-depth correlation coefficient using the initial displacement estimate. The correlation between depths is even less than what is observed in Fig. 4.18. As a result, custom displacement depths are used where displacement estimates are made every 5 m between 5 m and 30 m, and then every 10 m between 40 m and 60 m.
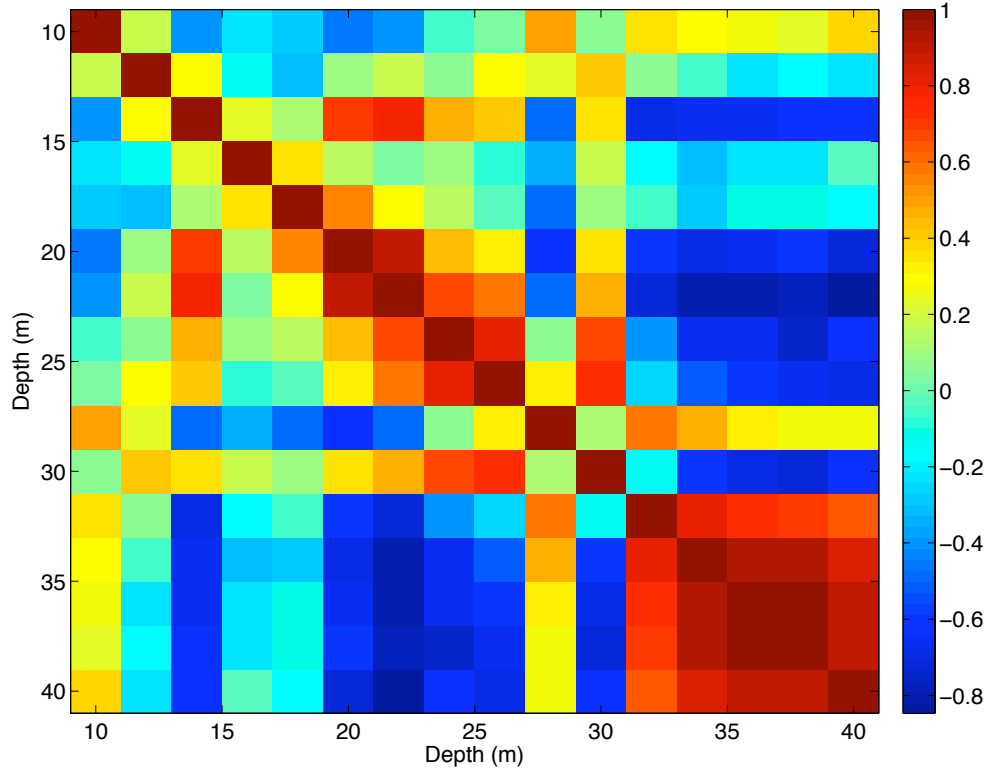


Figure 4.24: Depth-depth correlation coefficient for displacement estimate, for the FAF06 thermistor chain data.

Fig. 4.25 shows the temperature profile estimate after 6 iterations, along with the initial estimate. The estimation was seen to provide the lowest error after 6 iterations, after which the error was seen to increase again. This is possibly the result of the estimation process not quite finding a true minimum. If this were true, a global optimization method such as the use of a genetic algorithm may be required as a next step[10]. While a much higher level of resolution is seen in the final estimate, this figure by itself provides no information about the accuracy of the estimate. A note should be made of the steps that can be seen in the final

estimate. Since these occur in well-observed parts of the profile, a lack of overlap in the time-series cannot be an issue. Since the data are rather close to the water surface, heating of the surface is a likely candidate for alterations in the profile. A process such as this is not currently incorporated in the estimation model.
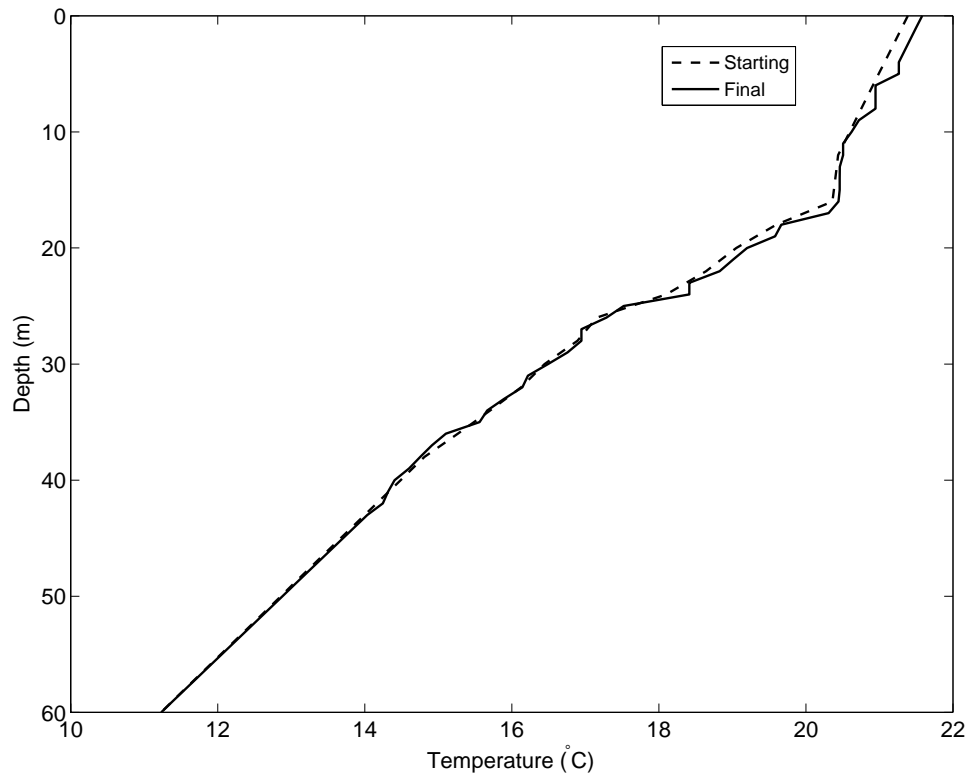


Figure 4.25: Starting (dashed) and final (solid) estimates for the FAF06 observations.

Fig. 4.26 shows the uncertainty variance for displacement and temperature increments. The displacement and temperature profile increments show that while the estimation method has been able to gradually converge to a solution between 20 m and 50 m, errors remain between 10 m to 20 m. This is also reflected in the step-like behavior in Fig. 4.25.

The next figure shows the spectra of displacements at a mean depth of 25 m, for displacements computed using the median of temperature observations (first estimate) and final temperature profile estimate. While not shown in the figure, the displacement spectra were observed to get increasingly narrow band
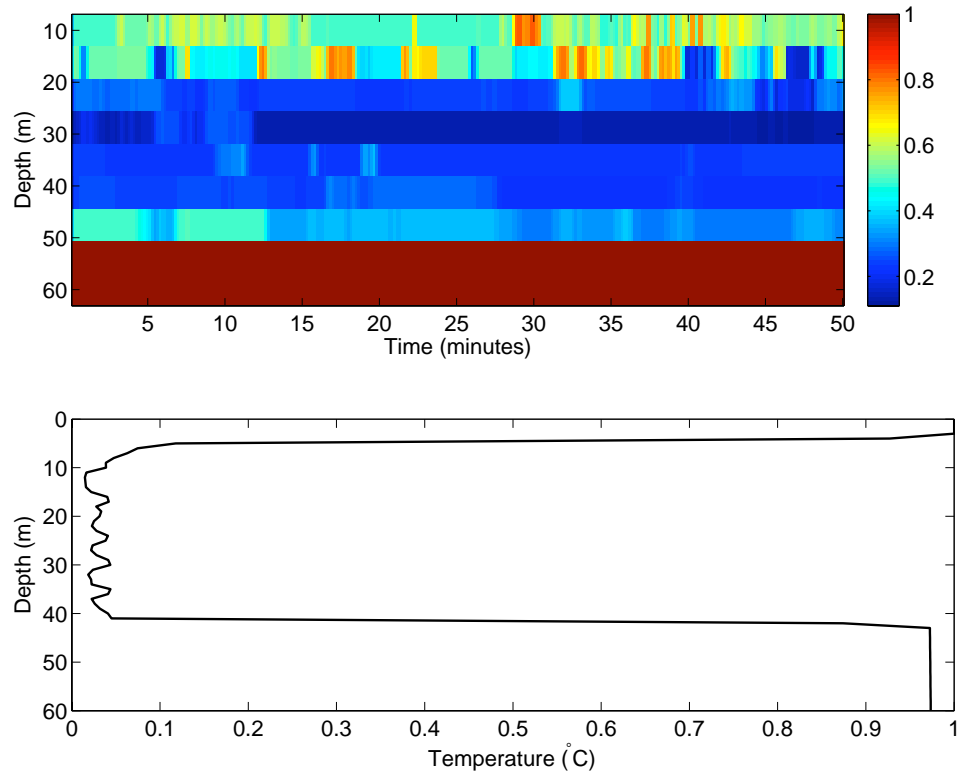
Figure 4.26: Posterior displacement (upper panel) and temperature increment (lower panel) rms. Low values show a gradual convergence. If it were 0, then no further increments need be made. High values at the fringes indicate the absence of observations at those depths.

over successive iterations. This is another indication that the iterative procedure is producing realistic displacement profiles since a narrowband spectra reflects a smooth displacement profile.

The final figure (Fig. 4.28) shows the modeled displacement time-series using the final estimate. A comparison with Fig. 4.23 shows a smoother displacement time-series, consistent with Fig. 4.27.
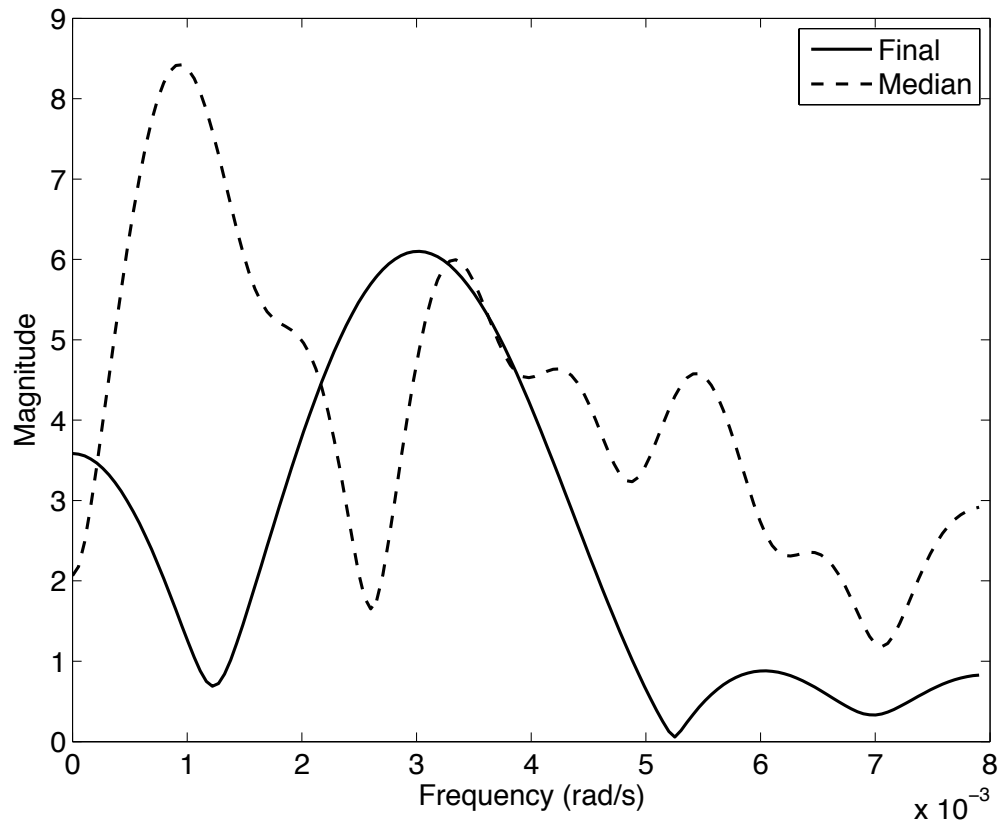
Figure 4.27: Spectrum of displacement estimates made at a mean depth of 25 m. The solid line shows the spectrum obtained using the median temperature profile of the observations in order to estimate displacements. The solid line shows the spectrum obtained using the final estimate of temperature profile of the observations in order to compute displacements. The harmonics present in the initial estimate are absent in the final estimate.s
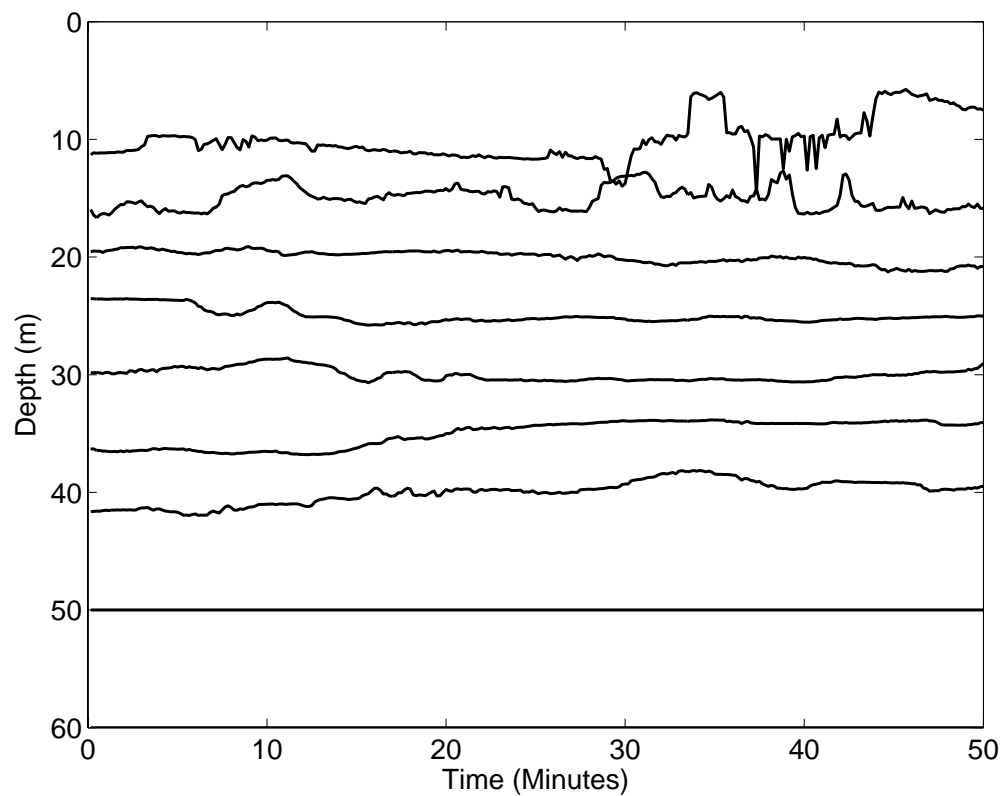
Figure 4.28: Displacement estimates computed using the final temperature profile estimate, for the FAF06 experiment.

## 4.5 Conclusions

This chapter demonstrated the use of an inversion technique that can be used to estimate a high-resolution background temperature profile, given a set of temperature observations. Temperature fluctuations are assumed to be caused by displacements that have a depth decorrelation scale much larger than that of observed temperature fluctuations. This assumption gives rise to a well-posed inversion problem that is then iteratively solved using the Gauss-Newton method.

Several test cases are demonstrated, with displacements ranging from uniform to those derived using an internal wave model. The internal wave model is matched to a set of experimental temperature observations, on which the inversion is finally performed. Similar results are seen for the internal wave model and the experimental observations, which shows promise for this method of inversion.

Some of the limitations of this method are that the temperature profile is required to be monotonic. In addition, sensors should be placed close enough that there is an overlap of displacement depths between sensors. While the method seems to work with non-linear profiles, severe non-linearities such as regions of rapidly changing slopes, still pose a bit of a challenge.

## 4.6 Acknowledgements

The text in this chapter is in full a reprint of the material as it appears in Kaustubha Raghukumar, Bruce Cornuelle, William Hodgkiss, William Kuperman, "Temperature profile estimation using thermistor chain data", in preparation, 2009.

# Bibliography

[1] C. Garret and O. M. Phillips. On spectra observed in an undulating layered medium. *Journal of Physical Oceanography*, 1:1–6, 1971.

[2] S. Flatte, R. Dashen, W. Munk, K. Watson, and F. Zachariasen. *Sound transmission through a fluctuating ocean.* Cambridge University Press, Cambridge, 1979.

[3] C. Garret and W. Munk. Space-time scales of internal waves. *Geophysical Fluid Dynamics*, 2:225–264, 1972.

[4] R. S. McKean. Temperature spectra in the deep ocean off hawaii. *Journal of Physical Oceanography*, 4:191–199, 1974.

[5] R. Pinkel. *Private communication*, 2009.

[6] R. L. Parker. *Geophysical inverse theory.* Princeton University Press, Princeton, 1994.

[7] P. Gerstoft. Inversion of seismo-acoustic data using genetic algorithms and a posteriori probability distributions,. *J. Acoustic Soc. Am.*, 95:770–782, 1994.

[8] H. C. Song, P. Roux, W. S. Hodgkiss, W. A. Kuperman, T. Akal, and M. Stevenson. Multiple-input/multiple-output coherent time reversal communications in a shallow water. *IEEE J. Oceanic Engineering*, accepted for publication.

[9] K. Raghukumar, Bruce D. Cornuelle, William S. Hodgkiss, and William A. Kuperman. Experimental demonstration of pressure sensitivity kernels. *J. Acoustic Soc. Am.*, 2009, to be submitted.

[10] P. Gerstoft. Inversion of acoustic data using a combination of genetic algorithms and the gauss-newton approach,. *J. Acoustic Soc. Am.*, 97:2181–2191, 1995.

# Chapter 5

# Conclusions and Future Work

In this dissertation, pressure sensitivity kernels were applied to time-reversal acoustics, in an effort to understand and quantify the observed stability of the time-reversal focal spot. The time-reversal focal spot has been previously observed to produce a focal spot over an hour after the initial Green's functions were acquired. The focal spot was produced despite the presence of internal wave-induced sound speed fluctuations, which results in a change in the Green's function between the time it is acquired and retransmitted.

The first Born, or single scattering approximation was used in deriving an expression for a sensitivity kernel that linearly maps changes in sound speed to changes in pressure at the receiver. These kernels are then studied from the point of view of time-reversal and applied to sound transmission in free space and a Pekeris waveguide. These simple examples were useful in providing insight into the stability of the time reversal focal spot. It was found that sensitivity kernels have a Fresnel-like interference pattern consisting of regions of positive and negative sensitivity to sound speed changes. During time-reversal transmissions, several of these kernels, corresponding to different paths, were found to overlap due to the fact that time-reversal delays each path such that they all arrive at the same time. Overlapping kernels, each having different patterns of sensitivity, result in a net reduction of sensitivity compared to the sensitivity of a single path.

As a logical next step, prior knowledge of the kernels that make up the focal spot was utilized to derive optimized source functions that can provide an

environmentally-adaptive focusing ability. These functions are regularized versions of the inverse filter, with a physics-based regularization using sensitivity kernels and the covariance of sound speed fluctuations. The optimized source functions were seen to have a focal spot quality in-between time-reversal and the inverse filter, but a stability greater than both. While time-reversal is still an enormously viable focusing scheme due to its inherent simplicity, the optimized source functions may be useful when environmental data are available such as during shallow-water tomography experiments.

Sensitivity kernels and the optimized source functions were then tested using experimental data gathered during the FAF05 experiment. It was found that the pressure sensitivity to sound speed changes was quadratic in nature, as a result of which the linear first Born approximation is only valid for about 10 minutes of Green's function evolution. Sensitivity kernels were derived for the experimental environment, and used to compute optimized source functions. Sound speed statistics for the environment were calculated using an internal wave model whose characteristics was matched to thermistor chain measurements. Optimized source functions were then compared to time-reversal and the inverse filter and gains found to be in the right sense, although small, due to the limited time-windows available during which the kernels were linear.

The last part of the dissertation demonstrated a method of inverting thermistor chain data for a reference temperature profile. Knowledge of a reference profile is useful in acoustic propagation modeling, or in order to compute a sensitivity kernel to model pressure and travel-time fluctuations. Temperature observations were assumed to be caused by displacements which have a larger time- and depth-scale compared to temperature. A Gauss-Newton method was then utilized to invert for a reference temperature. The method was then demonstrated on several test cases where the estimate was shown to compare well with a known profile. Finally, the method was demonstrated on thermistor chain data available during the FAF05 experiment, where it was shown to also perform well with respect to several diagnostics.

## 5.1   Future Work

There are several aspects of this dissertation that can be explored further, some of which may be summarized as follows.

- The second Born approximation may be applied in deriving pressure sensitivity kernels, which will allow them to track received pressure even as it varies quadratically. This enhanced tracking ability could possibly be used to predict the behavior of the time-reveral focal spot in realistic perturbations scenarios. This can also lead to the optimized source functions being demonstrated on significantly longer time scales compared to the 10 minutes currently demonstrated.

- Equalizers in underwater communications currently track arrival paths in order to minimize intersymbol interference. Sensitivity kernels could prove useful in enhancing equalizer performance by providing information on which paths are more likely to fluctuate given a particular perturbation scenario compared to others.

- The inversion method for a temperature profile currently uses for its first estimate the mean, median or the first of temperature observations. Better first estimates for the temperature profile could lead to improved final estimates.